

ALMA MATER STUDIORUM - UNIVERSITÀ DI BOLOGNA

**Dottorato di Ricerca in Ingegneria Energetica,
Nucleare e del Controllo Ambientale**

Ciclo XXV

Settore concorsuale di afferenza: 09/C3

Settore scientifico-disciplinare: ING-IND/19

**VALIDATION OF THE CFD CODE NEPTUNE FOR A FULL SCALE
SIMULATOR FOR DECAY HEAT REMOVAL SYSTEMS WITH
IN-POOL HEAT EXCHANGERS**

Presentata da: FEDERICA BASSENGHI

Coordinatore di Dottorato:
Prof. ANTONIO BARLETTA

Relatore:
Dott. Ing. SANDRO MANSERVISI

Esame finale anno 2013

Contents

Introduction	3
1 The CATHARE Code	7
1.1 CATHARE object oriented structure and system modeling	8
1.1.1 The assembly modules	8
1.1.2 The main modules	9
1.1.3 The sub-modules	12
1.1.4 Non-condensable gases and radio-chemical components	14
1.2 The two-fluid model	14
1.2.1 The two-phase flow regimes	15
1.2.2 Mass, momentum, and energy equations	15
1.2.3 Closure relations	19
1.2.4 Wall and interfacial transfers	19
1.3 CATHARE solution procedure	20
1.3.1 Introduction	20
1.3.2 Computation scheme	21
1.3.3 Post-processing data specification	23
1.4 CATHARE Input deck	23
1.4.1 The DATA block	23
1.4.2 Executable block	28
2 The Neptune CFD code	31
2.1 Two-fluid model in NEPTUNE code	32
2.1.1 Multi-field balance equations	32
2.1.2 Interface transfer closure laws	36
2.1.3 Bulk interface heat and mass transfer	39
2.1.4 Nucleate boiling model	42
2.1.5 Turbulent modeling	46
2.2 Numerical discretization	48

2.2.1	Momentum equations	48
2.2.2	Mass-Energy equations: the Alpha-Pressure-Energy cycle	53
2.2.3	Volume conservation and pressure projection	58
2.3	The NEPTUNE data, param file and user routines	60
2.3.1	NEPTUNE data structure of the code	60
2.3.2	The NEPTUNE param file	62
2.3.3	User routines	65
2.4	A param file for standard boiling flow in a rectangular channel with constant bubbles diameter	66
3	The PERSEO Facility	75
3.1	The main features of the PERSEO test facility	75
3.1.1	Introduction	75
3.1.2	Test facility geometry	76
3.1.3	Circuit configuration and operation	79
3.2	PERSEO experimental data	80
3.3	Experimental text MATRIX	80
3.3.1	Test n.7	84
3.3.2	Test n.9	93
4	CATHARE Modeling of PERSEO facility	99
4.1	The CATHARE model	99
4.2	Analysis of the PERSEO Tests	100
4.2.1	Test n.7 - Phase 1	100
4.2.2	Test n.7 - Phase 2	104
4.2.3	Test n.9	108
4.3	3D Overall Pool modeling	111
4.3.1	Test n.7 - Phase2	113
4.3.2	Test n.9	115
5	NEPTUNE_CFD modeling of PERSEO facility	119
5.1	Introduction	119
5.2	CATHARE-NEPTUNE coupled simulation	119
5.3	The two-dimensional model	122
5.3.1	Geometry and Boundary conditions for the Test 9	122
5.3.2	Physical properties and models set in the param file	124
5.3.3	Results obtained for the test 9	131
5.3.4	Steam injection on boiling pool	138
5.3.5	Injection above water level	140

INTRODUCTION 3

5.4 The OP-injector three-dimensional model 142

5.4.1 Results obtained for the test 9 142

Conclusions 156

Bibliography 163

Introduction

Simulations of multi-physics and multi-scale systems have a fundamental impact on engineering sciences. The study of multi-physics systems deals with simulations that involve multiple physical models and multiple simultaneous physical phenomena. The multi-scale modeling is aimed to evaluate material properties or system behavior on one scale using information or models from different scales. Various mathematical models may be used for the description of the system on each different scale. Multi-scale modeling is very important in complex systems where a direct simulation is not possible, since the time and length scales of the individual processes involved differ by orders of magnitude. However, numerical simulations of these multi-physics and multi-scale problems, require a strong development of sophisticated models both with efficient numerical algorithms and advanced computational techniques.

In order to study complex thermal hydraulic problems, a multi-scale analysis can be used to take advantage of increased computer power and improved simulation tools, including Direct Numerical Simulation (DNS), Computational Fluid Dynamics (CFD) and system thermal hydraulic codes. Furthermore, this multi-scale analysis is often developed with four scales corresponding to four topologies of simulation software: the system scale, the component scale, the CFD scale (meso-scale) and the DNS scale (micro-scale). The system scale is dedicated to the overall description of the circuits of a nuclear plant. The component scale is made for the design, safety, and operation studies of reactor cores and heat exchangers (steam generators, condensers, auxiliary exchangers). The meso-scale requires a CFD-type software to be solved in an open three-dimensional medium. The average scale (one millimeter or less) goes beyond the limits of the component scale for a finer description of the flows. This scale includes turbulence modeling using the RANS or URANS approach. This is also the only scale able to predict the fluid temperature field to analyze thermal shocks or thermal fatigue of the reactor structures. The micro-scale corresponds to the DNS or pseudo-DNS approaches and may also include some LES-like approaches. This characteristic length may focus on very small domains (e.g. containing a few bubbles or droplets). In order to better investigate a component of the system or when detailed information on a spe-

cific part of the domain is required (as when there is a particular interest in small scale phenomena taking place in a limited part of the domain), a coupling between two or more scales may be used. For example, it is possible to conceive a monodimensional system code which can predict the behavior of the primary circuit in order to supply boundary conditions to a three-dimensional CFD code for the investigation of the thermal hydraulic of a specific component.

In the present work, a multi-physics simulation concerning an innovative safety system for light water nuclear reactor is studied with the aim to increase the reliability of its main decay heat removal system. In particular, the system studied is able to remove the decay power from the primary side of the light water nuclear reactor through a heat suppression pool. In previous works, two examples of energy removal systems utilizing in-pool heat exchangers have been proposed to be installed in the GE-SBWR and in the Westinghouse AP-600: the isolation condenser and the passive residual heat removal system, respectively. In both systems, the heat transfer was actuated by opening of a valve installed on the primary side of the reactor. The first proposal of moving the primary side valve to the pool side was analyzed by CEA and ENEA in the thermal valve concept project. In this case, the valve was located, steam side, at the top of a bell, covering the pool immersed heat exchanger. During normal operation, the valve is closed to prevent the heat transfer due to the formation of steam under the bell, while in emergency conditions the valve opening caused the discharge of the insulating steam and the beginning of heat transfer from the primary side to the pool. The PERSEO (in-Pool Energy Removal System for Emergency Operation) project is an evolution of the Thermal Valve concept project where the triggering valve is installed liquid side, on a line connecting two pools at the bottom. The valve is closed during normal operation. In emergency conditions the valve is opened, the heat exchanger is flooded with consequent heat transfer from the primary side to the pool side. In this work, two main experimental PERSEO tests are studied computationally by coupling the monodimensional system code CATHARE, which reproduces the system scale behaviour, with a three-dimensional CFD code NEPTUNE_CFD, allowing a full investigation of the pools and the injector and for code validation purposes. The coupling between the two codes is realized through the boundary conditions.

Chapter 1

The CATHARE Code

The Code for Analysis of Thermal-Hydraulics during an Accident of Reactor and Safety Evaluation (CATHARE) is a system code developed to perform best-estimate calculations of a pressurized water reactor (PWR). This code is the result of a joint effort of the main French reactor commercial industry for nuclear power AREVA-NP, the French Atomic Energy Commission (CEA), the French electric utility (EDF) and the French Nuclear Safety Institute (IRSN). The CATHARE team, in charge of the development, the assessment and the maintenance of the code is located at CEA in GRENOBLE. The main objectives of the code are to perform safety analysis and analyze plant behavior providing real time calculation. The code is nowadays mainly used to perform safety analysis with best estimate calculations of thermalhydraulic transients of PWR for designed accidents such as LBLOCAs and to quantify the conservative analysis in SBLOCAS, SGTR, Loss of RHR, Secondary breaks and Loss of Feed-water accidents. The CATHARE code is also used to define plant operating procedures and for research and development. In this case the code is integrated with training simulators providing real time calculation. In fact a simplified version of CATHARE is implemented in the SIPA simulator presently used at EDF. Also the standard CATHARE version is implemented in the next generation simulator family under the SCAR project. On the recent version of the CATHARE code specific modules have been implemented to allow modeling of other reactors like boiling water reactor or gas cooled reactors.

The CATHARE code includes several independent modules that take into account any two-phase flow behavior, such as mechanical non-equilibrium (vertical co- or counter-current flow, flooding counter-current flow limitation and horizontal stratified flow, critical or not critical flow co- or counter-current flow), thermal non-equilibrium (critical flow, cold water injection, super-heated steam, reflooding) and all flow regimes and all heat transfer regimes. In order to take into account these phenomena the CATHARE code is based on a two-fluid and six-equation model including non-condensable gas

equations and additional equations for transporting radio-chemical components. The most recent version of the code V2.5₂ CATHARE is provided with new modules suitable for gas reactors (HTR High Temperature Reactor, Gas Turbine Modular Helium Reactor "GT MHR"), for the simulation of gas turbines or compressors, for the representation of the containment building and its interaction with the primary circuit, etc.. [1].

1.1 CATHARE object oriented structure and system modeling

In the CATHARE code each element of the reactor hydraulic circuits must be defined. Each element is described by a CATHARE module (or CATHARE object type) [2]. Depending on their function, nature and similarity, these modules may be: assembly modules, main (or basic) modules, sub-modules, and non-condensable gases together with radio-chemical components. For each module, if not already predefined by CATHARE, users must provide a topological definition, a nodalization definition, a geometrical definition (object size, for example), and a hydraulic definition (kind of flow, singular pressure drops).

The term object-oriented structure is used because modules are hierarchically organized: assembly modules contain modules that contain gadgets and/or sub-modules. Sub-modules are distinguished from gadgets because they may interfere with several modules, whereas gadgets only modify the behavior of a single module locally. The word "contain" should be understood literally in the physical sense but also with respect to the structure of CATHARE software; modules inherit properties from assembly modules; similarly gadgets or sub-modules inherit properties from their "parent" modules. Non-condensable gases, for example, can consequently be defined as belonging to an assembly module and are not need to be defined for each element making up the hydraulic circuit. Now the different modules are briefly described.

1.1.1 The assembly modules

The assembly modules are used to group basic modules. There are three assembly elements: REACTOR, CIRCUIT and ZONE.

The REACTOR element consists of CIRCUIT elements. Circuits connected in this way may be physically connected by heat exchangers. Several reactor elements can be defined in the same input deck, but from the calculation point of view is separated from one another. This module is used to control thermal hydraulic computation. It may also be used to launch specific calculations or initializations.

The *CIRCUIT element* consists of all the basic elements making up the hydraulic circuit. Some parts of the circuit can be isolated from the circulating fluid zone with valves. But as the fluid is the same in the entire circuit, non-condensable gases and radiochemical components are defined for a circuit element (obviously the concentration or radioactivity of fluid components are not necessarily the same in the entire circuit).

The *ZONE element* is designed to help CATHARE users process calculation results. It enables several elements of the same circuit to be combined in an assembly on which CATHARE performs mass and energy-balance calculations.

1.1.2 The main modules

Several main modules can be assembled to represent the primary and secondary circuits of any reactor and of any separate-effect test or integral effect test facility. The main modules are the following: the AXIAL element 1D module, the VOLUME element 0D module, the 3D module, the BOUNDARY CONDITION module and the RUPTURE module. Modules are connected by JUNCTIONS as shown in Figure 1.1.

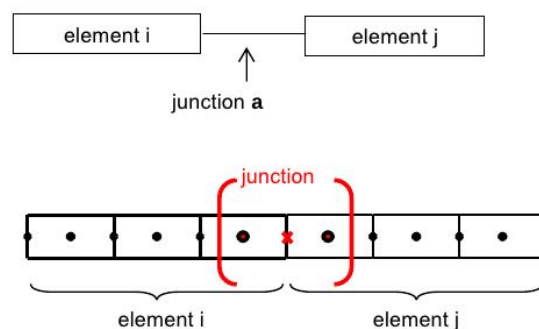


Figure 1.1: Junction between two modules

A *JUNCTION* is represented by a physical vector point and by two scalar points, which are all shared by the two connected elements. The vector point specifications (geometrical parameters, flow area, gravity, etc.) are provided adopting the point of view of each adjacent element; both sets of specifications must be consistent with each other and should satisfy CATHARE reader controls.

The *AXIAL element 1D module* is used to describe parts of the plant in which the refrigerant flow is predominantly one-dimensional such as hot and cold legs, SG U-tubes, expansion line, core channels, core bypass, downcomer SG rise, SG vapor line. It may

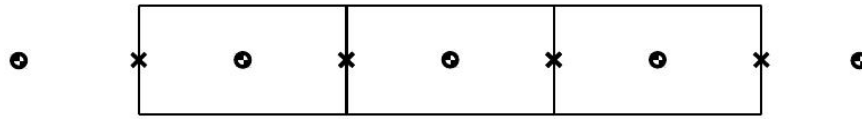


Figure 1.2: AXIAL 1D element

be connected to all the other modules and to all the sub-modules. An example of Axial element is shown in Figure 1.2.

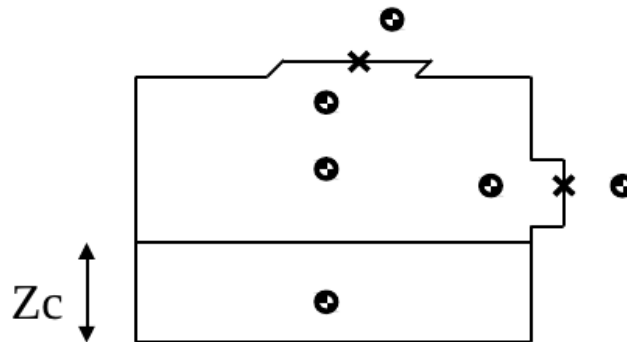


Figure 1.3: VOLUME 0D element

The *VOLUME 0D module* is a two-node module used to describe large size plena with several connections, such as the pressurizer, the accumulator, the steam generator dome, the upper and lower plenum and the dome of the vessel of a PWR. The volume predicts swell level, total or partial fluid stratification and phase separation phenomena at the junctions. Main assumptions are considered for 0D module: all thermal-hydraulic quantities are assumed uniform in horizontal planes and inertial forces are assumed to be negligible compared to gravity forces. Consequently, the momentum equations are simplified and the pressure field is hydrostatic. The stratification is represented by a two-node model with two sub-volumes. The interface between the sub-volumes has a variable level. In each sub-volume, enthalpies and void fractions are assumed to be uniform but not the pressure which has a hydrostatic gradient. It is assumed that there is liquid in the lower sub-volume possibly with gas rising towards the interface. In the upper sub-volume there is mainly gas, possibly with liquid drops or falling jets. Scalar variables are calculated inside the volume in front of each junction. Flow distribution between sub-volumes and the phase sorting phenomena are mod-

eled at each junction, taking into account the two-phase jet effect pull-through process. Mass and energy transfer between the two sub-volumes (bubble rise, fall of droplets, condensation, evaporation) are modeled. For the one-phase liquid case, the upper sub-volume is residual (height = 1 cm). Respectively the lower sub-volume is residual for one-phase gas fluid (height = 1 mm). In Figure 1.3 it is shown a 0D volume structure where Z_C is the variable separation level.

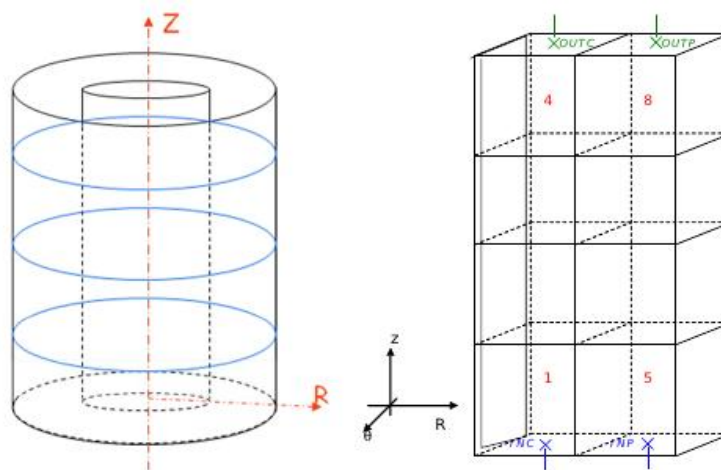


Figure 1.4: 3D module

The 3D module is created to represent large-scale thermal-hydraulic 3D effects in nuclear power plants. One of the main applications is the modeling of a PWR vessel. Figure 1.4 shows an example of 3D module. The 3D module has been only validated for PWR vessel modeling. The use of the 3D module can be extended to other geometries but the validation of such geometries has to be performed by users. The main phenomena to be addressed are the three main phases of a large break LOCA, i.e., blow-down, downcomer refill and core reflooding phases, for which turbulent phenomena are not dominant. Therefore the turbulent model is dedicated to very specific applications where the model is applied to a single phase.

The *BOUNDARY CONDITION* module is an element which can be placed at the extremity of a pipe, a volume, a tee or a 3D module. Figure 1.5 shows an example of boundary condition module. It is used to impose one or more hydraulic conditions for each phase (pressure, enthalpies or temperatures, velocities or mass flow rates for gas or liquid, the void fraction or the mass fraction of non-condensable gases or radiochemical components). These boundary conditions can be defined at the inlet or the

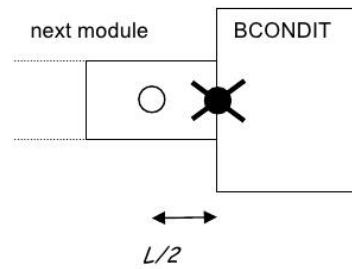


Figure 1.5: Boundary condition module

outlet of an element. The choice of the type and number of boundary conditions to impose takes account of the characteristic velocities. For example when liquid enters liquid enthalpy and void fraction are imposed, when gas enters gas enthalpy and non-condensable gas qualities are imposed.

The RUPTURE module The RUPTURE element is used to model a double-ended pipe break, with scope for critical flow rate conditions. An example of RUPTURE elements is shown in Figure 1.6. This object can only be connected to two AXIAL elements because critical flow can only be calculated on meshed elements. The RUPTURE element may be seen as the combination of two outlet boundary conditions, each one attached to an AXIAL element.

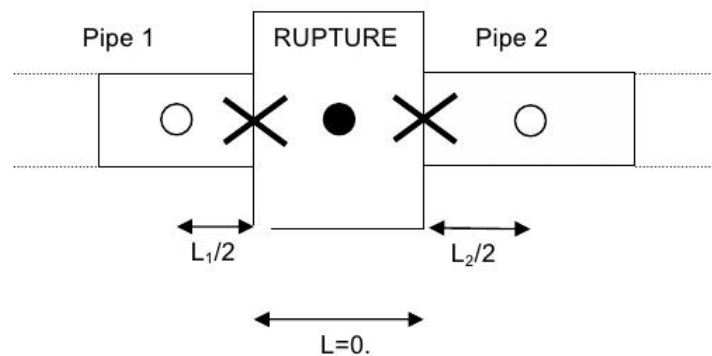


Figure 1.6: RUPTURE element

1.1.3 The sub-modules

A sub-module is a group of subroutines connected locally to a module, that calculates additive terms for the equations of the module. A sub-module may have internal vari-

ables and internal equations to calculate the additive terms.

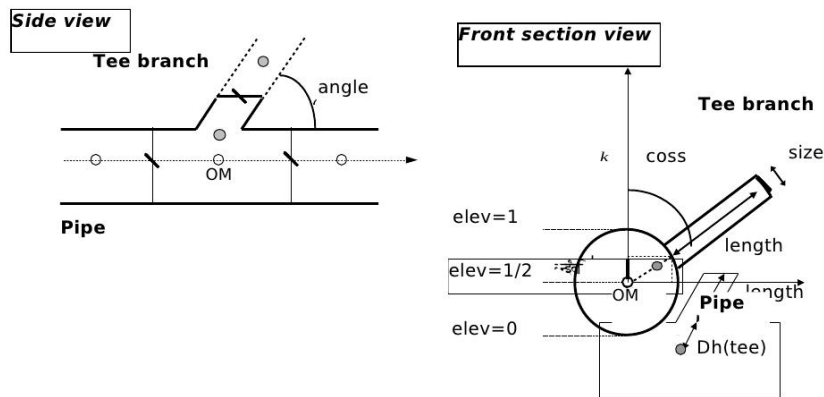


Figure 1.7: TEE scheme

Two kinds of sub-modules exist and are listed below.

Extended sub-modules (having a wide interaction with the module): the *multi-layer WALL* sub-module in which radial conduction is calculated, the *heat exchangers* sub-module that can be used between two circuits or between two elements of a circuit, the *fuel pin thermo-mechanics* sub-module which can predict fuel cladding deformation, creep, rupture, clad oxidation and thermal exchanges, the *reflooding* sub-module with a 2-D heat conduction model in the wall or in fuel rod for predicting the quench front progression. Two kind of reflooding sub-modules can be used, the bottom-up reflooding. Finally the *top-down reflooding and the point neutronics* sub-module (a 3-D neutronics code can also be coupled to CATHARE).

Sub-modules (or gadgets) connected to one mesh: the *TEE* sub-module used to represent a lateral branch (tee-branch) on a 1D module. This sub-module predicts phase separation phenomena and a specific modeling effort has been paid for cases where the flow is stratified in the main pipe. Figure 1.7 shown an example of TEE scheme. The *accumulator* sub-module, *sources (fill) and sink (loss) injection mass* sub-modules (including break and Steam Generator Tube Rupture), the *1-node pump* sub-module, the *PRZ pressurizer* sub-module based on the 0D module with specific features, *valves, safety valves, check valves, flow limiters* sub-modules, the *CCFL* sub-module which may be connected at any junctions, or at any vector node of the 1-D or 3-D modules in order to predict counter current flow limitation in complex geometries such as the upper core plate and the inlet of Steam Generator tubes.

1.1.4 Non-condensable gases and radio-chemical components

More than the main fluid used for PWR or BWR reactors, (steam and liquid water), CATHARE can define other main fluids or other elements in the circuit fluid. Figure

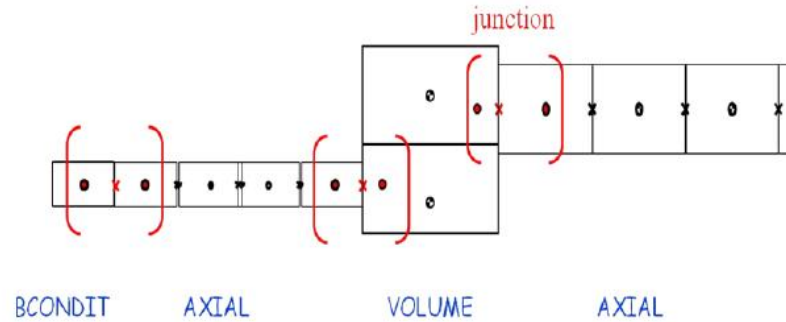


Figure 1.8: Assembly of modules

1.8 shows an assembly of modules. These elements are described through the following three components: non-condensable gases, radio-chemical elements and other fluids.

Transport of one to four *non-condensable gases* by a circuit can be modeled by CATHARE. These gases are assumed to be in thermal and mechanical equilibrium with steam. Non-condensable gas concentration has an impact on the standard calculation because it changes the vapor pressure, which becomes a partial pressure with respect to the gas phase total pressure and the condensation correlations (condensation is reduced in the presence of non- condensable gases).

The *radioactive/radio-chemical element* module is used to follow boron concentration and /or fission components in the primary circuit. CATHARE includes a mass-continuity equation for a solute moving with the liquid field, for a gas moving with the gas phase and also allows dissolution and evaporation of the component. In case of radioactive products, the decay period is taken into account to calculate the activity.

1.2 The two-fluid model

The CATHARE code describes properly the different of phase regimes, the interface behavior and the transport of the state variable by using well defined physical models. All modules use the two-fluid model to describe steam-water flows and four non condensable gases. Both thermal and mechanical non-equilibrium of the two phases may

be taken into account [3].

1.2.1 The two-phase flow regimes

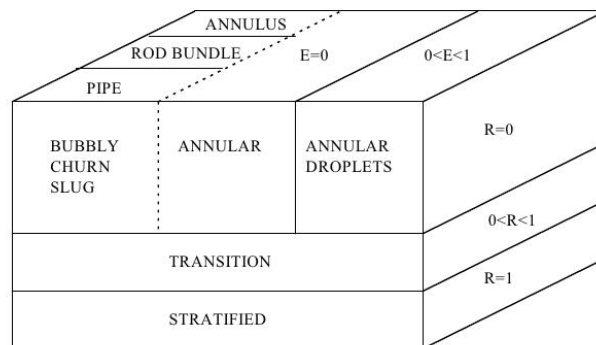


Figure 1.9: Map of the motion regimes in CATHARE code

The two-phase flow patterns are modeled in the CATHARE code but only two transitions are explicitly written and used in several closure terms of CATHARE: the transition between stratified and no stratified flow. This transition depends on two criteria: a first criterion is based on Kelvin-Helmholtz instability threshold and the second depends on the relative effects of bubble sedimentation and of bubble turbulent mixing. The second transition is between annular and droplets flows. These two transitions describe the change from a separate flow to a dispersed flow. Co-current and counter-current flows are modeled with prediction of the Counter-Current Flow Limitation (CCFL). The Figure 1.9 shows a map of motion regimes treated by CATHARE. Heat transfer with wall structures and with fuel rods are calculated taking into account all heat transfer processes. In Figure 1.9 one can see the appropriate zone for natural/forced convection with liquid in both laminar and turbulent regimes, natural/forced convection with gas in both laminar and turbulent regimes, subcooled/ saturated nucleate boiling with criteria for onset of nucleate boiling, critical heat flux, dry-out criterion, rewetting temperature and transition boiling, film boiling for inverted annular, inverted-slug and dispersed flows, film condensation for effects of non-condensable gases, and finally radiation to vapor and to liquid.

1.2.2 Mass, momentum, and energy equations

Mass, momentum, and energy equations are established for any CATHARE module. They are written for each phase and derived from exact local instantaneous equations,

using some simplification through physical assumptions and using time and space averaging procedures. In this section the model for axial 1D module is presented. to the 3D and 0D modules. One up to four transport equations can be added when non condensable gases are present.

Mass balance equations

Liquid phase

$$\frac{\partial}{\partial t}(A(1-\alpha)\rho_L) + \frac{\partial}{\partial z}(A(1-\alpha)\rho_L v_L) = -A\Gamma + S_L, \quad (1.1)$$

Gas phase

$$\frac{\partial}{\partial t}(A\alpha\rho_G) + \frac{\partial}{\partial z}(A\alpha\rho_G v_G) = A\Gamma + S_G + \sum_{(i=1)}^4 S_i. \quad (1.2)$$

Non condensable transport equation

$$\frac{\partial}{\partial t}A\alpha\rho_G X_i + \frac{\partial}{\partial z}A\alpha\rho_G X_i v_G = S_i, \quad (1.3)$$

with

$$\Gamma = \frac{q_{pi}\chi_c/A - q_{Le} - q_{Ge}}{H_V - H_L} + \Gamma_r. \quad (1.4)$$

Γ is the interfacial mass transfer [kg/m^3s] and Γ_r is the residual value use to have $\alpha_{min} \leq \alpha \leq \alpha_{max}$

$$\Gamma_r = \begin{cases} -\rho_G \frac{\alpha - \alpha_{min}}{\theta_V} & \text{when } \alpha < \alpha_{min} \text{ Vaporization} \\ 0 & \alpha_{min} < \alpha < \alpha_{max} \\ -\rho_L \frac{\alpha - \alpha_{max}}{\theta_L} & \text{when } \alpha_{max} < \alpha \text{ Condensation} \end{cases} \quad (1.5)$$

Momentum equations

Liquid phase

$$\begin{aligned} (A(1-\alpha)\rho_L) \left[\frac{\partial v_L}{\partial t} + v_L \frac{\partial v_L}{\partial z} \right] + A(1-\alpha) \frac{\partial P}{\partial z} + A p_i \frac{\partial(1-\alpha)}{\partial z} - \\ A\beta\alpha(1-\alpha)\rho_m \left[\frac{\partial v_G}{\partial t} - \frac{\partial v_L}{\partial t} + v_G \frac{\partial v_G}{\partial z} - v_L \frac{\partial v_L}{\partial z} \right] = \\ -A\Gamma(w_i - v_L) + A\tau_i - \chi_f C_L \frac{\rho_L}{2} v_L |v_L| + A(1-\alpha)\rho_L g_z + R \frac{\alpha}{4} p_i \frac{\partial A}{\partial z} + S M_L, \quad (1.6) \end{aligned}$$

Gas phase

$$(A\alpha\rho_G)\left[\frac{\partial v_G}{\partial t} + v_G\frac{\partial v_G}{\partial z}\right] + A\alpha\frac{\partial P}{\partial z} + Ap_i\frac{\partial \alpha}{\partial z} + A\beta\alpha(1-\alpha)\rho_m\left[\frac{\partial v_G}{\partial t} - \frac{\partial v_L}{\partial t} + v_G\frac{\partial v_G}{\partial z} - v_L\frac{\partial v_L}{\partial z}\right] = A\Gamma(w_i - v_G) - A\tau_i - \chi_f C_G \frac{\rho_G}{2} v_G |v_G| + A\alpha\rho_G g_z + R\frac{(1-\alpha)}{4} p_i \frac{\partial A}{\partial z} + SM_G, \quad (1.7)$$

with

$$\rho_m = \alpha\rho_G + (1-\alpha)\rho_L. \quad (1.8)$$

Energy equations

Liquid phase

$$A\frac{\partial}{\partial t}\left((1-\alpha)\rho_L\left[H_L + \frac{v_L^2}{2}\right]\right) + \frac{\partial}{\partial z}\left(A(1-\alpha)\rho_L v_L\left[H_L + \frac{v_L^2}{2}\right]\right) - A(1-\alpha)\frac{\partial P}{\partial t} = Aq_{Le} + \chi_e q_{pL} - A\Gamma\left[H_L + \frac{w_i^2}{2}\right] + A(1-\alpha)\rho_L v_L g_z + SE_L. \quad (1.9)$$

Gas phase

$$A\frac{\partial}{\partial t}\left(\alpha\rho_G\left[H_G + \frac{v_G^2}{2}\right]\right) + \frac{\partial}{\partial z}\left(A\alpha\rho_G v_G\left[H_G + \frac{v_G^2}{2}\right]\right) - A\alpha\frac{\partial P}{\partial t} = Aq_{Ge} + \chi_e q_{pG} + A\Gamma\left[H_G + \frac{w_i^2}{2}\right] + A\alpha\rho_G v_G g_z + SE_G. \quad (1.10)$$

State equations for the gas mixture

Four non condensable gases can be calculated

$$\begin{aligned} \rho_i &= X_i \rho_G & P_i &= \rho_i R_i T_G, \\ \rho_G &= \sum_{i=1}^4 \rho_i + \rho_V(T_G, H_V) & \text{for } i &= 1, 4, \\ P &= \sum_{i=1}^4 P_i + P_V, \\ H_G &= \left(1 - \sum_{i=1}^4 X_i\right) H_V + \sum_{i=1}^4 [X_i (h_{vs7} + cp(T_G - T_{s7}))], \end{aligned} \quad (1.11)$$

with $H_V = H_V(P_V, T_G)$, $h_{vs7} = H_{Vsat}(7bar) \approx 2766430 J/kg$ and $T_{s7} = T_{sat}(7bar) \approx 164.93^\circ C$.

The value of transport properties used during calculation depends on the mixture model chosen by user. By default the following standard models are used for the gas mixture viscosity and conductivity computation:

$$\mu_G = \sum_i y_i \mu_i, \quad \lambda_G = \sum_i y_i \lambda_i, \quad (1.12)$$

where y_i and μ_i (respectively λ_i) stands for the molar fraction and for the pure gas viscosity (respectively pure gas conductivity) of each species.

S_L, S_G, S_i are the source terms of mass for liquid, steam and non condensable gases [kg/ms], X_i is the specific fraction of the non condensable gas i , β is the added mass coefficient, w_i is the interface velocity [m/s], χ_f is the friction perimeter [m], C_L and C_G are the wall friction coefficient for the liquid and the gas and R is the rate of stratification, SM_G and SM_L are the source terms of momentum for gas and liquid, q_{Le} and q_{Ge} are the interface to liquid and to gas heat fluxes [W/m^3], χ_e is the heating perimeter [m], q_{pL} and q_{pG} are the the wall to liquid and to gas heat fluxes [W/m^2].

The main variables are six: pressure, liquid enthalpy, gas enthalpy, void fraction, liquid velocity and gas velocity ($P, H_L, H_G, \alpha, v_L, v_G$) and, if it exists, $X_i (i = 1, 4)$ non-condensable mass fraction (with related transport equations). The model of the 1D module is extended to the 3D and 0D modules. In the 3D module $10(+X_i)$ main variables are considered, with the momentum equations being written in all three directions: $P, H_L, H_G, \alpha, v_{Lx}, v_{Gx}, v_{Ly}, v_{Gy}, v_{Lz}, v_{Gz}$. The 0D modules is divided in two sub volumes. The main variables are pressure, liquid enthalpy, gas enthalpy, void fraction and non-condensable mass fraction (with related transport equations) for each sub volume and the separation level elevation between the two sub-volumes. Two energy and mass balance equations are written for each sub volume. For the volume, a total pressure equation is written. The system always has six equations: even in single-phase computations, a residual phase treatment is used.

To simplify the balance equation, some terms, such as the axial component of the viscous stress tensor and its work, the axial heat conduction, the axial mass diffusion (in case of non condensable gas transport), the work of the interface forces and the pressure distribution forces in the energy equation, are negligible. Moreover, in the averaging process, all correlation coefficients are assumed equal to one and the phase kinetic energy is assumed to be due to the axial motion. Finally, the water and gas properties (which are valid for local instantaneous variables) are assumed also valid for averaged variables and they are calculated with the mean pressure P and not the phase pressure.

Simplify assumptions are applied also on the interface balance equations. In partic-

ular, it has been assumed that the interface has no thickness and no mass, the superficial tension in the momentum balance is neglected, the contribution of superficial tension in the energy balance is neglected and both phases have the same velocity at the interface supposed uniform.

1.2.3 Closure relations

The solution of the system of differential equations implemented in the CATHARE code requires closure equations that take into account the physical model and heat, mass and momentum transfer phenomena between a phase and the other and between the fluid and the walls. These closure equations are developed according to some considerations. First, as far as possible, physical closure laws are developed on an experimental basis. A set of a separate effect experiments were performed and analyzed. Original correlations are developed when existing models are not satisfactory. The degree of empiricism depends on the comprehension of the physical mechanisms involved. In the domain where experimental and theoretical knowledge are missing, it needs to extrapolate the data by making simple assumptions, depending of the case studied. Also, it needs to consider that thermal and mechanical transfers are interconnected. So, it is assumed in a first approximation that mechanical interactions do not strongly depend on thermal exchanges. Mechanical terms are first derived from experiments where thermal non equilibrium is negligible. Interfacial heat transfer terms are then derived. Then, wall to fluid heat fluxes are correlated. Finally, it should be known that each closure law is unique. No choice between several correlations is proposed to the users in order to reduce the user effect. Also, it should be emphasized that the user does not have the possibility of choosing between the various correlations used by the code, in order to minimize the influence of the choices of the user on the results provided from the code.

1.2.4 Wall and interfacial transfers

These terms are calculated by the code through the application of many correlations. The main ones are mention below.

The interfacial friction correlations for bubbly-slug-churn flows. This correlations were developed from an extensive database and validated for tube annular and rod bundles geometries [4].

The wall friction. It is mainly derived from a modified Lockhardt-Martinelli correlation. An empirical phase distribution, consistent with limit cases and with the CATHARE experimental basis has been developed [5]

The wall heat transfer for dry wall situation. A semi-empirical approach has been followed starting from bibliography correlations for inverted annular and droplet flow regimes. Models parameters have been adjusted to fit reflooding data [6],[7],[8].

The flashing. The correlation is mainly empirical and derived from the analysis of critical flow tests [9].

The direct contact condensation at safety injection. A semi-empirical correlation accounting the local effects of the injection jet has been developed [10].

The non condensable gas effect. The modeling of mass diffusion effects is based on a classical heat and mass transfer analogy. An original procedure was developed in order to avoid the calculation of the interface temperature [11], [12].

1.3 CATHARE solution procedure

1.3.1 Introduction

A CATHARE computation consists of three stages, corresponding to three separate executables: pre-processing, computation and post-processing. Each of them requires and generates some files containing data.

CATHARE pre-processing (READER.exe) involves a user input deck. These data contain a description of the hydraulic circuit(s) to be simulated, the events occurring during the simulation and how calculation is managed. The input file is the Input deck. The output files are V25.INIT (file containing the image of the input deck data block) and FORTRAN file PILOT.f (translation of input deck execution block).

CATHARE calculation (CATHAR.exe) is the stage where one execute the simulation described in the input deck, i.e. basically the thermal hydraulic computation. The input files are DICO (Dictionary of key words used by CATHARE), FAST.H and FASTSIZE.f (CATHARE memory dimensioning files). The Output files are the Listing file and the FORT21 (Result file).

In the CATHARE post-processing stage (POSTPRO.exe) users may process CATHARE binary output files to output useful information to a formatted file for analysis. The input files are FORT21 (result file containing saved values), the file containing the cho-

sen definitions of variables for post-processing and files containing the variables corresponding to experimental values to be compared to calculated values - may be used for post-processing. The output file is FORT07 (formatted file with the chosen variables).

1.3.2 Computation scheme

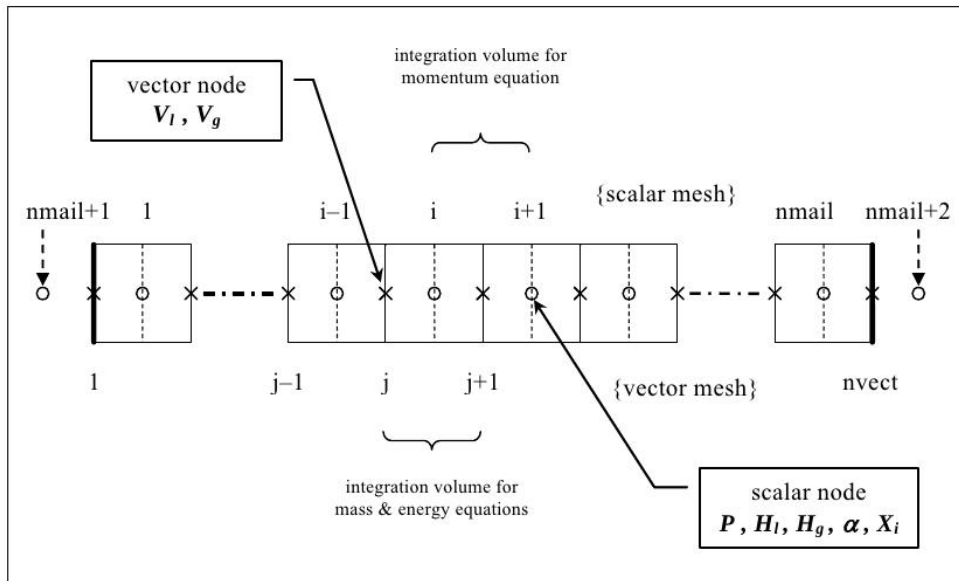


Figure 1.10: Spatial discretization of the AXIAL module

The numerical method in the CATHARE code uses for the spatial discretization a first order finite volume (mass, energy equations) and finite difference (momentum equation) scheme with structured and staggered nodalization. Figure 1.10, 1.11 and 1.12 show the spatial discretization of scalar and vector variables for 1D AXIAL module, 0D VOLUME module and 3D module respectively. The scalar properties of the fluid such as pressure, enthalpy and density, are represented by average conditions of the fluid and are valued in the center of a mesh (scalar point). Vector properties of the fluid, such as speed, are valued in internal points (points between two meshes of an axial element, points located in the middle of each mesh cell face for a 3D element) or at the junctions between two elements.

The time discretization varies from the fully implicit discretization used in the OD and 1D modules to the semi-implicit scheme used in the 3D module. These methods are known for their robustness in a wide range of flow configurations. An hyperbolic system of equations is used to ensure the well posedness of the problem. Mass and energy equations use a conservative form and are discretized in order to keep a very

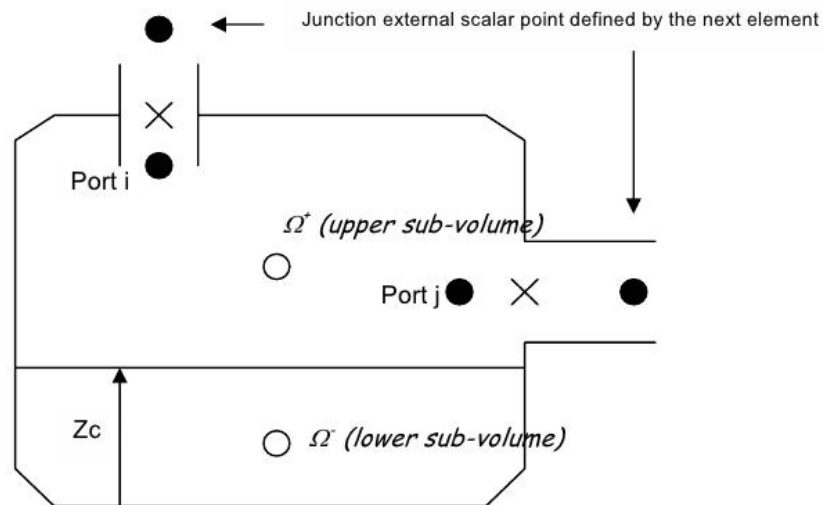


Figure 1.11: Spatial discretization of the standard VOLUME module

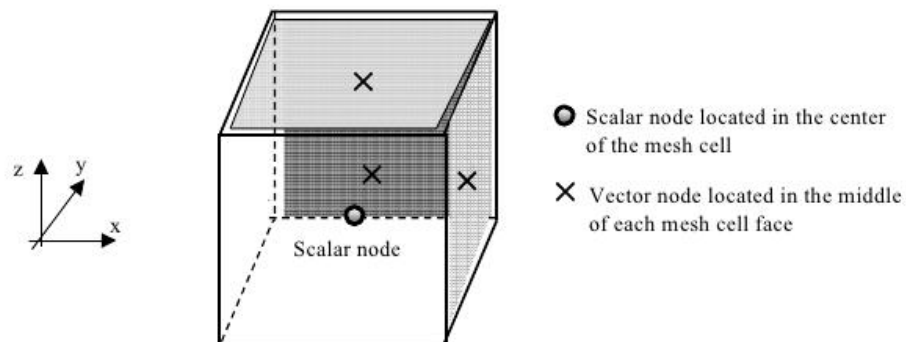


Figure 1.12: Spatial discretization of the 3D module

good mass and energy conservation. The phase appearing and disappearing problem is properly solved using some residual volume fractions and an appropriate conditioning of interfacial mass and energy transfers. The wall conduction is implicitly coupled to hydraulic calculations.

The non linear system of equations is solved by a Newton-Raphson iterative method following several steps. At each iteration:

- increments of internal variables of each element are eliminated as function of increments of junction variables,
- increments of all junction variables are calculated,

- all variable increments are regenerated and convergence tests are performed.

In the last versions of CATHARE (since *V2.5 – 1* and *V2.5 – 2* versions), the solution can be distributed over several processors in order to reduce the CPU time by parallel computing (OPEN MP). This will allow real time calculation of reactor transients for the simulator application (speed-up of 5 on 8 processors for most of the reactor plant safety studies).

1.3.3 Post-processing data specification

In CATHARE code, a post-processing tool is available, also called `postpro` executable. This program processes the result binary file `FORT21` following user `postpro` input deck directives and creates a formatted file `FORT07` suitable for simple graphic representations (XY plots). The default format of this file is not a column format and thus cannot be easily visualized. But an option (`XMGROP`) can be used in the user `postpro` input deck to generate two column formatted files which can be read by most standard software packages.

1.4 CATHARE Input deck

The CATHARE input deck is composed by two parts: the data block part, which deals with the spatial reactor description, and the command block (or `exec` block) part, which deals with the simulated scenario (steady state and time transient). To be understood by CATHARE pre-processing, data acquisition has to use a specific language, which is described in the User manual of CATHARE code [1] and the syntax of each commands is developed in the dictionary [13].

1.4.1 The DATA block

The data block has a modular structure and consists of the description of the reactor, in particular the definition of all module specifications: topological (connections between modules), geometrical (length, high, diameter, angle, etc.), numerical (mesh), hydraulic (type of flow, hydraulic diameter, flow section, etc.), the definition of all sub-modules and gadgets connected to these main modules, the choice of chemical elements and non-condensable gas, the assembling of circuit(s) and reactor.

In the Input deck there are two kinds of instruction:

OPERATOR instruction → is a declaration of a variable or an object and it is characterized by = symbol.

Example:

```
var1 = 12.5;
elem1= AXIAL ent USTREAM exit DSTREAM
```

DIRECTIVE instruction → acts upon calculation or objects properties.

In the data block key words for each element are utilized to define all module specifications. For example, to characterized an AXIAL element the following key words are needed:

AXIAL (topological definition),

GEOM (geometrical definition),

HYDR (hydraulic definition),

MESH (mesh definition),

SINGULAR (optional) (singular pressure-drop definition).

To describe the reactor geometry, two concepts are then used. The first is the **Junction** notion and concerns the object element connection. The second concept concerns the **Weight** notion. This is used to simplify the data file avoiding to repeat identical parts of the reactor.

Junction notion

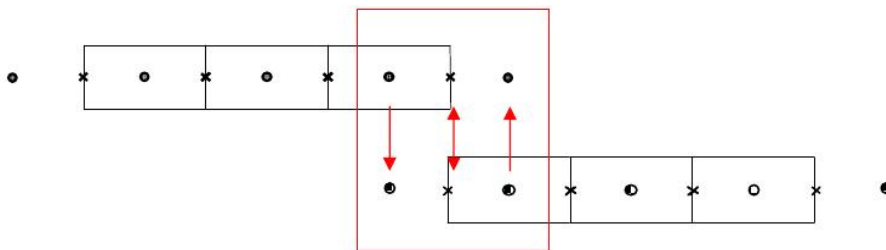


Figure 1.13: junction between two AXIAL elements

A junction is a topological notion used to link two elements (Refer to Section 1.3.2 for an introduction to the notion of junction). A junction is either upstream or down-

stream of the element. This choice is of no importance in terms of flow and is a topological control for the element and the circuit. In an element (except boundary condition) at least one upstream and one downstream junction should be defined. In a circuit, each junction should appear in two, and only two, different element definitions, each with a different direction key word. For each element, a junction consists of an assembly vector node and a scalar node which is a copy of the adjacent module node. Figure 1.13 shows a junction between two AXIAL elements

Weight notion

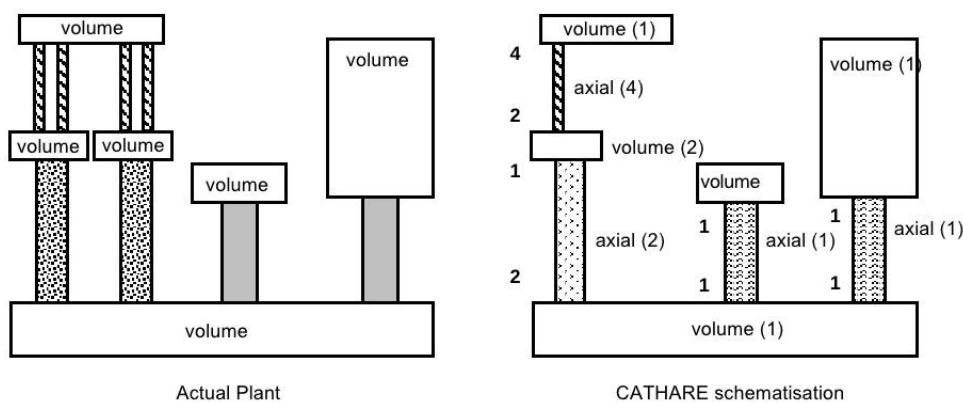


Figure 1.14: weight notion in a hydraulic circuit description

Weight for hydraulic elements. In CATHARE, the notion of weight appears twice, in connections between elements and in a volume or a 3D element concerning junctions. The weight of an element is the number of identical elements simulated by this element. For example, for a reactor with three loops, the broken loop is simulated by elements with weight 1, and the intact loops can be described with a single loop and weight 2 in each element. Inside a capacity or a VOLUME or 3D element, the weight notion for each junction is used to connect several identical elements (or assembly of elements) to the module. The introduction of weights is a way of simplifying the model, but has a drawback: the user loses the possibility of representing asymmetric effects. Moreover the weight has to be taken into account to ensure flow section, gravity and friction perimeter continuity at junctions.

In *VOLUME elements* the junction data SECT and PERI are those of an elementary junction linked to an elementary axial element. The Figure 1.14 illustrates how to use the weight notion to simplify a hydraulic circuit description. In particular SECT is the section of one elementary axial element and PERI is the wall friction perimeter of one

axial element. The SIZE data should be equal to the total size (because it is used to determine flow distribution in sub-volumes). The weight value n is then attributed to the junction connected with n elementary elements modeled by an axial element with weight n .

In the *AXIAL element* all geometrical data are those of an elementary axial element. With reference with Figure 1.14, SECT is section of one elementary element PERI is wall friction perimeter of one elementary element. SIZE represents the size of one elementary element.

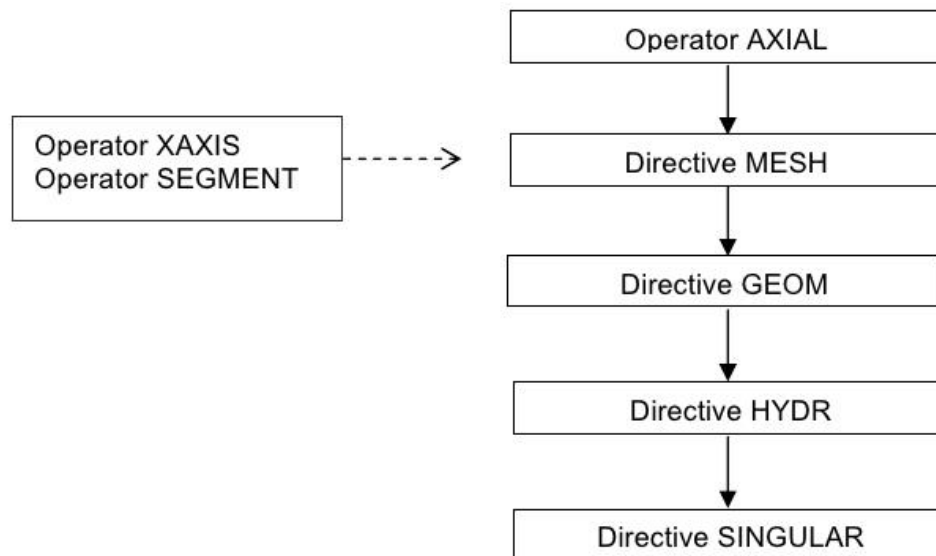


Figure 1.15: Description of an AXIAL element

Weight for sub-modules and gadgets. The WEIGHT is a property that is inherited between a module and its connected sub-modules or gadgets. Example: an AXIAL element is defined with a weight 3. A sink gadget is connected to the third scalar mesh of this axial element. Each of the 3 pipes has a sink connected to its third scalar mesh. If this sink is activated, it will be activated for the three pipes. Consequently, there is no way of imposing a different extracted flow rate for one of these three sinks (because in fact for CATHARE there is only one AXIAL element and one SINK gadget). This is the same for all gadgets and sub-modules. The TEE is the only gadget or sub-module on which a particular weight may be defined (with respect to the main AXIAL module). This is due to the special correlations used for flow rate distribution and stratification making it possible to define several tee branches connected to the same scalar mesh. For example an AXIAL element can be defined with a weight 3. A tee-branch gadget with a weight 2 is connected to the third scalar mesh of this axial element. Each of the

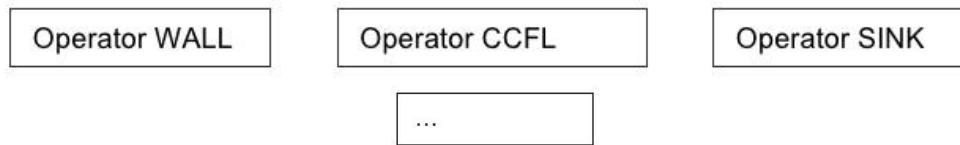


Figure 1.16: Examples of sub-modules or gadget associated with an AXIAL element

three pipes has two tee-branches connected on its third scalar mesh.

Building the geometry to study

For each circuit in the study system the following steps are recommended:

Step 1: Each element, one after the other, has to be completely defined, as well as the belonging-to sub-modules (thermal sub-modules, PWR sub-modules or gadgets). The steps for an AXIAL module and the sub-modules and/or gadgets associated with this element are summarized in Figures 1.15 and 1.16

Step 2: Definition of the components other than water in the circuit with NONCOND or RADCHEMI operator. NONCOND is the key word to define the list of non-condensable gases to use in the calculation (see the Section 1.3.4 for more details of non-condensable gases) and RADCHEMI is the key word used to define for each circuit the acquisition of radio-chemical component characteristics (see the Section 1.3.5 for more details of radio-chemical component).

Steps 1 and 2 must be repeated as many times as there are circuits in the reactor.

Step 3: Definition of the modules which belong to several CIRCUIT modules: heat exchangers (EXCHANGER, SGTR), special links between elements of different circuits (EXHYLINK).

Step 4: Definition of circuits (CIRCUIT).

Steps 1 to 4 must be repeated as many for each system in the data block

Step 5: Definition of the modules which belong to several REACTOR modules: special links between elements of different reactors (EXHYLINK).

Step 6: Definition of reactors (REACTOR).

1.4.2 Executable block

The executable block manages the actions that are carried out on the reactor. These actions can be of two types: internal and external. The internal actions refer to the numerical solution of the problem in question, recalling gradually appropriate solvers and proceeding in steps of calculation. External actions are implemented by the user through directives. With these actions, it is possible to manage the output information, but also act on the objects described in the DATA BLOCK to modify these characteristics, for example by closing a valve which in the data block was initialized open, or to modify the boundary conditions, etc.. The command block consists of: *the initialization of the thermal hydraulic state for the entire reactor, the achievement of the initial steady state, and the transient scenario.*

The initialization is a mandatory step for any CATHARE calculation because any time step calculation requires the knowledge of the initial values of all the variables. To minimize the amount of data to enter and to facilitate this first calculation, this initialization step aims at reaching a plant steady step. The initialization order for each hydraulic circuit is defined with the PERMINIT directive. This directive reads the order of the elements of each circuit used to compute the initial state of the system. Then, the imposed thermal hydraulic state has to be defined. To perform this operation, the code needs to know the values of the main variables for, at least, one junction in each fluid zone of the circuit from which the initialization will be propagated to the entire zone. This corresponds, in the input deck, to the definition of a real constraint point (REALC operator). When the definition is complete, the initialization calculation can be launched using the GOPERM directive. This directive is used to trigger steady state computation of a reactor. The initialization procedure is performed in two steps. The first step, following the initialization order given by PERMINIT, calculates in each element the variable values which satisfy the stationary condition. The inlet conditions are propagated along the element taking into account a hydrostatic pressure correction. If there are walls, a conduction calculation will be done taking into account generating power or heat loss flux. All connected gadgets are taken into account during this calculation. The calculation is done to obtain a thermal hydraulic stationary state with the inlet junction calculated pressures being monitored with respect to the imposed values (REALC). Knowledge of the thermal-hydraulic variables for all the inlet junctions is thus required. This implies that if the inlet junction conditions are not given by elements that have already been calculated, then additional real constraint points have to be defined. Boundary conditions are not calculated during this step. The second step allows the user to reach an overall coherent state.

This is the stabilized solution of the standard transient calculation of ten time steps for the entire reactor (i.e. a calculation with time set to zero). During this step, contrary to the previous one, the boundary conditions (and then their models as defined in the data block) and the real exchanged power between circuits are taken into account.

The purpose of *the Stabilized transient* is to obtain a system at equilibrium with the required initial conditions (P at pressurizer, flowrate at secondary side, pump rotation speed, etc.).

Usually, this part of the input deck consists of a transient loop with regulations and with outlet condition tests set on a time step value to ensure the stability of the physical state obtained and its agreement with the imposed reference state (tests on physical variable values with respect to imposed values). This transient block may be performed with time set constant to 0 or not. Performing this phase with running time may be advantageous in order to post-treat the regulation results in order to check reactor convergence towards the desired state. Then, the RESETIME directive can be used to reset time to 0 before beginning the real transient scenario. Some regulation tools can be used but are not actually available in reactor plants or facility plants. For example, it is possible to regulate loop mass flow rates or flow distribution by changing pressure loss coefficients at volume junctions. It is also possible to regulate the temperature difference between a primary and a secondary circuit by introducing a fouling factor in the heat exchanger. In both cases, after convergence, the final values of the pressure loss coefficients or fouling factor have to be checked. Realistic values may be used.

The *Transient scenario* of the executable block is used to represent the actual reactor or experiment transients. Available directives may be sorted into different categories, such as the RESETIME directive, that is used to reinitialize the CATHARE calculation time as well as the time input deck local variable to zero.

Chapter 2

The Neptune CFD code

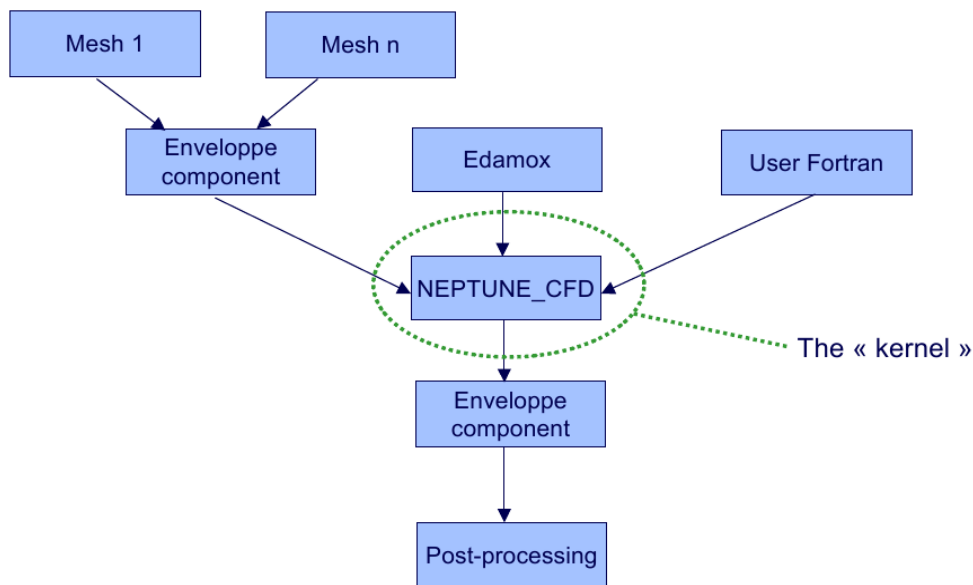


Figure 2.1: Modules of the NEPTUNE CFD

NEPTUNE.CFD is a three-dimensional two-fluid code for calculating multiphase or multifield flows at the local scale and in geometries that may be complex. It is developed for nuclear reactor applications in particular for three-dimensional computations of the main components of the reactors: cores, steam generators, condensers, and heat exchangers. This project is a joint research and development program between EDF (French utility), CEA (French Atomic Energy Commission), IRSN (French Nuclear Safety Institute), and AREVA-NP for nuclear reactor simulation tools. Based on a fully unstructured finite volume solver and on state-of-the-art physical modeling, the NEPTUNE.CFD code is currently being developed and validated against numerous

experimental data. NEPTUNE_CFD has also been chosen as a basis for the development of CFD tools within the European Project NURISM and NURISP, which aims at building an international shared software platform for nuclear thermal-hydraulics.

NEPTUNE can process from 1 to 20 fluid fields or phases [14]. In particular it can process water/steam flows with actual thermodynamic laws. The code can be used with meshes with all types of cell (element) and non-conforming connections with quality constraints. The code is cell-center type finite volume with calculation of colocalized gradients with reconstruction methods and distributed-memory parallelism by domain splitting. There are several physical models implemented in the code such as interface momentum transfer, interface energy transfer, turbulence, head losses and porosity. NEPTUNE, coded in Fortran 77 (the majority) and C (ANSI 1989) (procedural programming), is ported on LINUX and UNIX systems and it can be interfaced with the Code Saturne Enveloppe module for management of the pre-processing operations on the mesh, of the parallelism and of the post-processing files. Neptune is organized in modules as shown in Figure 2.1.

Edamox is the graphical user interface of NEPTUNE and the user Fortran module allows to define user function within the code. The kernel of the calculation is implemented in the NEPTUNE_CFD module. In version 1.0.8, NEPTUNE_CFD is interfaced with the Enveloppe module of Code Saturne [15], a component managing the pre-processing and post-processing of the calculation component, also referred to as the kernel. Enveloppe (also nicknamed ECS) can communicate directly with the kernel, or be run separately, for example to test a mesh. The kernel can also be used alone, but with reduced functions, i.e., in non-standard mesh format, mesh merging impossible, parallel mode forbidden.

2.1 Two-fluid model in NEPTUNE code

In this section, the mathematical model of the flows that can be simulated with the NEPTUNE_CFD module is presented. This includes the mass, momentum and energy balance equations in a general multi-field form, the interface transfer closure laws, the constitutive relations and the turbulence modeling [16].

2.1.1 Multi-field balance equations

The behavior of a fluid made of several physical phases or components can be modeled using the general Eulerian multi-field balance equations. These fields can represent many kinds of multiphase flow: distinct physical components (gas, liquid and solid particles), thermodynamic phases of the same component (liquid water and its vapor),

distinct physical components where some of which may be split into different groups (water and several groups of different diameter bubbles), different forms of the same physical components (a continuous liquid field, a dispersed liquid field, a continuous vapor field, a dispersed vapor field). The classical two fluid-model is in fact a two-field formulation for modeling two-phase flows. The several multi-fluid balance equations are obtained from the fundamentals conservation laws of physics, restricted to Newtonian mechanics: mass conservation, momentum conservation, and energy conservation. The second law of thermodynamics is not represented through a transport equation in the NEPTUNE CFD module. The above three conservation laws are written in a classical integro-differential form that is valid for arbitrary time and location within the continuum, except across the interfaces between two physical phases. At the interfaces, jump conditions derived from the continuous equations are written. If one wants to avoid the direct simulation in time and space of all the interfaces, an averaging procedure is needed. Equations for m fields that can be a physical phase or a model field of a physical phase, are written in a symbolic coordinate-free notation.

Mass balance equations

The multi-field mass balance equation for the field k is written as

$$\frac{\partial}{\partial t}(\alpha_k \rho_k) + \frac{\partial}{\partial x_i}(\alpha_k \rho_k U_{k,i}) = \Gamma_k, \quad (2.1)$$

with α_k, ρ_k, U_k , the volumetric fraction, the density and the mean velocity of phase k , respectively. Γ_k is the interface mass transfer rate on phase k , sum of all the other phases contributions

$$\Gamma_k = \sum_{p \neq k} \Gamma_{(p \rightarrow k)}^c + \Gamma_{(w \rightarrow k)}^{nuc}. \quad (2.2)$$

$\Gamma_{(p \rightarrow k)}^c$ is the interface mass transfer from phase p to phase k (bulk transfer). $\Gamma_{(w \rightarrow k)}^{nuc}$ represents the mass transfer contribution to phase k induced by wall nucleate boiling. In our model, these terms are calculated near heated walls and only affect liquid and steam phases, i.e., $k = 1, 2$, and verify

$$\Gamma_{(w \rightarrow 1)}^{nuc} + \Gamma_{(w \rightarrow 2)}^{nuc} = 0 \quad (2.3)$$

and

$$\Gamma_{(w \rightarrow 2)}^{nuc} \geq 0 \quad (2.4)$$

since steam is produced by nucleation. Conservation relations for mass and volume lead to

$$\sum_k \alpha_k = 1, \quad (2.5)$$

$$\sum_k \Gamma_k = 0 \quad (\text{since } \Gamma_{(p \rightarrow k)}^c + \Gamma_{(k \rightarrow p)}^c = 0). \quad (2.6)$$

Momentum equations

The multi-field momentum balance equation for the field k is first presented in its semi-conservative form (all the contributions are conservative except for the pressure gradient one)

$$\begin{aligned} \frac{\partial}{\partial t}(\alpha_k \rho_k U_{k,i}) + \frac{\partial}{\partial x_j}(\alpha_k \rho_k U_{k,i} U_{k,j}) = \\ \frac{\partial}{\partial x_j}(\alpha_k \tau_{k,ij} + \Sigma_{k,ij}^{Re}) - \alpha_k \frac{\partial P}{\partial x_i} + \alpha_k \rho_k g_i + \sum_{p \neq k} \left(I'_{(p \rightarrow k),i} + \Gamma_k U_{pk,i}^I \right) + \alpha_k S_k, \end{aligned} \quad (2.7)$$

with P the mean pressure and g_i acceleration due to gravity. The viscous stress tensor is defined by

$$\tau_{k,ij} = \mu_k \left(\frac{\partial U_i}{\partial x_j} + \frac{\partial U_j}{\partial x_i} - \frac{2}{3} \text{div}(U) \delta_{ij} \right). \quad (2.8)$$

where μ_k is the dynamic viscosity. $\Sigma_{k,ij}^{Re} = -\alpha_k \rho_k \langle U'_{k,i} U'_{k,j} \rangle_k$ is the turbulent stress tensor that has to be modeled or neglected when the flow is considered laminar. $S_k = S_k(\alpha_l, U_l, P)$ with $l = 1, \dots$ number of phases, is the external source terms such as head losses for instance (resistance forces due to porous medium) and U_{pk}^I is the interface velocity between phases p and k . $I_{(p \rightarrow k)} = \left(I'_{(p \rightarrow k),i} + \Gamma_k U_{pk,i}^I \right)$ represents the average interface momentum transfer rate from phase p to phase k , that accounts for mass transfer, drag force, added mass force, lift, etc, and complies with the local balance equations

$$I_{(p \rightarrow k)} + I_{(k \rightarrow p)} = 0. \quad (2.9)$$

$I'_{p \rightarrow k}$ is the part of the interface momentum transfer rate that remains after substitution of the mass transfer contribution.

The non-conservative form is obtained after decomposition of the non stationary term with respect to the mass balance equation, and dividing by the volumetric fraction. The result is the following

$$\rho_k \frac{\partial}{\partial t} U_{k,i} - U_{k,i} \frac{1}{\alpha_k} \frac{\partial}{\partial x_j} (\alpha_k \rho_k U_{k,i} U_{k,j}) =$$

$$\frac{1}{\alpha_k} \frac{\partial}{\partial x_j} (\alpha_k \tau_{k,ij} + \Sigma_{k,ij}^{Re}) - \frac{\partial P}{\partial x_i} + \rho_k g_i + \sum_{p \neq k} (J'_{(p \rightarrow k),i}) + S_{k,i}, \quad (2.10)$$

with

$$J'_{(p \rightarrow k),i} = \frac{I'_{(p \rightarrow k),i}}{\alpha_k}. \quad (2.11)$$

Energy equations

For the total enthalpy variable

$$H_k = e_k + \frac{1}{2} u_k^2 + \frac{P}{\rho_k}. \quad (2.12)$$

The energy equations in conservative form is written

$$\begin{aligned} \frac{\partial}{\partial t} (\alpha_k \rho_k H_k) + \frac{\partial}{\partial x_j} (\alpha_k \rho_k H_k U_{k,j}) = \\ \left[\frac{\partial}{\partial x_j} (\alpha_k U_{k,i} \tau_{k,ij}) \right] - \frac{\partial}{\partial x_j} (\alpha_k Q_{k,j}) + \alpha_k \frac{\partial P}{\partial t} + \\ [\alpha_k \rho_k U_{k,i} g_i] + \Pi_k + \varphi_{wall \rightarrow k} + \left[\sum_{p \neq k} I'_{(p \rightarrow k),i} + U_{k,i} \right], \quad (2.13) \end{aligned}$$

with $Q_k = -\lambda_k T_k$ and λ_k the thermal conductivity containing both molecular and turbulent contributions. $\varphi_{(wall \rightarrow k)}$ represents the heat exchanges with boundaries and is described by the nucleate boiling model. It takes into account bubble creation and agrees with

$$\sum_{k=1}^{nphase} \varphi_{(wall \rightarrow k)} = \varphi_{wall}, \quad \text{with } \varphi_{wall} \text{ the total flux imposed.} \quad (2.14)$$

Π_k is the bulk interface heat transfer, sum of the interface transfer between phase p and phase k , which complies with conservation relation

$$\Pi_k = \sum_{p \neq k} \Pi_{p \rightarrow k} \quad \text{with } \Pi_{(p \rightarrow k)} + \Pi_{(k \rightarrow p)} = 0. \quad (2.15)$$

Square bracket terms are not taken into account in the code but could be quite easily coded in the future.

The interface heat transfer between two phases are divided into two contributions, one related to mass transfer term, the second independent of the mass transfer

$$\Pi_{p \rightarrow k} = \Gamma_{p \rightarrow k}^c H_{p \rightarrow k}^\sigma + \Pi'_{p \rightarrow k}. \quad (2.16)$$

In order to verify the conservation relation, two choices are possible for the jump of enthalpy for the two phases: it may be the same or independent. If the jumps of enthalpy is the same for the two phases then $H_{p \rightarrow k}^\sigma = H_{k \rightarrow p}^\sigma = H^\sigma$ so that the following relation must be verified : $\Pi'_{p \rightarrow k} + \Pi'_{k \rightarrow p} = 0$. If the the jump of enthalpy are independent then in this case the following relation between heat and mass transfers must be verified

$$\Gamma_{p \rightarrow k}^c = -\frac{\Pi'_{p \rightarrow k} + \Pi'_{k \rightarrow p}}{H_{p \rightarrow k}^\sigma - H_{k \rightarrow p}^\sigma}. \quad (2.17)$$

Notice that in the case of two-phase water-steam flows, this last model is generally used with

$$H_{2 \rightarrow 1}^\sigma = H_1, \quad H_{1 \rightarrow 2}^\sigma = H_2 \quad (2.18)$$

and introducing independent models for heat transfers, for each phase we have

$$\Pi'_{2 \rightarrow 1} = \Pi_1'^{w/s}, \quad \Pi'_{1 \rightarrow 2} = \Pi_2'^{w/s} \quad (2.19)$$

so the condensation rate is simply given by

$$\Gamma_1^c = \frac{\Pi_1'^{w/s} + \Pi_2'^{w/s}}{H_2 - H_1}. \quad (2.20)$$

The non-conservative form is obtained after decomposition of the unsteady term with respect to the mass balance equation, and after division by the volumetric fraction

$$\begin{aligned} \rho_k \frac{\partial}{\partial t} H_k - H_k \frac{1}{\alpha_k} \frac{\partial}{\partial x_j} (\alpha_k \rho_k U_{k,j}) + \frac{1}{\alpha_k} \frac{\partial}{\partial x_j} (\alpha_k \rho_k H_k U_{k,j}) = \\ - \frac{1}{\alpha_k} \frac{\partial}{\partial x_j} (\alpha_k Q_{k,j}) + \frac{\partial P}{\partial t} + \rho_k U_{k,i} g_i + \frac{\varphi_{wall \rightarrow k}}{\alpha_k} + \\ \frac{1}{\alpha_k} \sum_{p \neq k} \left[\Pi'_{(p \rightarrow k)} + \Gamma_{(p \rightarrow k)}^c H_{(p \rightarrow k)}^\sigma \right] - \frac{\Gamma_k H_k}{\alpha_k}. \quad (2.21) \end{aligned}$$

Notice that, in the standard case where $H_{(p \rightarrow k)}^\sigma$ is taken equal to H_k , and where nucleate transfer does not exist ($\sum \Gamma_{p \rightarrow k}^c = \Gamma_k$), the mass transfer terms do not appear in the equation.

2.1.2 Interface transfer closure laws

The interface momentum transfer between phases k and p , is written as a symmetric extension of the closure obtained for fluid-inclusions (bubbles, drops or solid particles). It can be split into laminar and turbulent contributions.

Laminar contribution. The laminar part is the sum of the drag force, the added mass force, the lift force and additional user forces. Drag, added mass and lift are independently usable in the code and must be understood as forces between the first phase ($k = 1$), chosen as the carrier fluid (or continuous phase), and other phases. The general form is

$$\begin{aligned} I_{1 \rightarrow p}^{(lam)} = & -(\alpha_1 \alpha_p) F_D^{1p} V_r^{1p} - (\alpha_1 \alpha_p) C_A^{1p} \left[\frac{dV_r^{1p}}{dt} \right] \\ & - (\alpha_1 \alpha_p) L^{1p} (U_p - U_1) \wedge rot(U_1), \end{aligned} \quad (2.22)$$

with F_D^{1p} the drag coefficient between phases 1 and p . $V_r^{1p} = U_p - U_1 - V_d^{1p}$ is the averaged value of the local relative velocity between phases 1 and p , expressed in terms of the total relative mean velocity and a drifting velocity, V_d^{1p} due to the correlation between the instantaneous distribution of dispersed particles and the turbulence structure of the carrier fluid. Note that the laminar contribution only takes the laminar part of the relative velocity: $U_p - U_1$. C_A^{1p} is the added mass coefficient between phases 1 and p and dV_r^{1p}/dt the relative acceleration, symmetrically handled as

$$\frac{dV_{r,i}^{1p}}{dt} = \left(\frac{\partial U_{p,i}}{\partial t} + U_{p,j} \frac{\partial U_{p,i}}{\partial x_j} \right) - \left(\frac{\partial U_{1,i}}{\partial t} + U_{1,j} \frac{\partial U_{1,i}}{\partial x_j} \right). \quad (2.23)$$

Finally L^{1p} is the lift coefficient.

Drag closure law. The closure law for the drag coefficient F_D^{1p} is not general and has to be adapted to the simulated flow. Several choices are however proposed.

In the case of *isolated (diluted) spherical inclusions* such as bubbles, droplets or solid particles p represents the dispersed phase and 1, the continuous phase. The drag coefficient is written in terms of the particle drag-relaxation time scale

$$F_D^{1p} = \frac{\rho_p}{\alpha_1} \frac{1}{\tau_p^F}, \quad \frac{1}{\tau_p^F} = \frac{\rho_1}{\rho_p} \frac{3}{4} \frac{C_D}{d_p} < |V_r^{1p}| >_p, \quad C_D = \frac{24}{Re_p} [1 + 0.15 Re_p^{0.687}]. \quad (2.24)$$

The particulate Reynolds number is based on the particle diameter and on the relative velocity modulus that takes into account turbulence and fluctuating velocities covariance

$$Re_p = \rho_1 \frac{|V_r^{1p}| d_p}{\mu_1}, \quad |V_r^{1p}| = \left((\vec{U}_p - \vec{U}_1 - \vec{V}_d^{1p})^2 + 2q_1^2 - q_{1p} + 2q_p^2 \right)^{1/2}. \quad (2.25)$$

In the case of *separated phases*, used for liquid-gas separated flows, this Simmer-like model considers either dispersed gas bubbles in a continuous liquid flow, or dispersed

liquid droplets in a continuous gas flow with regard to the volumetric fraction

$$\text{bubbles } (\alpha_p < 0.3) : F_D^{1p} = F_D^{bb}(\alpha_p) = \frac{\rho_p}{\alpha_1} \frac{1}{\tau_p^F}, \quad (2.26)$$

$$\text{droplets } (\alpha_p > 0.7) : F_D^{1p} = F_D^{dr}(\alpha_p) = \frac{\rho_1}{\alpha_p} \frac{1}{\tau_1^F}, \quad (2.27)$$

$$\text{mixing } (0.3 < \alpha_p < 0.7) : F_D^{1p} = \frac{0.7 - \alpha_p}{0.7 - 0.3} F_D^{bb}(0.3) + \frac{\alpha_p - 0.3}{0.7 - 0.3} F_D^{dr}(0.7), \quad (2.28)$$

limits 0.3 and 0.7 being arbitrary.

Ishii correlation, used in the case of bubbly flow, with automatic calculation of the drag coefficient, based on the local regime.

Added mass closure law. The closure law for the added mass coefficient C_A^{1p} is not general and has to be adapted to the simulated flow. Different choices are proposed

Standard EDF model implemented for isolated (diluted) spherical inclusions

$$C_A^{1p} = \frac{1}{2} \frac{\rho_1}{\alpha_1^*}, \text{ with } \alpha_1^* = \max(\alpha_1, 0.1). \quad (2.29)$$

Melt model

$$C_A^{1p} = \frac{1}{2} (\alpha_1 \rho_1 + \alpha_p \rho_p). \quad (2.30)$$

Separated phase model, generalization of the standard model, inspired by the drag coefficient form used for separated phase flows

$$\text{bubbles } (\alpha_p < 0.3) : C_A^{1p} = C_A^{bb} = \frac{1}{2} \frac{\rho_1}{\alpha_1}, \quad (2.31)$$

$$\text{droplets } (\alpha_1 < 0.3) : C_A^{1p} = C_A^{dr} = \frac{1}{2} \frac{\rho_p}{\alpha_p}, \quad (2.32)$$

$$\text{mixing } (0.3 < \alpha_p < 0.7) : C_A^{1p} = \frac{0.7 - \alpha_p}{0.7 - 0.3} C_A^{bb}(0.3) + \frac{\alpha_p - 0.3}{0.7 - 0.3} C_A^{dr}(0.7), \quad (2.33)$$

limits 0.3 and 0.7 being arbitrary.

Standard CEA Zuber model implemented for two-phases bubbly flows (any regime)

$$C_A^{1p} = \frac{1}{2} \frac{\rho_1}{\alpha_1^*} \left(\frac{1 + 2\alpha_p^*}{\alpha_1^*} \right), \text{ with } \alpha_1^* = \max(\alpha_1, 0.1), \alpha_p^* = \min(\alpha_p, 0.1). \quad (2.34)$$

Turbulent contribution. The turbulent contribution of the interface momentum transfer depends on the turbulence modeling of each phase. It will only be activated if the turbulence of the continuous phase (phase 1) is $k - \epsilon$ model and the turbulence of the

dispersed phase ($p > 1$) are given by the Tchen's local equilibrium model, leading to an algebraic closure for the particles turbulent energy $q_p^2 = 0.5 \langle U'_{p,i} U'_{p,i} \rangle$ and the fluid-particles covariance $q_{1p} = \langle U'_{1,i} U'_{p,i} \rangle$.

$$I'_{(1 \rightarrow p)}^{(turb)} = \alpha_1 \alpha_p F_D^{1p} V_d^{1p} - \frac{\alpha_1 C_A^{1p}}{\rho_1} \nabla \left(\alpha_p \rho_1 \left[\frac{2}{3} q_p^2 - \frac{1}{3} q_{1p} \right] \right) + \alpha_p \langle \nabla \sigma'_1 \rangle_p. \quad (2.35)$$

The first contribution is the part of the drag effect due to drifting velocity, with V_d^{1p} given by

$$V_d^{1p} = - \frac{\tau_{1p}^t q_{1p}}{3} \frac{\nabla \alpha_p}{\alpha_1 \alpha_p}, \quad (2.36)$$

τ_{1p}^t being the fluid-particle turbulent time scale.

The second contribution is the fluctuating part of the added mass force.

The last contribution is the fluctuating pressure term due to the correlation between the particles distribution and the carrier phase constraint tensor. Using extension of the classical model used for bubbly flows, it is written using the added mass coefficient

$$\alpha_p \langle \nabla \sigma'_1 \rangle_p = 2 \frac{\alpha_1 \alpha_p C_A^{1p}}{\rho_1} \left(\frac{\nabla \alpha_p \rho_1 q_{1p} / 3}{\alpha_p} - \frac{\nabla \alpha_1 \rho_1 2 q_1^2 / 3}{\alpha_1} \right). \quad (2.37)$$

Developing all these terms and neglecting the gradients of turbulence, one can show that a simplified form of this turbulent contribution can be re-written as a turbulent dispersive term

$$I'_{(1 \rightarrow p)}^{(turb)} = -C_p^{DT} \rho_1 q_1^2 \nabla \alpha_p. \quad (2.38)$$

Notice that such a modeling is possible in the code and does not require any assumption on the dispersed phase turbulence. Nevertheless, the turbulence of the continuous phase has to be described by a $k - \epsilon$ model.

2.1.3 Bulk interface heat and mass transfer

General user case

It has been seen in the previous section that interface heat and mass transfer can be either independent or dependent, depending on the choice of the enthalpy jump in the heat and mass transfers formulation. In the first case, three user FORTRAN files can be implemented. The first regards the heat transfer between phase p and k , which agree with $\Pi'_{(p \rightarrow k)} + \Pi'_{(k \rightarrow p)} = 0$. The standard form implemented is written in terms of the temperature difference between two phases

$$\Pi'_{(p \rightarrow k)} = \zeta_{kp} (T_p - T_k) \quad \text{with} \quad \zeta_{kp} = \zeta_{pk} \geq 0 \quad \text{the heat transfer coefficient.} \quad (2.39)$$

The second is related to the jump of enthalpy, verifying $H_{(p \rightarrow k)}^\sigma = H_{(k \rightarrow p)}^\sigma$ and finally the third concerns the mass transfer between phase p and k verifying $\Gamma_{(p \rightarrow k)} + \Gamma_{(k \rightarrow p)} = 0$.

In this form, one can have some mass transfer without heat transfer and some heat transfer without mass transfer. The case of dependent heat and mass transfer corresponds to the Water-Steam transfer models. In this frame, one can separate direct heat transfer at liquid-vapor interface and wall heat transfer with nucleate boiling.

Interface Steam-Water transfers

In this part, a two-phase liquid-vapor flow is supposed. The liquid phase is located by index 1 and the vapor phase by index 2. In this model, mass transfers directly depend on heat transfers. Different models are available for $\Pi_1'^{w/s}$ and $\Pi_2'^{w/s}$.

Water Phase. In this phase the constant time scales and the different models must be defined. The *Constant time scale return to saturation* is defined by

$$\Pi_1'^{w/s} = f(\alpha_1) \frac{\rho_1 C_{p1}}{\tau_1} (T_{sat} - T_1), \quad (2.40)$$

τ_1 is the time constant (s) given by the user, $f(\alpha_1)$ is a pondering function which can takes different values 1, α_1 , α_2 or $\alpha_1 * \alpha_2$.

The *Bulk model (ASTRID-like model) for diluted bubbly flows* is set to

$$\Pi_1'^{w/s} = \frac{6\alpha_2 Nu \lambda_1}{d_2^2} (T_{sat} - T_1), \quad (2.41)$$

with *Nusselt* number definition

$$Nu = 2 + 0.6(Re)^{1/2}(Pr)^{1/3}, \quad Re = \rho_1 \frac{d_2 |V_r|}{\mu_1}, \quad Pr = \frac{\mu_1 C_{p1}}{\lambda_1}, \quad (2.42)$$

and relative velocity $|V_r|$ calculated for laminar or turbulent velocity fields.

The *Hugues-Duffey model for turbulent stratified flows* is given by

$$\Pi_1'^{w/s} = a_i \zeta_1 (T_{sat} - T_1), \quad (2.43)$$

with a_i being the interface area (m^{-1}) supposed to be equal to $|\nabla \alpha_1|$ (in stratified areas), and ζ_1 , the heat transfer coefficient, calculated from

$$\zeta_1 = \frac{2}{\pi} \frac{\lambda_1}{\mu_1} \rho_1 V_L^* \sqrt{Pr}, \quad V_L^* = \max(V_L, 0.01), \quad V_L = \min(|U_1|, C_\mu^{0.25} \sqrt{q_1^2}).$$

Since this model only takes into account condensation effect at the water-steam interface, it has been completed by a residual droplet term (in the upper zone where $\alpha_1 < 0.1$) taken as a return to saturation term, with a constant time scale τ_1 arbitrary equal to $1s$, and the pondering function $f(\alpha_1)$ equal to α_2 .

The *Flashing model* (CATHARE1D-like model) is defined as

$$\Pi_1^{w/s} = -COEF(h_1 - h_1^{sat}) \text{ if } h_1 > h_1^{sat}. \quad (2.44)$$

The correlation for *COEF* takes into account a delay to saturation

$$COEF = FLASH * 1.210^{-8} * \rho_1^2 * \frac{U_1^2 + V_0^2}{\mu_1} * exp(4.5\alpha_2), \quad V_0 = 4 \quad (2.45)$$

$$\zeta = \sqrt{\left(\frac{\alpha_2}{0.02}\right)^2 + \left(\frac{h_1 - h_1^{sat}}{\delta h}\right)^2} \quad (2.46)$$

$$CC = 0.001 \frac{|h_1 - h_1^{sat}|}{\delta h}, \quad \delta h = 1500 * exp(1.253 * 10^{-6} h_1). \quad (2.47)$$

Default $\rightarrow FLASH = 1$,

$\zeta \leq 1 \rightarrow FLASH = CC$,

$1 < \zeta < 2 \rightarrow FLASH = CC + (1 - CC) * (5 - 12\zeta + 9\zeta^2 - 2\zeta^3)$.

Steam phase. In this phase the constant time scales and the sub-cooled model must be defined. *The constant time scale return to saturation* is defined as

$$\Pi_2^{w/s} = f(\alpha_2) \frac{\rho_2 C p_2}{\tau_2} (T_{sat} - T_2). \quad (2.48)$$

τ_2 is the time constant (s) given by the user, $f(\alpha_2)$ is a pondering function which can takes different values $1, \alpha_1, \alpha_2$ or $\alpha_1 * \alpha_2$. In this CATHARE1D-like model, a strong return to saturation is enforced if the steam temperature remains lower than the saturation temperature

$$T_2 < T_{sat} \rightarrow \Pi_2^{w/s} = f(\alpha_2) * 10^8 (T_{sat} - T_2)^2, \quad (2.49)$$

$$T_2 > T_{sat} \rightarrow \Pi_2^{w/s} = f(\alpha_2) \frac{\rho_2 C p_2}{\tau_2} (T_{sat} - T_2). \quad (2.50)$$

In this numerical model, the constant time scale is replaced by the local time-step

$$\Pi_2^{w/s} = \alpha_2 \frac{\rho_2 C p_2}{\nabla t} (T_{sat} - T_2). \quad (2.51)$$

2.1.4 Nucleate boiling model

Basic computation of the flux heat

In the lack of any global understanding of the processes involved in the heat transfer at the wall, a first model for the wall heat transfer mechanisms is implemented in the NEPTUNE_CFD code. Closures involving the parameters, namely the mean bubble frequency, the mean waiting time between bubble departures, the mean bubble maximum equivalent diameter and the active site spatial density, should be provided. The two steps of this model are presented below: the condition for on-setting boiling and the heat flux calculation.

In order to obtain satisfactory results, the incipient boiling point (in forced convection) has to be determined accurately. To do this, the widely used Hsus criterion is chosen [17]. According to this criterion, a bubble will grow from a vapor embryo occupying a cavity if the liquid temperature at tip of the embryo is at least equal to the saturation temperature corresponding to the bubble pressure. The single phase temperature profile in the viscous sub-layer allows to obtain the relations described as follow. If cavities of all sizes containing vapor embryo are available (which means that even the largest cavities contain vapor embryo), the wall superheat at boiling incipience ($T_{wall} - T_{sat}$) and the wall heat flux ϕ_{wall} are related by

$$T_{wall} - T_{sat} = T_{crit1} = \left(\frac{8\sigma T_{sat} \varphi_{wall}}{H_{lat} \rho_{sat} \lambda_1} \right)^{1/2}, \quad (2.52)$$

while the activated cavity radius r_{cl} is

$$r_{cl} = \frac{\lambda_1 T_{crit1}}{2\varphi_{wall}}. \quad (2.53)$$

When the wall temperature reaches the critical value, the cavities of radius equal to r_{cl} are activated. Then, as the temperature still increases, smaller cavities are activated too. If the radius r_{cmax} of the largest cavity available (allowed to contain vapor embryo) on the surface is smaller than r_{cl} , the required wall superheat is higher

$$T_{wall} - T_{sat} = T_{crit2} = \frac{\varphi_{wall}}{\lambda_1} r_{cmax} + \frac{2\sigma T_{sat}}{H_{lat} \rho_{sat} r_{cmax}}. \quad (2.54)$$

In a first simplified approach and following the analysis of Kurul and Podowski [18], the boiling heat flux splits into three terms, a single phase flow convective heat flux at the fraction of the wall area unaffected by the presence of bubbles, a quenching heat flux where bubble departures bring cold water in contact with the wall periodically and a vaporization heat flux needed to form the vapor phase.

The wall surface unit is split into two parts: an area influenced by bubble departure A_Q and a single phase area A_C with the relation $A_Q + A_C = 1$.

A_Q is the sum of the areas of influence of each bubble over the unit surface. Neglecting the overlapping areas of influence between adjacent bubbles, A_Q is written

$$A_Q = \min(1, \pi D_m^2 n / 4), \quad (2.55)$$

where n is the active site density and D_m is the bubble diameter departure.

A classical law of single phase flow heat transfer at the wall is used to predict the flux

$$\varphi_C = A_C h_{log}(T_{wall} - T_\delta), \quad (2.56)$$

where δ refers to a point in the fluid turbulent sub-layer. h_{log} represents the heat transfer within the thermal boundary layer.

The quenching heat flux is modeled as the mean value of a transient conductive heat flux supplied to a semi infinite medium at external temperature T_δ , during the waiting period t_Q between the departure of a bubble and the beginning of growth of the following one

$$\varphi_Q = A_Q t_Q f \frac{2\lambda_1(T_{wall} - T_\delta)}{\sqrt{\pi a_l t_Q}}, \quad (2.57)$$

where a_l is the liquid thermal diffusivity, f is the bubble departure frequency, $t_Q = 1/f_Q$ is the time fraction during which quenching occurs. The use of a pure convective process to model quenching is not well established, since the external convective heat flux often has a time scale comparable to it. The vaporization heat flux is assumed to be proportional to the volume V_b of the bubble

$$\varphi_E = f V_b \rho_2 (H_2^\sigma - H_1^\sigma) n, \quad (2.58)$$

where H_2^σ and H_1^σ are the enthalpy jumps defined in 2.1.1 ($H_1^\sigma = H_{(2 \rightarrow 1)}^\sigma$, $H_2^\sigma = H_{(1 \rightarrow 2)}^\sigma$). The volume of a bubble is

$$V_b = \frac{\pi D_m^3}{6}. \quad (2.59)$$

It means that the net heat flux used to form vapor is supposed to arise from the wall. This approximation is well adapted for subcooled boiling, while for saturated boiling, energy is also received at the upper part of the bubbles. Figure 2.2 shows the boiling heat flux scheme of Kurul & Podowski. Provided coherent closure relations for n , D_m , f and t_Q are given, and the radius r_{cmax} is estimated, we have a closed model of the on-off boiling conditions associated with a given heat flux. The density of active sites

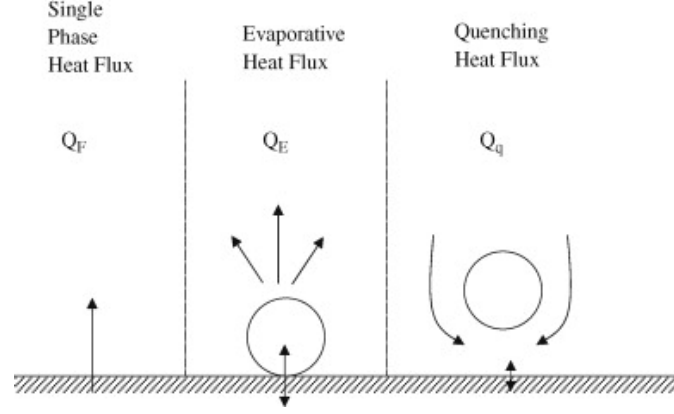


Figure 2.2: Boiling heat flux at the wall

is :

$$n = (210(T_{wall} - T_{sat}))^{1.8}. \quad (2.60)$$

The frequency is

$$f = \sqrt{\frac{4g(\rho_1 - \rho_2)}{3\rho_1 D_m}} = \frac{1}{t_Q}, \quad (2.61)$$

for the time t_Q , the time of bubble growth is neglected

$$t_Q = 1/f. \quad (2.62)$$

The bubble diameter is

$$D_m = 2.4210^{-5} P^{0.709} \frac{a}{\sqrt{b\phi}}, \quad (2.63)$$

with

$$a = \frac{(T_{wall} - T_{sat})\lambda_S}{2\rho_2 H_{lat} \sqrt{\pi a_S}}, \quad b = \frac{(T_{sat} - T_\zeta)}{2(1 - \frac{\rho_2}{\rho_1})}, \quad (2.64)$$

and

$$\phi = \begin{cases} \left(\frac{U_\zeta}{U_0}\right)^{0.47} & \text{if } U_\zeta > U_0, \\ 1 & \text{if } U_\zeta < U_0, \end{cases} \quad (2.65)$$

where $U_0 = 0.61m/s$ and s refers to the solid wall. This correlation has been determined in subcooled water flows [19].

Generalization of the heat flux decomposition model

In order to account for the wall burning out phenomenon, in this section a phenomenological function f_{α_1} is proposed by introducing the different contributions on phases 1

(water) and 2 (steam), and defined as

$$\begin{aligned}\varphi_{wall} &= \varphi_{wall \rightarrow 1} + \varphi_{wall \rightarrow 2}, \\ \varphi_{wall \rightarrow 1} &= f_{\alpha_1} \varphi_1 - \Gamma_w^{nuc} H_1^\sigma, \\ \varphi_{wall \rightarrow 2} &= f_{\alpha_2} \varphi_2 + \Gamma_w^{nuc} H_2^\sigma,\end{aligned}\tag{2.66}$$

where φ_1 is the energy part given to the phase 1 (water) and φ_2 is the energy part given to the phase 2 (steam). These fluxes are of diffusive nature. Γ_w^{nuc} is the mass transfer by wall nucleation ($= \Gamma_{(w \rightarrow 2)}^{nuc} = -\Gamma_{(w \rightarrow 1)}^{nuc}$). H_1^σ and H_2^σ are the enthalpy jumps related to the mass transfer (see 2.1.1) ($H_1^\sigma = H_{(2 \rightarrow 1)}^\sigma$, $H_2^\sigma = H_{(1 \rightarrow 2)}^\sigma$). f_{α_1} only depends on α_1 ($f_{\alpha_2} = 1 - f_{\alpha_1}$) and must satisfy to

$$f_{\alpha_1}(\alpha_1) \rightarrow 1 \text{ if } \alpha_1 \rightarrow 1, \quad f_{\alpha_1}(\alpha_1) \rightarrow 0 \text{ if } \alpha_1 \rightarrow 0,\tag{2.67}$$

and

$$\frac{f_{\alpha_1}(\alpha_1)}{\alpha_1} \rightarrow 0 \text{ if } \alpha_1 \rightarrow 0, \quad \frac{1 - f_{\alpha_1}(1 - \alpha_1)}{\alpha_1} \rightarrow 0 \text{ if } \alpha_1 \rightarrow 1.\tag{2.68}$$

The choice selected in NEPTUNE_CFD is $\alpha_{crit} = 0.2$ and then f_{α_1} is

$$\alpha_1 > \alpha_{crit} \rightarrow f_{\alpha_1} = 1 - \frac{1}{2} \exp[-20(\alpha_1 - \alpha_{crit})],\tag{2.69}$$

$$\alpha_1 < \alpha_{crit} \rightarrow f_{\alpha_1} = \frac{1}{2} \left(\frac{\alpha_1}{\alpha_{crit}} \right)^{20\alpha_{crit}}.\tag{2.70}$$

We will notice that the classical choice $f_{\alpha_1} = 1$ is also available.

The *diffusive contribution* part given to the vapor phase, namely φ_2 , is predicted by a classical law of single phase flow heat transfer at the wall

$$\varphi_2 = h_{log}^{vap} [T_{wall} - T_2].\tag{2.71}$$

As concerns the liquid diffusive part, φ_1 is divided into two terms

$$\varphi_1 = \varphi_C + \varphi_Q.\tag{2.72}$$

The *mass transfer by nucleation* is expressed as

$$\Gamma_{(w \rightarrow 1)}^{nuc} = f_{\alpha_1} f V_b \rho_2 * n.\tag{2.73}$$

The vaporization heat flux φ_E is related to the mass transfer and is connected to the

total heat flux φ_{wall} by

$$\varphi_{wall} = f_{\alpha_1}(\varphi_C + \varphi_Q + \varphi_E) + (1 - f_{\alpha_1})\varphi_2. \quad (2.74)$$

When T_δ tends towards T_{sat} , b tends to towards 0 and the bubble diameter tends towards infinity. To avoid this problem, the Stanton number is used and it is defined by

$$St = \frac{\varphi_{wall}}{\rho_1 C p_1 (T_{sat} - T_\delta) U_\delta}. \quad (2.75)$$

If $St < St_{lim}$, the last definition of b is considered. If $St > St_{lim}$, the b definition is replaced by

$$b = \frac{\varphi_{wall}}{2(1 - \frac{\rho_2}{\rho_1}) \times St_{lim} \times \rho_1 C p_1 U_\delta}, \quad (2.76)$$

with $St_{lim} = 0.0065$. This theory has been dedicated to boiling flows in tubes which provide small values of U_δ .

2.1.5 Turbulent modeling

For each phase k , the Reynolds stress tensor is closed, using a Boussinesq-like hypothesis

$$\langle \rho_k U''_{k,i} U''_{k,j} \rangle_k = -\mu_k^t \left[\frac{\partial U_{k,i}}{\partial x_j} + \frac{\partial U_{k,j}}{\partial x_i} \right] + \frac{2}{3} \delta_{ij} \left[\rho_k q_k^2 + \mu_k^t \frac{\partial U_{k,m}}{\partial x_m} \right], \quad (2.77)$$

introducing μ_k^t and q_k^2 the turbulent viscosity and the turbulent kinetic energy of the phase

$$q_k^2 = \frac{1}{2} \langle U'_{k,i} U'_{k,j} \rangle_k.$$

Basically the code uses two main turbulence models, the $q_k^2 - \epsilon_k$ and the local equilibrium model.

The $q_k^2 - \epsilon_k$ model is an extension of the classical $k - \epsilon$ model, used on single phase flows. It can be chosen to describe the turbulence of a continuous phase, coupled with dispersed phases such as bubbles or droplets, or with an other continuous phase (stratified two-phase flows). The transport equations system on the turbulent energy and the turbulent viscous dissipation is written in the following non-conservative form

$$\rho_k \left[\frac{\partial q_k^2}{\partial t} + U_{k,i} \frac{\partial q_k^2}{\partial x_i} \right] = \frac{1}{\alpha_k} \frac{\partial}{\partial x_j} \left[\alpha_k \frac{\mu_k^t}{\sigma_q} \frac{\partial q_k^2}{\partial x_j} \right] + \rho_k (Prod_k + G_k - \epsilon_k) + \Pi_{q_k}, \quad (2.78)$$

$$\rho_k \left[\frac{\partial \epsilon_k}{\partial t} + U_{k,i} \frac{\partial \epsilon_k}{\partial x_i} \right] = \frac{1}{\alpha_k} \frac{\partial}{\partial x_j} \left[\alpha_k \frac{\mu_k^t}{\sigma_\epsilon} \frac{\partial \epsilon_k}{\partial x_j} \right] \quad (2.79)$$

$$+ \rho_k \frac{\epsilon_k}{q_k^2} (C_{\epsilon_1} Prod_k + C_{\epsilon_1} \max(G_k, 0) - C_{\epsilon_2} \epsilon_k) + C_{\epsilon_4} \frac{\epsilon_k}{q_k^2} \Pi_{q_k},$$

where μ_k^t is the turbulent dynamic viscosity defined as

$$\mu_k^t = C_\mu \rho_k \frac{(q_k^2)^2}{\epsilon_k}, \quad C_\mu = 0.09. \quad (2.80)$$

$Prod_k$ represents the (positive) production contribution due to the mean velocity gradients

$$Prod_k = - \langle U'_{k,i} U'_{k,j} \rangle \frac{\partial U'_{k,i}}{\partial x_j}, \quad (2.81)$$

and G_k is a stratification attenuation term modeling the correlation between fluctuating density and velocity. The closure form assumes a gravity equilibrium

$$G_k = - \frac{\nu_k^t}{Pr^t} \frac{1}{\rho_k} \frac{\partial \rho_k}{\partial x_i} g_i \quad \text{with} \quad Pr^t = 0.9. \quad (2.82)$$

Notice that this contribution can only be positive in the dissipation equation. $C_{\epsilon_1} = 1.44$ and $C_{\epsilon_2} = 1.92$ are the two classical constants taken from the single phase flow model. Π_{q_k} represents the (production or destruction) influence of the $nphas - 1$ other phases, i.e. the turbulent contribution of combined drag and added mass terms

$$\Pi_{q_k} = \sum_{p \neq k} \Pi_{q_{p \rightarrow k}}, \quad (2.83)$$

$$\Pi_{q_{p \rightarrow k}} = \alpha_p F_D^{kp} \frac{\rho_p}{\rho_p + \alpha_k C_A^{kp}} (q_{kp} - 2q_k^2) + \alpha_p F_D^{kp} V_{d,i}^{kp} (U_{p,i} - U_{k,i} - V_{d,i}^{kp}), \quad (2.84)$$

with V_d^{kp} the drifting velocity already defined, $q_{kp} = \langle U_{k,i} U_{p,i} \rangle$ the covariance of the fluctuating velocities of phases k and p that will be either modeled or neglected. The multiplicative constant C_{ϵ_4} used in the dissipation equation is equal to 1.2.

The Local equilibrium model (extended Tchen's theory assumption) is an algebraic model, developed in the framework of Tchen's theory ([20]) and used for dilute dispersed phase, i.e. bubbles or droplets transported by a continuous phase. The main assumption here is that the continuous phase is the first one $p = 1$, and its turbulence is given by a $k - \epsilon$ model. With this assumption, the turbulent kinetic energy q_k^2 and the covariance q_{1k} of the dispersed phase $k > 1$ are calculated from the turbulent kinetic energy q_1^2

$$q_k^2 = q_1^2 \left[\frac{b^2 + \eta_r}{1 + \eta_r} \right] \quad q_{1k} = 2q_1^2 \left[\frac{b + \eta_r}{1 + \eta_r} \right], \quad (2.85)$$

where b and η_r are functions of drag and added mass coefficient, and two specific time scales

$$b = \frac{\rho_1 + \alpha_1 C_A^{1k}}{\rho_k + \alpha_1 C_A^{1k}} \quad \eta_r = \frac{\tau_{1k}^t}{\tau_{1k}^F}. \quad (2.86)$$

τ_{1k}^F is the characteristic time scale of the momentum transfer rate between 1 and k , i.e. the particle relaxation time scale

$$\tau_{1k}^F = \frac{\alpha_1 C_A^{1k} + \rho_k}{\alpha_1 F_D^{1k}}. \quad (2.87)$$

τ_{1k}^t represents the time scale of the continuous phase turbulence, viewed by the dispersed phase (or the fluid-particle turbulent time scale) that takes into account crossing trajectories effect [20], [21]

$$\tau_{1k}^t = \frac{\tau_1^t}{\sigma_\alpha} [1 + C_\beta \xi_r^2]^{-\frac{1}{2}}, \quad \tau_1^t = \frac{3}{2} C_\mu \frac{q_1^2}{\epsilon_1}, \quad \xi_r = \frac{\langle |\vec{V}_r| \rangle_2}{\sqrt{\frac{2}{3} q_1^2}}, \quad \vec{V}_r = \vec{U}_k - \vec{U}_1 - \vec{V}_d^{1k}.$$

C_β is the crossing trajectory coefficient, taken equal to 1.8.

2.2 Numerical discretization

In this section, an overview of the numerical algorithm used in NEPTUNE CFD code to solve conservation equations on mass, momentum and energy is given [16]. The main idea is a fractional step method that leads either to use linear solvers or direct $nphas * nphas$ matrix inversion. The main interest of the method is the so-called *alpha-pressure-energy cycle* that ensures conservative of mass and energy and allows strong interface source term coupling. The algorithm is compressible and allows variation of density (in function of pressure and enthalpy) during a time step. Moreover, all the variables are located at the center of the cells.

2.2.1 Momentum equations

Basic equation. The momentum equations are solved using the implicit for as possible. The final equation is the following one, that will be split in fractional steps

$$\rho_k^n \frac{U_{k,i}^{n+1} - U_{k,i}^n}{\Delta t} - U_{k,i}^{n+1} \frac{1}{\alpha_k^n} \frac{\partial}{\partial x_j} (\alpha_k^n \rho_k^n U_{k,j}^n) + \frac{1}{\alpha_k^n} \frac{\partial}{\partial x_j} (\alpha_k^n \rho_k^n U_{k,i}^{n+1} U_{k,j}^n) = \frac{1}{\alpha_k^n} \frac{\partial}{\partial x_j} (\alpha_k^n \tau_{k,ij}^{n+1} + \Sigma_{k,ij}^{Re^{n+1}}) - \frac{\partial P^{n+1}}{\partial x_i} + \rho_k^n g_i + \sum_{p \neq k} J'_{(p \rightarrow k),i}^{n+1} + S_{k,i}^{n+1}. \quad (2.88)$$

In this sub-step, the explicit contributions are considered

$$\rho_k^n \frac{U_{k,i}^E}{\Delta t} = \rho_k^n \frac{U_{k,i}^n}{\Delta t} + \overbrace{U_{k,i}^n \frac{1}{\alpha_k^n} \frac{\partial}{\partial x_j} (\alpha_k^n \rho_k^n U_{k,j}^n)}^1 - \overbrace{\frac{1}{\alpha_k^n} \frac{\partial}{\partial x_j} (\alpha_k^n \rho_k^n U_{k,i}^n U_{k,j}^n)}^2 +$$

$$\frac{1}{\alpha_k^n} \frac{\partial}{\partial x_j} (\alpha_k^n \tau_{k,ij}^n + \Sigma_{k,ij}^{Re^n}) - \overbrace{\frac{\partial P^n}{\partial x_i}}^7 + \rho_k^n g_i + \overbrace{\sum_{p \neq k} J'_{(p \rightarrow k),i}^n}^8 + \overbrace{S_{k,i}^n}^9, \quad (2.89)$$

with

$$\begin{aligned} \frac{1}{\alpha_k^n} \frac{\partial}{\partial x_j} (\alpha_k^n \tau_{k,ij}^n + \Sigma_{k,ij}^{Re^n}) &= \frac{1}{\alpha_k^n} \frac{\partial}{\partial x_j} \left(\overbrace{\alpha_k^n (\mu_k^{t^n} + \mu_k)}^3 \frac{\partial U_{k,i}^n}{\partial x_j} + \overbrace{\alpha_k^n (\mu_k^{t^n} + \mu_k)}^4 \frac{\partial U_{k,j}^n}{\partial x_i} - \right. \\ &\left. \overbrace{\frac{2}{3} \delta_{ij} \alpha_k^n \rho_k^n q_k^{n^2}}^5 - \overbrace{\frac{2}{3} \delta_{ij} \alpha_k^n (\mu_k^{t^n} + \mu_k)}^6 \frac{\partial U_{k,m}^n}{\partial x_m} \right). \end{aligned} \quad (2.90)$$

Also we have

$$J'_{(p \rightarrow k),i}^n = \frac{1}{\alpha_k^n} I'_{(p \rightarrow k),i}^n, \quad (2.91)$$

with $S_k^n = S_k^n(\alpha_l, U_l^n, P^n)$, with $l = 1, \dots$, number of phases and $\rho_k^n = \rho_k(P^n, h_k^n)$ given by the thermodynamic table or analytic law.

The first term is so called explicit mass accumulation part

$$\frac{1}{(\alpha_k^n)^I} \frac{\partial}{\partial x_j} (\alpha_k^n \rho_k^n U_{k,j}^n) U_{k,i}^n \Omega_I = \frac{1}{(\alpha_k^n)^I} \sum_{J \in V_I} (\alpha_k^n)^{IJ} (\rho_k^n)^{IJ} (U_{k,m}^n)^{IJ} n_{IJ,m} (U_{k,i}^n)^I, \quad (2.92)$$

with $(\cdot)^I$ the values on the cell number I , $(\cdot)^{IJ}$ the values at the interface of the cells I and J , or on the boundary of the cell I , $n_{IJ,m}$ the m^{th} component of the surface vector (m^2), V_I the neighboring of the cell I and Ω_I the volume of the cell I . The main problem in this expression is the term $\frac{(\alpha_k^n)^{IJ}}{(\alpha_k^n)^I}$ which is not bounded. In order to bound this term one may set $(\alpha_k^n)^I > \alpha_{min}^c \rightarrow \frac{(\alpha_k^n)^{IJ}}{(\alpha_k^n)^I}$ with $(\alpha_k^n)^{IJ}$ equal to the interface fraction calculated by the conservative mass solver. It is also possible set $(\alpha_k^n)^I < \alpha_{min}^c$ and in this case, the interface fraction is re-calculated, using an harmonic mean

$$(\alpha_k^n)^{IJ} = \frac{2(\alpha_k^n)^I (\alpha_k^n)^J}{(\alpha_k^n)^I + (\alpha_k^n)^J}. \quad (2.93)$$

Then, the ratio is bounded $\frac{(\alpha_k^n)^{IJ}}{(\alpha_k^n)^I} = \frac{2(\alpha_k^n)^J}{(\alpha_k^n)^I + (\alpha_k^n)^J} < 2$. Finally we can simply limit α_{min}^c with a numerical parameter and the default value is 10^{-6} .

The second term is the explicit convective contribution

$$\frac{1}{(\alpha_k^n)^I} \frac{\partial}{\partial x_j} (\alpha_k^n \rho_k^n U_{k,i}^n U_{k,j}^n) \Omega_I = \frac{1}{(\alpha_k^n)^I} \sum_{J \in V_I} (\alpha_k^n)^{IJ} (\rho_k^n)^{IJ} (U_{k,i}^n)^{IJ} (U_{k,m}^n)^{IJ} n_{IJ,m}. \quad (2.94)$$

The ratio $\frac{(\alpha_k^n)^{IJ}}{(\alpha_k^n)^I}$ is determined as explained before.

The terms from 3 to 6 represent the diffusive contributions. The different parts are: the diagonal part of the deformation tensor (laminar and turbulent), the transposed-gradient contribution (laminar and turbulent), the turbulence gradient and the second viscosity contribution. The diagonal part of the deformation tensor (laminar and turbulent) is defined as

$$\frac{1}{(\alpha_k^n)^I} \frac{\partial}{\partial x_j} \left(\alpha_k^n (\mu_k) \frac{\partial U_{k,i}^n}{\partial x_j} \right) \Omega_I = \frac{1}{(\alpha_k^n)^I} \sum_{J \in V_I} (\alpha_k^n)^{IJ} (\mu_k)^{IJ} \frac{(U_{k,j}^n)^{IJ} - (U_{k,i}^n)^{IJ}}{IJ} (U_{k,i}^n)^{IJ} |n_{IJ}|. \quad (2.95)$$

The ratio $\frac{(\alpha_k^n)^{IJ}}{(\alpha_k^n)^I}$ is determined as explained before for the convective part, but the limit fraction used here, α_{min}^D , can be set to an other numerical value by the user. The default value remains equal to 10^{-6} . Expressions 4 to 6 are called weighted gradient contributions, such as the turbulence gradient,

$$-\frac{1}{\alpha_k} \frac{\partial}{\partial x_i} \left(\frac{2}{3} \alpha_k \rho_k q_k^2 \right). \quad (2.96)$$

They are treated using a weighted mean-square gradient method, which presents the advantage to avoid problems due to the residual phases ($\alpha_k \rightarrow 0$).

The last term represents the pressure gradient contribution. In single phase or dispersed phase zones, it is calculated as a simple finite volume gradient with mass weighted adaptation

$$\left(\frac{\partial P}{\partial x_i} \right)^I \Omega_I = \sum_{J \in V_I} P^{IJ} n_{IJ,i}, \quad (2.97)$$

with P^{IJ} the pressure calculated at the boundary of the cells, using

$$\left(\frac{1}{M^I} + \frac{1}{M^J} \right) P^{IJ} = \frac{P^I}{M^I} + \frac{P^J}{M^J} \quad M = \sum_k \alpha_k \rho_k. \quad (2.98)$$

In order to take into account the non uniformity of the pressure gradient in cells where one detects a perfect phase separation, a different contribution for each present phase is applied. The weight is taken consistent with the assumption of gravity equilibrium

$$\frac{\partial}{\partial t} \alpha_k \rho_k U_{k,i} + \dots = \dots - \alpha_k \overbrace{\frac{\rho_k}{\sum_{p=1}^{nphas} \alpha_p \rho_p} \frac{\partial P}{\partial x_i}}^7 + \alpha_k \rho_k g_i + \dots \quad (2.99)$$

Implicit balance $U_{k,i}^n \rightarrow U_{k,i}^{n+1}$. Making the difference between equations (2.88 and

2.89), the implicit part of the balance is

$$\begin{aligned} \rho_k^n \frac{\delta U_{k,i}}{\Delta t} + \text{conv}(\delta U_{k,i}) - \text{diff}(\delta U_{k,i}) - \sum_{p \neq k} \frac{\partial J'_{p \rightarrow k,i}}{\partial U_{l,i}} \delta U_{l,i} - \frac{\partial S_{k,i}}{\partial U_{l,i}} \delta U_{l,i} = \\ - \frac{\partial \delta P}{\partial x_i} + \rho_k^n \frac{\delta U_{k,i}^E}{\Delta t} - \frac{1}{\alpha_k^n} \frac{\partial}{\partial x_i} \rho_k^n D_{\alpha_k} \delta \alpha_k, \quad (2.100) \end{aligned}$$

with $\delta U_k = U_k^{n+1} - U_k^n$, $\delta U_k^E = U_k^E - U_k^n$, and $\delta P = P^{n+1} - P^n$.

The convective and diffusive operators conv and diff are linear, positive and defined as follow

- $\text{conv}(\cdot) = \frac{1}{\alpha_k^n} \left[\text{div} \left[\alpha_k^n \rho_k^n \vec{U}_k^n(\cdot) \right] - (\cdot) \text{div} \alpha_k^n \rho_k^n \vec{U}_k^n \right]$,
- $\text{diff}(\cdot) = \frac{1}{\alpha_k^n} \text{div} \left[\alpha_k^n (\mu_k + \mu_k^t) \nabla(\cdot) \right]$.

The dispersive contribution form $\frac{1}{\alpha_k^n} \frac{\partial}{\partial x_i} \rho_k^n D_{\alpha_k} \delta \alpha_k$ can be obtained after decomposition of the weighted gradient-like contributions contained in momentum closure-laws expression, such as the gradient of turbulence, the drift contribution or the turbulent added-mass term. For instance, if we only retain the gradient of turbulence, the dispersive coefficient will remain equal to $D_{\alpha_k} = \frac{2}{3} q_k^2$.

Prediction velocity step $U_{k,i}^n \rightarrow U_{k,i}^{pr}$. In this sub-step, we solve the momentum equation, neglecting the volumetric fractions and pressure variations : $\delta \alpha_k \rightarrow 0$ and $\delta P \rightarrow 0$.

$$\rho_k^n \frac{\delta U_{k,i}^{pr}}{\Delta t} + \text{conv}(\delta U_{k,i}^{pr}) - \text{diff}(\delta U_{k,i}^{pr}) - \sum_{p \neq k} \frac{J'_{(p \rightarrow k),i}}{\partial U_{l,i}} \delta U_{l,i}^{pr} - \frac{\partial S_{k,i}}{\partial U_{l,i}} \delta U_{l,i}^{pr} = \rho_k^n \frac{\delta U_{k,i}^E}{\Delta t}, \quad (2.101)$$

with $\delta U_k^{pr} = U_k^{pr} - U_k^n$.

This system of equations cannot be solved easily since phases are strongly coupled by the implicit nature of the momentum source terms, interface ones $J'_{(p \rightarrow k)}$ and external ones S_k . The linearization of these contributions, with respect to the definition of drag and added-mass terms lead to the following expression

$$\begin{aligned} \rho_k^n \frac{\delta U_{k,i}^{pr}}{\Delta t} + [\text{conv} + \text{diff}](\delta U_{k,i}^{pr}) - \\ \sum_{p \neq k} \alpha_p F_D^{pk} [\delta U_{p,i}^{pr} - \delta U_{k,i}^{pr}] - \sum_{p \neq k} \frac{\alpha_p C_A^{pk}}{\Delta t} [\delta U_{p,i}^{pr} - \delta U_{k,i}^{pr}] - \sum_l \frac{\partial S_{k,i}}{\partial U_{l,i}} \delta U_{l,i}^{pr} = \rho_k^n \frac{\delta U_{k,i}^E}{\Delta t}. \quad (2.102) \end{aligned}$$

There is only one condition to obtain an invertible system. The external source-term

derivatives must verify

$$\frac{\partial S_{k,i}}{\partial U_{k,i}} < 0 \text{ and } \frac{\partial S_{k,i}}{\partial U_{l,i}} > 0, \text{ for } l \neq k. \quad (2.103)$$

The system is then split in two sub-steps, which guarantee the conservative property of the interface transfer terms

convection-diffusion sub-step $U_{k,i}^n \rightarrow U_{k,i}^{pr1}$, solved by a Jacobi process

$$\rho_k^n \frac{\delta U_{k,i}^{pr1}}{\Delta t} + [\text{conv+diff}](\delta U_{k,i}^{pr1}) + \sum_{p \neq k} \left(\alpha_p F_D^{pk} + \frac{\alpha_p C_A^{pk}}{\Delta t} \right) \delta U_{k,i}^{pr1} - \frac{\partial S_{k,i}}{\partial U_{k,i}} \delta U_{k,i}^{pr1} = \rho_k^n \frac{\delta U_{k,i}^E}{\Delta t}. \quad (2.104)$$

source-term reactualisation sub-step $U_{k,i}^{pr1} \rightarrow U_{k,i}^{pr}$

$$\begin{aligned} \rho_k^n \frac{\delta U_{k,i}^{pr}}{\Delta t} - \sum_{p \neq k} \alpha_p F_D^{pk} [\delta U_{p,i}^{pr} - \delta U_{k,i}^{pr}] - \sum_{p \neq k} \frac{\alpha_p C_A^{pk}}{\Delta t} [\delta U_{p,i}^{pr} - \delta U_{k,i}^{pr}] - \sum_l \frac{\partial S_{k,i}}{\partial U_{l,i}} \delta U_{l,i}^{pr} = \\ \rho_k^n \frac{\delta U_{k,i}^{pr1}}{\Delta t} + \sum_{p \neq k} \left(\alpha_p F_D^{pk} + \frac{\alpha_p C_A^{pk}}{\Delta t} \right) \delta U_{k,i}^{pr1} - \frac{\partial S_{k,i}}{\partial U_{k,i}} \delta U_{k,i}^{pr1}. \end{aligned} \quad (2.105)$$

This last system is local (for each cell and each i-space direction) and can be written using matrix formalism

$$[M_i^V] \begin{bmatrix} \delta U_{1,i}^{pr} \\ \vdots \\ \delta U_{nphas,i}^{pr} \end{bmatrix} = [M_i^V]^{diag} \begin{bmatrix} \delta U_{1,i}^{pr1} \\ \vdots \\ \delta U_{nphas,i}^{pr1} \end{bmatrix} \quad (2.106)$$

$[M_i^V]$ is a $nphas * nphas$ positive definite matrix, called the velocity coupling matrix in the i_{th} direction. Its inversion is made either by a direct method (for $nphas \leq 5$) or by a conjugated gradient method. $[M_i^V]^{diag}$ is the diagonal part of the matrix. The general form of the coefficient is

$$[M_i^V]_{(k,p)} = -\frac{\alpha_p F_D^{pk} \Delta t}{\rho_k^n} - \frac{\alpha_p C_A^{pk}}{\rho_k^n} + \frac{\Delta t}{\rho_k} \frac{\partial S_{k,i}}{\partial U_{p,i}}, \text{ for } p \neq k, \quad (2.107)$$

$$[M_i^V]_{(k,k)} = 1 + \sum_{p \neq k} \frac{\alpha_p F_D^{pk} \Delta t}{\rho_k^n} + \sum_{p \neq k} \frac{\alpha_p C_A^{pk}}{\rho_k^n} - \frac{\Delta t}{\rho_k} \frac{\partial S_{k,i}}{\partial U_{k,i}}. \quad (2.108)$$

Final velocity $U_{k,i}^{pr} \rightarrow U_{k,i}^{n+1}$. Making the difference between equations 2.88 and 2.101 and using 2.89 and neglecting the convective and diffusive increment contribution, one

can obtain the final velocity, for each i -space direction. In this step, final velocity $U_{k,i}^{n+1}$ is solution of a linear system, introducing the pressure and fraction increments

$$\begin{aligned} \begin{bmatrix} U_{1,i}^{n+1} \\ \vdots \\ U_{nphas,i}^{n+1} \end{bmatrix} &= \begin{bmatrix} U_{1,i}^{pr} \\ \vdots \\ U_{nphas,i}^{pr} \end{bmatrix} \\ &- [M_i^V]^{-1} \begin{bmatrix} \frac{\Delta t}{\rho_1^n} \frac{\partial}{\partial x_i} (\delta P) \\ \vdots \\ \frac{\Delta t}{\rho_{nphas}^n} \frac{\partial}{\partial x_i} (\delta P) \end{bmatrix} - [M_i^V]^{-1} \begin{bmatrix} \frac{\Delta t}{\alpha_1 \rho_1^n} \frac{\partial}{\partial x_i} (\rho_1 D_{\alpha_1} \delta \alpha_1) \\ \vdots \\ \frac{\Delta t}{\alpha_{nphas} \rho_{nphas}^n} \frac{\partial}{\partial x_i} (\rho_{nphas} D_{\alpha_{nphas}} \delta \alpha_{nphas}) \end{bmatrix} \end{aligned} \quad (2.109)$$

with $\delta P = P^{n+1} - P^n$, $\delta \alpha_k = \alpha_k^{n+1} - \alpha_k^n$ and $[M_i^V]^{-1}$ the inverse of the velocity coupling matrix.

The pressure-gradient correction represents the basis of the elliptic scheme, so the exact formulation has to be kept. The fraction-gradient correction is not essential, but can introduce some numerical diffusion (i.e. numerical stabilization) in the mass balance equation. Nevertheless, the diagonal and isotropic contribution is only kept (that is to say the diffusion contribution of the fraction in the equation), the local spatial variation of the D_{α_k} coefficients are neglected. These remarks lead to the simple formulation

$$U_{k,i}^{n+1} = U_{k,i}^{pr} - C_{k,i}^P \frac{\partial \delta P}{\partial x_i} - C_k^\alpha \frac{1}{\alpha_k \rho_k} \frac{\partial \delta \alpha_k}{\partial x_i}, \quad (2.110)$$

with $C_{k,i}^P$ and C_k^α two positive parameters defined as

$$C_{k,i}^P = \sum_{l=1}^{nphas} [M_i^V]_{(k,l)}^{-1} \frac{\Delta t}{\rho_l^n}, \quad (2.111)$$

$$C_k^\alpha = [M_i^V]_{(k,k)}^{-1} \Delta t D_{\alpha_k}. \quad (2.112)$$

2.2.2 Mass-Energy equations: the Alpha-Pressure-Energy cycle

The next fractional step solves a coupled-system of mass and total enthalpy, in order to ensure a perfect conservation of these quantities. The algorithm is called the *Alpha-Pressure-Energy cycle* since the final main variables are α_k^{n+1} , P^{n+1} , H_k^{n+1} and U_k^{n+1} .

Full implicit non-linear system

The mass-energy system in its implicit form

$$\sum_{k=1}^{nphas} \alpha_k^{n+1} = 1, \quad (2.113)$$

$$\frac{\alpha_k^{n+1} \rho_k^{n+1} - \alpha_k^n \rho_k^n}{\Delta t} + \frac{\partial}{\partial x_i} (\alpha_k^{n+1} \rho_k^n U_{k,i}^{n+1}) = \Gamma_k^{n+1}, \quad (2.114)$$

$$\begin{aligned} \rho_k^n \frac{H_k^{n+1} - H_k^n}{\Delta t} + \frac{1}{\alpha_k^n} \left[\frac{\partial}{\partial x_i} (\alpha_k^n \rho_k^n U_{k,i}^{n+1} H_k^{n+1}) - H_k^{n+1} \frac{\partial}{\partial x_i} (\alpha_k^n \rho_k^n U_{k,i}^{n+1}) \right] = \\ \frac{1}{\alpha_k^n} \frac{\partial}{\partial x_i} \left(\alpha_k^n \lambda_k \frac{\partial T_k^{n+1}}{\partial x_i} \right) + \left(\frac{f_{\alpha_k}(\alpha_k^n)}{\alpha_k^n} \right) \varphi_k^n + \\ \frac{P^{n+1} - P^n}{\Delta t} + \sum_{p \neq k} \frac{\Pi_{(p \rightarrow k)}^{n+1}}{\alpha_k^n} + \frac{\Gamma_k^{n+1} (H_k^\sigma - H_k^{n+1})}{\alpha_k^n}, \quad (2.115) \end{aligned}$$

with $\rho_k^{n+1} = \rho_k(P^{n+1}, h^{n+1})$, calculated from external tables or analytic user laws, $\Gamma_k^{n+1} = \Gamma_k(\alpha_l^n, h_l^{n+1}, P^{n+1})$, $h_l^{n+1} = H_l^{n+1} - \frac{1}{2}(U_{l,i}^{n+1})^2$, $T_k^{n+1} = T_k(P^n, h_k^n) + \frac{1}{C_{p_k}}(H_k^{n+1} - H_k^n)$, $f_{\alpha_k}(\alpha_k^n)$ given by formula 2.69, $\Pi_{p \rightarrow k}^{n+1} = \Pi'_{p \rightarrow k}(\alpha_l^n, h_l^{n+1}, P^{n+1})$, $H_k^\sigma = H_k^{n+1}$, h^{sat} or given by a user routine, $U_{k,i}^{n+1}$ updated from $U_{k,i}^{Pr}$ and α_k^{n+1} .

The system is now solved using sub-cycles, each containing sub-steps solving sequentially, total enthalpies, volumetric fractions and pressure. Density and velocities are actualized at the end of each sub-cycle. Before starting the cycles, the variables must be initialized (see Table 2.1).

Initialization
$\alpha_k^{[0]} = \alpha_k^n$
$H_k^{[0]} = H_k^n$
$P^{[0]} = P^n$
$\rho_k^{[0]} = \rho_k^n$
$U_{k,i}^{[0]} = U_{k,i}^{Pr}$

Table 2.1: Variable initialization

Enthalpy j^{th} sub-step $H_k^n \rightarrow H_k^{[j]}$

In order to get a simpler formulation, the enthalpy jump and local enthalpy are supposed to be equal, i.e. $H_k^\sigma = H_k$. The full balance is obtained after decomposition in

fractional steps: the explicit balance, the source- coupling balance, the implicit balance, and the extra-diagonal source-coupling actualization.

j^{th} **Enthalpy explicit balance** $H_k^n \rightarrow H_k^{[j,E]}$

This equation is solved for each phase

$$\begin{aligned} \rho_k^n \frac{H_k^{[j,E]} - H_k^n}{\Delta t} + \overbrace{\frac{1}{\alpha_k^n} \left[\frac{\partial}{\partial x_i} \left(\alpha_k^n \rho_k^n U_{k,i}^{[j-1]} H_k^n \right) - H_k^n \frac{\partial}{\partial x_i} \left(\alpha_k^n \rho_k^n U_{k,i}^{[j-1]} \right) \right]}^1 = \\ \underbrace{\frac{1}{\alpha_k^n} \frac{\partial}{\partial x_i} \left(\alpha_k^n \lambda_k \frac{\partial T_k^n}{\partial x_i} \right)}_2 + \underbrace{\left(\frac{f_{\alpha_k}(\alpha_k^n)}{\alpha_k^n} \right) \varphi_k^n}_3 + \underbrace{\frac{P^{[j-1]} - P^n}{\Delta t}}_4 + \underbrace{\frac{1}{\alpha_k^n} \sum_{p \neq k} \Pi'_{(p \rightarrow k)}^n}_5. \end{aligned} \quad (2.116)$$

The *first term* represents the sum of explicit convection and mass accumulation part. The handling makes appear unbounded terms $\frac{(\alpha_k^n)^{IJ}}{(\alpha_k^n)^I}$. The solution is once again to adapt the value of face fractions, choosing either geometric or harmonic interpolation for $(\alpha_k^n)^{IJ}$. The *second term* represents the diffusive thermal contribution. For practical reasons, it is evaluated as

$$\frac{1}{\alpha_k^n} \frac{\partial}{\partial x_i} \left(\alpha_k^n \beta_k \frac{\partial H_k^n}{\partial x_i} \right), \quad \beta_k = \frac{\lambda_k}{C p_k} + \frac{\mu_t}{\sigma_s}, \quad \text{accounting for turbulent diffusion.} \quad (2.117)$$

The *third term* represents the wall heating diffusive contribution. The weighting by f_{α_k} function is only available for phases 1 and 2, in water-steam regime. The *term 4* represents the temporal variation of pressure that remains explicit. The *term 5* represents the source contributions, that can be decomposed into user defined sources and water-steam model sources (see 2.1.3)

$$\sum_{p \neq k} \Pi'_{(p \rightarrow k)}^n = \sum_{p \neq k} \underbrace{\zeta_{pk} (T_p^n - T_k^n)}_{\text{user defined}} + \underbrace{\psi_0^{[j-1]} \Pi_k'^{w/s}}_{\text{water or steam, i.e., } k=1,2}. \quad (2.118)$$

The explicit part of $\Pi_k'^{w/s}$ is kept, with regard to the enthalpy, and a linear development in terms of the pressure increment is used

$$\Pi_k'^{w/s} = \Pi_k'^{w/s} (P^n, h_k^n \text{ or } T_k^n) + \left(\frac{\partial \Pi_k'^{w/s}}{\partial P} \right)^n (P^{[j-1]} - P^n). \quad (2.119)$$

Moreover, division by volumetric fraction is controlled in order to avoid residual phase problems

$$\frac{1}{\alpha_k^n} \Pi'_{(p \rightarrow k)}^n \rightarrow \frac{1}{\alpha_k^*} \Pi'_{(p \rightarrow k)}^n \quad \text{with } \alpha_k^* = \max(\alpha_k^n, 1.e^{-10}). \quad (2.120)$$

Finally, non-dimensional coefficient $\psi_0^{[j-1]}$ value is close to one. It is solution of the mass source step and ensures the exact conservation of the mass-energy system.

j^{th} **Enthalpy source-coupling balance** $H_k^n \rightarrow H_k^{[j,C]}$. Neglecting convective and diffusive increment contributions, the system can be set in a linear and conservative form involving source, written as follows

$$\rho_k^n \frac{H_k^{[j,C]} - H_k^{[j,E]}}{\Delta t} = \sum_{p \neq k} \frac{\zeta_{pk}}{\alpha_k^*} \left(\frac{H_p^{[j,C]} - H_p^n}{Cp_p} - \frac{H_k^{[j,C]} - H_k^n}{Cp_k} \right) + \frac{\psi_0^{[j-1]}}{\alpha_k^*} \left(\frac{\partial \Pi_k'^{w/s}}{\partial H_k} \right)^n (H_k^{[j,C]} - H_k^n). \quad (2.121)$$

Making sure that the derivative of water-steam sources terms are negative,

$$\left(\frac{\partial \Pi_k'^{w/s}}{\partial H_k} \right) \leq 0. \quad (2.122)$$

The system can be written, using a matrix formalism

$$[M^H] \begin{bmatrix} \delta H_1^{[j,C]} \\ \vdots \\ \delta H_{nphas}^{[j,C]} \end{bmatrix} = \begin{bmatrix} \delta H_1^{[j,E]} \\ \vdots \\ \delta H_{nphas}^{[j,E]} \end{bmatrix} \text{ with } \delta H_k^{[j,C]} = H_k^{[j,C]} - H_k^n \text{ and } \delta H_k^{[j,E]} = H_k^{[j,E]} - H_k^n. \quad (2.123)$$

$[M^H]$ is a $nphas * nphas$ positive definite matrix, called the enthalpy coupling matrix. Its inversion is made either by a direct method (for $nphas \leq 5$) or by a conjugated gradient method. The general form of the coefficient is

$$[M^H]_{(k,p)} = -\zeta_{pk} \frac{\Delta t}{\alpha_k^* \rho_k^n Cp_p} \text{ for } p \neq k, \quad (2.124)$$

$$[M^H]_{(k,k)} = 1 + \left(\sum_{p \neq k} \zeta_{pk} \right) \frac{\Delta t}{\alpha_k^* \rho_k^n Cp_k} - \left(\frac{\partial \Pi_k'^{w/s}}{\partial H_k} \right)^n \frac{\psi_0^{[j-1]} \Delta t}{\alpha_k^* \rho_k^n}. \quad (2.125)$$

j^{th} **Enthalpy implicit balance** $H_k^n \rightarrow H_k^{[j,I]}$. The following step accounts for implicit contributions of convection and diffusion, and is obtained by making the difference between 2.115 and 2.121 and using 2.116. Diagonal part of source coupling is kept

$$\frac{\rho_k^n [M^H]_{(k,k)}}{\Delta t} \delta H_k^{[j,I]} + \frac{1}{\alpha_k^n} \left[\frac{\partial}{\partial x_i} \left(\alpha_k^n \rho_k^n U_{k,i}^{[j-1]} \delta H_k^{[j,I]} \right) - \delta H_k^{[j,I]} \frac{\partial}{\partial x_i} \left(\alpha_k^n \rho_k^n U_{k,i}^{[j-1]} \right) \right] - \frac{1}{\alpha_k^n} \frac{\partial}{\partial x_i} \left(\alpha_k^n \beta_k \frac{\delta H_k^{[j,I]}}{\partial x_i} \right) = \frac{\rho_k^n [M^H]_{(k,k)}}{\Delta t} \delta H_k^{[j,C]}, \quad (2.126)$$

with $\delta H_k^{[j,I]} = H_k^{[j,I]} - H_k^n$.

Extra-diagonal source-coupling actualization $H_k^n \rightarrow H_k^{[j]}$. The last step is obtained by making the difference between 2.115 and 2.126, and neglecting convective and diffusive double increment contributions. Then the linear system is solved for each cell

$$[M^H] \begin{bmatrix} H_1^{[j]} - H_1^{[j,I]} \\ \vdots \\ H_{nphas}^{[j]} - H_{nphas}^{[j,I]} \end{bmatrix} = [M^H]^{ext} \begin{bmatrix} H_1^{[j,C]} - H_1^{[j,I]} \\ \vdots \\ H_{nphas}^{[j,C]} - H_{nphas}^{[j,I]} \end{bmatrix} \quad (2.127)$$

with $[M^H]^{ext}$ the extra-diagonal part of the coupling matrix.

One can remark that in the simple case of a two-phase steam-water flow, the coupling matrix is diagonal, so the re-actualization reduces for each phase to $H_k^{[j]} = H_k^{[j,I]}$.

Mass j^{th} sub-step $\alpha_k^n \rightarrow \alpha_k^{[j]}$. The mass balance equations are solved in terms of volumetric fractions. The full balance is obtained after decomposition in two fractional steps: the mass source-coupling balance and the convection balance.

j^{th} mass source-coupling balance $\alpha_k^n \rightarrow \alpha_k^{[j,C]}$. Mass transfer terms have 3 possible contributions: $\Gamma_k = \Gamma_k^{w/s} + \Gamma_{(w \rightarrow k)}^{nuc} + \sum_{p \neq k} \Gamma_{(p \rightarrow k)}^{us}$.

The first term is the mass transfer that, in the water-steam bulk model, is deduced from energy transfer

$$\Gamma_1^{w/s} = -\Gamma_2^{w/s} = \frac{\Pi_1^{w/s} + \Pi_2^{w/s}}{H_2^\sigma - H_1^\sigma}, \quad \Gamma_k^{w/s} = 0 \text{ for } k \geq 3, \quad (2.128)$$

with $\Pi_k^{w/s} = \Pi_k^{w/s}(P^n, h_k^n, \text{ or } T_k^n) + \left(\frac{\partial \Pi_k^{w/s}}{\partial P}\right)^n (P^{[j-1]} - P^n) + \left(\frac{\partial \Pi_k^{w/s}}{\partial H_k}\right)^n (H_k^{[j]} - H_k^n)$.

The second term is the nucleate boiling at heated wall

$$\Gamma_w^{nuc} = \Gamma_{(w \rightarrow 2)}^{nuc} = -\Gamma_{(w \rightarrow 1)}^{nuc} \geq 0, \quad \Gamma_{(w \rightarrow K)}^{nuc} = 0 \text{ for } k \geq 3, \quad (2.129)$$

with $\Gamma_w^{nuc} = \Gamma_w^{nuc}(P^n, T_1^n, \dots) + \left(\frac{\partial \Gamma_w^{nuc}}{\partial P}\right)^n (P^{[j-1]} - P^n)$.

The third term is the user-define transfer term

$$\Gamma_k^{us} = \sum_{p \neq k} \Gamma_{(p \rightarrow k)}^{us}. \quad (2.130)$$

To ensure the positivity of all the volumetric fractions, the sub-step must includes a

numerical treatment, introducing weighted coefficients

$$\frac{\rho_k^{[j-1]} \alpha_k^{[j,C]} - \rho_k^n \alpha_k^n}{\Delta t} = \psi_0^{[j]} \Gamma_k^{w/s} + \psi_1^{[j]} \Gamma_{(w \rightarrow k)}^{nuc} + \sum_{p \neq k} \psi_{pk}^{[j]} \Gamma_{(p \rightarrow k)}^{us}, \quad (2.131)$$

with

$$\psi_0^{[j]} = \frac{\alpha_1^{[j,C]}}{\alpha_1^*} \text{ if } \Gamma_1^{w/s} \leq 0, \quad \psi_0^{[j]} = \frac{\alpha_2^{[j,C]}}{\alpha_2^*} \text{ else} \quad (2.132)$$

$$\psi_1^{[j]} = \frac{\alpha_1^{[j,C]}}{\alpha_1^*}, \quad (2.133)$$

$$\psi_{pk}^{[j]} = \frac{\alpha_k^{[j,C]}}{\alpha_k^*} \text{ if } \Gamma_{p \rightarrow k}^{us} \leq 0, \quad \psi_{pk}^{[j]} = \frac{\alpha_p^{[j,C]}}{\alpha_p^*} \text{ else, } (\psi_{pk}^{[j]} = \psi_{kp}^{[j]}), \quad (2.134)$$

and the definition $\alpha_k^* = \max(\alpha_k^n, 1e^{-10})$.

j^{th} **mass convection balance** $\alpha_k^n \rightarrow \alpha_k^{[j]}$. Making the difference between equations 2.114 and 2.131 and neglecting transfer terms increments and density increments, the mass convection balance is written

$$\rho_k^{[j-1]} \frac{\alpha_k^{[j]} - \alpha_k^{[j,C]}}{\Delta t} + \frac{\partial}{\partial x_i} (\alpha_k^{[j]} \rho_k^n U_{k,i}^{n+1}) = 0. \quad (2.135)$$

Using re-actualization formula 2.110 of the velocity, the convection-diffusion equation obtained is the following

$$\rho_k^{[j-1]} \frac{\alpha_k^{[j]} - \alpha_k^{[j,C]}}{\Delta t} + \frac{\partial}{\partial x_i} \left(\alpha_k^{[j]} \rho_k^n \left[U_{k,i}^{pr} - C_{k,i}^P \frac{\partial}{\partial x_i} (P^{[j-1]} - P^n) \right] \right) - \frac{\partial}{\partial x_i} \left(C_k^\alpha \frac{\partial \alpha_k^{[j]} - \alpha_k^n}{\partial x_i} \right) = 0. \quad (2.136)$$

In the end, all the fractions are positive but they don't ensure the volume conservation defined in (2.113).

2.2.3 Volume conservation and pressure projection

The pressure step is the basis of the elliptic solver. It can be obtained, first, by making the combination between mass-equations (2.114 -(2.131+ 2.136))

$$\underbrace{\frac{\alpha_k^{n+1} \rho_k^{n+1} - \alpha_k^{[j]} \rho_k^{[j-1]}}{\Delta t}}_1 - \underbrace{\frac{\partial}{\partial x_i} \left(\alpha_k^{[j]} \rho_k^n C_{k,i}^P \frac{\partial}{\partial x_i} (P^{n+1} - P^{[j-1]}) \right)}_2$$

$$\underbrace{\frac{\partial}{\partial x_i} \left(C_k^\alpha \frac{\partial \alpha_k^{n+1} - \alpha_k^{[j]}}{\partial x_i} \right)}_3 = \underbrace{\Gamma_k(\alpha_l^{n+1}, P^{n+1}, \dots) - \Gamma_k(\alpha_l^{[j]}, P^{[j-1]}, \dots)}_4. \quad (2.137)$$

Then, each contribution in terms of the pressure increment is linearized.

The first term represents the unsteady part. The linearization leads to

$$\frac{\alpha_k^{[j]}}{\Delta t} \left[\frac{\partial \rho_k}{\partial P} \Big|_h (P^{n+1} - P^{[j-1]}) + \frac{\partial \rho_k}{\partial h} \Big|_P (h^{n+1} - h^{[j-1]}) \right] + \frac{\rho_k^{[j-1]}}{\Delta t} [\alpha_k^{n+1} - \alpha_k^{[j]}]. \quad (2.138)$$

The enthalpy increment is supposed proportional to the pressure increment; one can derive a simplified equation from 2.115 that only takes into account the pressure variation and energy source terms increments development (see 2.121)

$$[M^H]_{k,k} (h^{n+1} - h^{[j-1]}) = \left[1 + \Delta t \frac{\partial}{\partial P} \sum_{p \neq k} \Pi_{(p \rightarrow k)}^n \right] \frac{1}{\rho_k^n} (P^{n+1} - P^{[j-1]}). \quad (2.139)$$

One may remark that in a flow without any energy transfer term, the first part of the unsteady contribution remains classical, introducing the celerity c_k^2

$$\frac{\partial \rho_k}{\partial P} \Big|_h \delta P + \frac{\partial \rho_k}{\partial h} \Big|_P \delta h = \left(\frac{\partial \rho_k}{\partial P} \Big|_h + \frac{1}{\rho_k} \frac{\partial \rho_k}{\partial h} \Big|_P \right) \delta P = \frac{1}{c_k^2} \delta P. \quad (2.140)$$

In the general case, a modified celerity c_k^{*2} is used, solution of equations 2.139 and 2.140. The first term becomes

$$\frac{\alpha_k^{[j]}}{c_k^{*2} \Delta t} (P^{n+1} - P^{[j-1]}) + \frac{\rho_k^{[j-1]}}{\Delta t} [\alpha_k^{n+1} - \alpha_k^{[j]}]. \quad (2.141)$$

The second term represents the diffusive (called elliptic) contribution. *The third term* is ignored in the sub-step. *The fourth term* represents the mass transfer increment. Only pressure increment of water-steam and nucleate boiling contributions are considered (see 2.131), and that leads to the simple expression

$$\left(\frac{\partial \Gamma_K^*}{\partial P} \right) (P^{n+1} - P^{[j-1]}) \text{ with } \frac{\partial \Gamma_K^*}{\partial P} = \psi_0^{[j]} \frac{\partial \Gamma_K^{w/s}}{\partial P} + \psi_1^{[j]} \frac{\partial \Gamma_{(w \rightarrow k)}^{nuc}}{\partial P}. \quad (2.142)$$

Pressure equation $P^{[j-1]} \rightarrow P^{[j]}$. The pressure equation applies to the increment $\delta P^{[j]} = P^{[j]} - P^{[j-1]}$. It is obtained after combining the *nphas*-equations 2.137 so as to make appear the volume conservation criterion

$$\sum_{k=1}^{nphas} \left(\frac{\alpha_k^{[j]}}{\rho_k^{[j-1]} c_k^{*2}} - \frac{\Delta t}{\rho_k^{[j-1]}} \left(\frac{\partial \Gamma_k^*}{\partial P} \right) \right) \frac{\delta P^{[j]}}{\Delta t} - \sum_{k=1}^{nphas} \frac{1}{\rho_k^{[j-1]}} \frac{\partial}{\partial x_i} \left(\alpha_k^{[j]} \rho_k^n C_{k,i}^P \frac{\partial}{\partial x_i} \delta P^{[j]} \right) =$$

$$\frac{1}{\Delta t} \left(\sum_{k=1}^{nphas} \alpha_k^{[j]} - \underbrace{\sum_{k=1}^{nphas} \alpha_k^{n+1}}_{\text{equal to 1}} \right). \quad (2.143)$$

The *Alpha-Pressure-Energy* cycle stops after the mass conservation sub-step, when the volume conservation holds. It is possible to adapt the criterion parameter ϵ_{vol} , but this one remains very severe as it applies to a maximum value over the whole domain

$$\max_{I \in NCEL} \left(\left| 1 - \sum_k \alpha_k^{[j]}(I) \right| \right) < \epsilon_{vol}. \quad (2.144)$$

The standard value of ϵ_{vol} is 10^{-5} .

2.3 The NEPTUNE data, param file and user routines

2.3.1 NEPTUNE data structure of the code

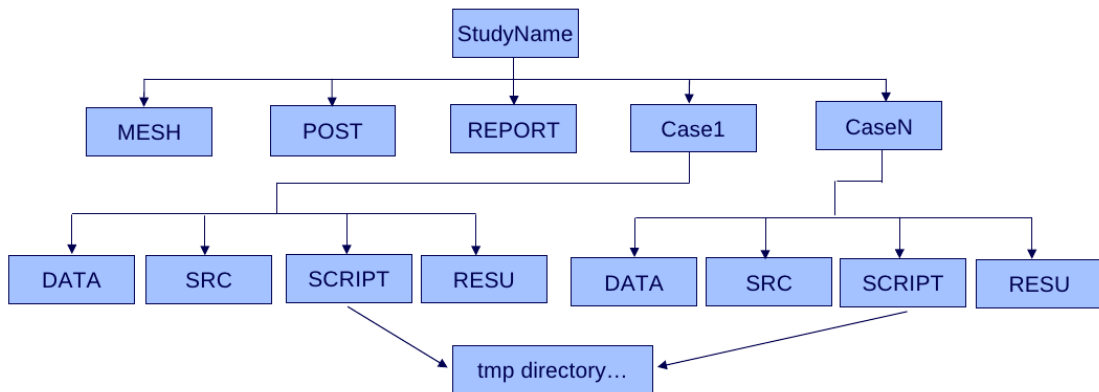


Figure 2.3: Tree structure of a case study

NEPTUNE requires a specific structure for the configuration and input files. Figure 2.3 shows this structure. Each simulation is denoted as *case*. It is possible to create a *studyName* directory where all the NEPTUNE simulations are performed. Inside this directory, each case will have its own directory (for example *case1*, *case2*) and there must be a *MESH* directory, where all the meshes are stored. Also, inside each case directory, four sub-directories are required to run the code. The utility `buildcase_nept` is used to build the tree structure of the study. The syntax of the command line is

```
$ buildcase_nept -study case1
```

This generates the correct directory structure as shown in Figure 2.3.



Figure 2.4: NEPTUNE GUI interface (Edamox).

When the study has been generated, new cases can be added by running the following command from the study base directory

```
$ buildcase_nept -case case1
```

During the execution, NEPTUNE will generate some temporary files that are by default stored in the `tmp_NEPTUNE` directory in the user directory. This directory must be periodically cleaned by hands, there is no automatic procedure.

The *MESH directory* contains the mesh(es) necessary for the study. The mesh formats accepted with the use of Enveloppe module are the I-DEAK Universal (extension `.unv`) and the MED 2.3 (extension `.med`). If Enveloppe is not used, only binary or ASCII Common Solver format is accepted.

The *POST directory* contains any post-processing programs.

The *REPORT directory* is intended to contain a spreadsheet or a report on the study.

The *SRC directory* contains a sub-directory **USERS** in which there are all the user Fortran routines necessary for the case, and it is possible to create other routines.

The *DATA directory* contains the data file `param` generated by the EDAMOX graphic user interface and also any file `suiamo` used for calculation restart.

The *RESU directory* contains the results of the NEPTUNE.CFD runs. To aid the traceability of the calculations, the files and directories placed in the directory RESU are given a suffix identifying the calculation start date and time by a ten-digit number (two digits each for year, month, day, hours, minutes). In the standard cases, RESU directory contains the files **suiava.*** for the calculation restart, **compil.log.*** giving a compilation report, **resume.*** giving information including machine type and code version, **listing*** reporting on the kernel run, **listenv.pre.*** reporting on the Enveloppe run during

pre-processing, **listenv.post.*** reporting on the Enveloppe run during post-processing, **param.***, copy of the settings file `param` used for the calculation and **runcase.***, copy of the launch script. Finally, the RESU directory contains the following directories: **CHR.ENSIGHT.*** containing the post-processing files in EnSight format (default option), **MED.*** containing the post-processing files in MED format (if requested by the user), **SRC.*** containing the user routines taken into account and **HIST.*** containing individual log files, These files record the monitoring over time, of certain certain variables at certain points defined by the user, called probes,

The *SCRIPT Directory* contains the calculation launch script (`runcase`).

Before running the case, it is necessary to copy the meshes to the directory MESH, to generate the settings file `param` using the EDAMOX interface and to adapt the User Fortran files necessary for the case. The next step is to open the directory SCRIPT and to launch the command file `runcase`. From this moment the NEPTUNE calculation starts and the temporary files of this simulation appears in the directory `tmp_NEPTUNE`. In this directory is possible to supervise the calculation through the file listing in which are reported the the main information of the run. At the end of the calculation, the results are copied to the directory RESU. It is also possible to change the temporary directory name and use, for example, a specific local disk name.

2.3.2 The NEPTUNE param file

Module	description
Special	enable special modules
Fluid&flow properties	Fluid properties
input-output control	input and output control
Generality	general physical settings
Numerical schemes	numerical schemes
Scalar	set scalar equations
Variable output control	output control
Run	run the code

Table 2.2: NEPTUNE modules

The `param` file is an input file create by the user to set the data for the simulations and it is contained in the DATA directory (see 2.3.1). There are two different ways to generate this dataset file. Using the NEPTUNE Edamox GUI or by editing the `param` file directly.

The `param` file consists of several sections. As shown in Figure 2.4 the NEPTUNE GUI opens a window which is divided into two main panels: the menu bar and the

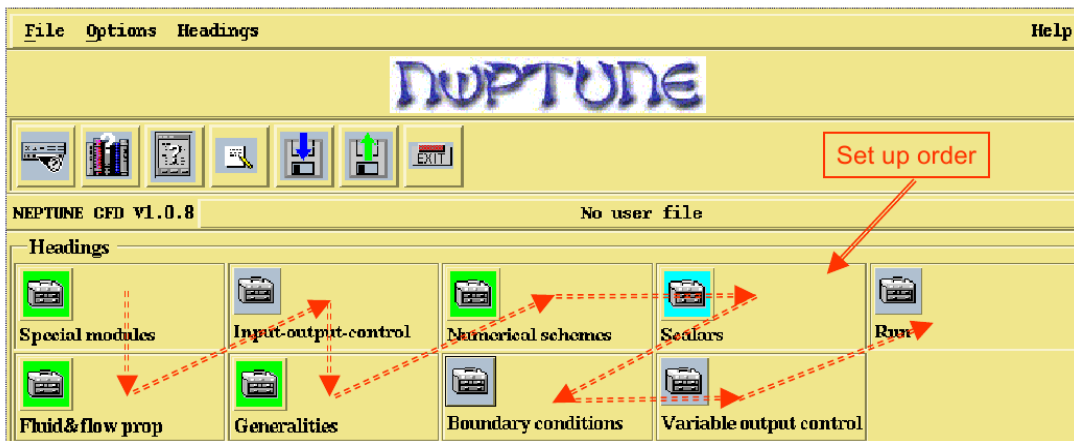


Figure 2.5: Suggested parameter order.

selection panel. The selection panel for the data structure is composed by 9 modules: Special modules, Fluid&flow properties, Input-output control, Generalities, Numerical schemes, Boundary conditions, Scalars, Variable output control and Run. In order to insert the parameters of the case it is preferable to follow the order shown in Figure 2.5.

In the menu *Options* it is possible to set the level of the users. There are three different level, User, Expert, Programmer. The standard level is the user level and it contains less parameters respect to the other levels; the expert and programmer levels provide access to a larger number of settings whose modification requires deeper knowledge of the numerical method. Now we illustrate briefly the NEPTUNE modules shown in Table 2.2.

The module *Special Modules* allows to enable special features of the two-phase flow. The options are: the option none for the separate phases, the option water/steam module and the option water/non-condensable module.

In the *Fluid&flow properties* module one can find the number of fluids and the fluid name options. All the physical properties and the turbulence models are defined in this module.

The *input-output control* module allows to set memory allocation, the mesh file, the time step and all input/output parameters.

The *Generality* module contains the general physical settings (gravity, pressure, etc) and controls the calling of many user routines. To compile these subroutines it is necessary to copy them from the USERS directory in the SRC directory.

The *numerical schemes* module contains the options that coupled the different equa-

tions and lead to the iterative solution of each system.

In the *Scalar* section one can set the scalars. In particular, there are two scalars that are enabled automatically when the water/steam module is selected in Special modules, the two total enthalpies for each phase, water and steam. Other scalars must be defined by specifying total number of scalars. The possible option that define a scalar equation are shown in Table 2.3.

routine	description
Convection	selection of the convection phase of the scalar
T-dep	time-dependent term in the scalar equation
Effective Diffusion	diffusion term in the scalar equation
Laminar Dynamic Coefficient	reference diffusion coefficient
Turbulent Schmidt	turbulent Schmidt number
Initialization Choice	scalar initialization choice
Type	passive scalar or total enthalpy
Initialization value and limit	

Table 2.3: Scalar equation options

In general, the *Boundary Conditions* module has several options to define Dirichlet or Neumann boundary conditions over the different boundary regions. For a complete explanation see Section 2.4.

In the *Variable output control* section the `chrono` buttons select the output of variables in the chronological post-processing files. The `listing` buttons enable the variables to be tracked in the listing (i.e. textual output). The `probes` number fields are used to track the values of variables at the probes. The values given for this case mean that results are wanted at all the probes.

The *run* module allows to run the code and save the results. Before running the code, it is necessary to save the `param` file. In the module Run it is possible to set the number of processors for a parallel run and to launch the code on line with the button `Run on line`. The NEPTUNE GUI generates a `param` file as

```
/Headings
/SPECIAL MODULES (1)
MODULE SPECIFIQUE = 1
/FLUID&FLOW prop (1)
NPHAS = 2
/GENERALITIES (2)
NOM FLUIDE = eau;vapeur
ETAT FLUIDE = 0;1
/THERMO (2)
MASSE VOLUMIQUE = 1000;1000
TEMPERATURE REFERENCE = 610;293.14
```

```

VISCOSITE DYN = 0.001;0.001
.....
/TURBULENCE (2)
ITURB =2;-1
CNUTLO =0;0
.....
/FLUID 1 (2)
UENT CONDL1 = 0;0;0;0;0
.....

```

This file can also be generated directly by editing the file. The file is subdivided in various sections with characteristic key words. The same keys on the NEPTUNE GUI interface.

2.3.3 User routines

routine	description
usini1.F	initialization from settings read from EDAMOX
usclim.F	boundary conditions at boundary faces
usphyv.F	calculation of physical properties
usiniv.F	definition of initial conditions
usdrag.F	drag coefficient calculation
ustsht.F	water and steam total enthalpy source
uslift.F	lift coefficient calculation
ustsns.F	generic momentum source terms
ustssp.F	passive scalar source terms
ustrmv.F	mass source terms (transfer or not)
usth12.F	source terms for energy transfer between two phases
usmaaj.F	added mass force
ushsig.F	interface enthalpy model
uskpdc.F	head losses zones
uspors.F	zones of porosity

Table 2.4: User routines

During the definition of the `param` file, it is possible to add user Fortran routines to specify laws, boundary conditions or property of the case study that are missing in the `param` file. These user routines are contained in the `USERS` folder within the `SRC` directory. When a user wants to modify a routine, it must to copy this routine in the directory `SRC`. The available user routines are the defined in Table 2.4.

2.4 A `param` file for standard boiling flow in a rectangular channel with constant bubbles diameter

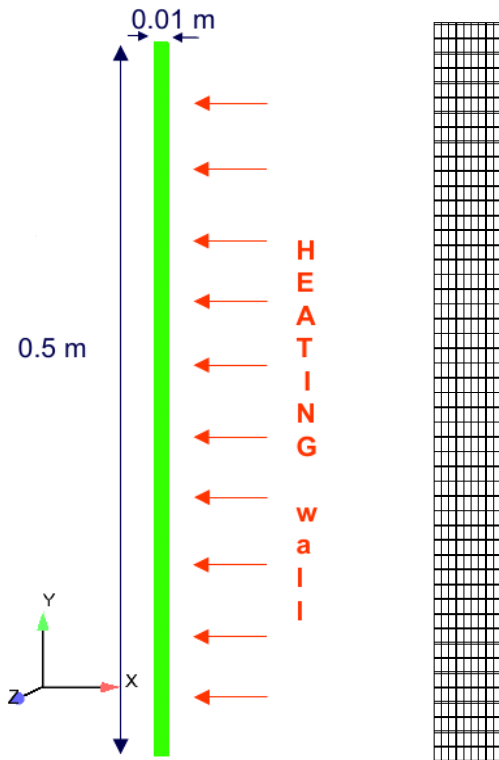


Figure 2.6: Geometry and mesh of the channel

In this section, an example of `param` file is presented step by step. The case analyzed is the standard boiling flow with constant bubble diameter. The geometry and the mesh chosen are shown in Figure 2.6. First, it is necessary to create the tree structure of the current case. Then, the mesh file `m1.unv` of the geometry is copied in the MESH folder and the Edamox GUI is opened by launching the command `./edam` from the DATA folder.

The `expert level` for this case is set in the menu Options, that provide access to a larger number of numerical settings.

In order to activate the two phase option of the code, the *Water/steam* module in the Special Modules panel is defined.

The `fluid and flow properties` panel is opened to setting the number of fluids involved in the simulation, the flow properties, the turbulence models, the wall

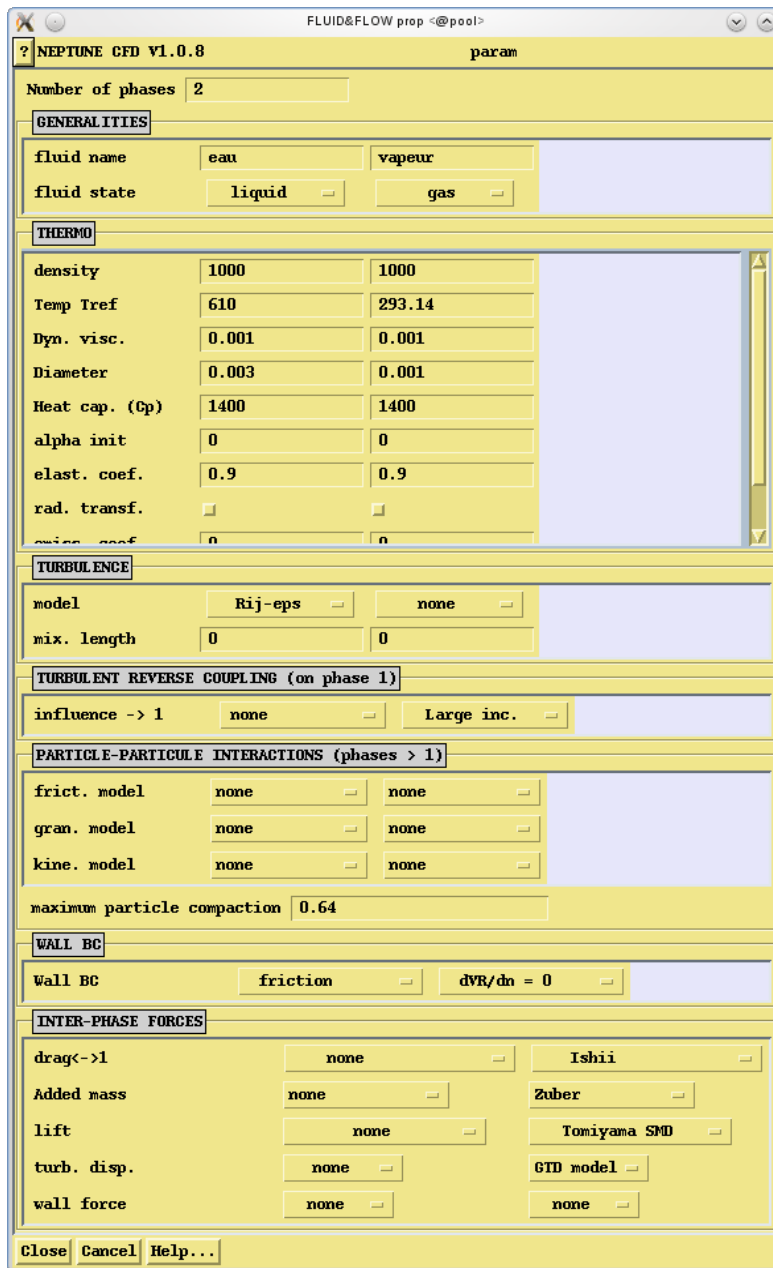


Figure 2.7: Fluid and Flow Properties panel

boundary conditions and the inter-phase forces. Figure 2.7 shows the fluid and flow properties panel. For this simulation, two phases, water and steam, are defined. The turbulent model chosen for the liquid phase is the *Rij-epsilon turbulence* model. No turbulence model is set for the vapor phase. Friction wall boundary conditions are chosen for the liquid phase and zero flux on the relative velocity conditions for the vapor phase. The inter-phase forces are shown in Figure 2.8.

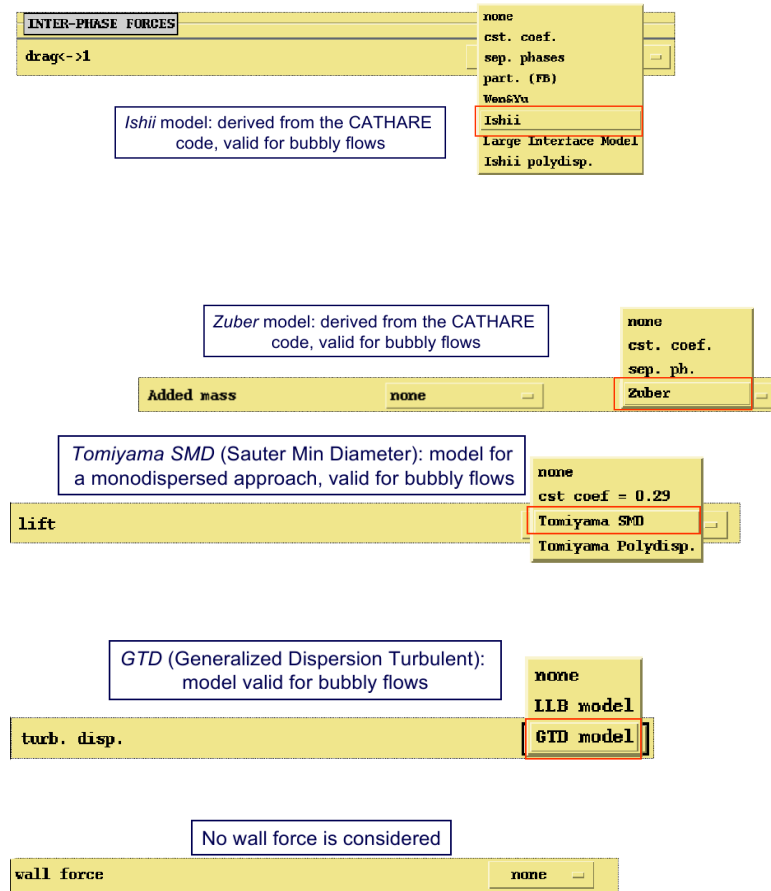


Figure 2.8: Inter-phase forces for liquid and vapor phases

In the `Input-output` control panel, the meshes, the numerical settings and the post-processing outputs are defined. Figure 2.9 shows the panel. In the simulation, two probes are inserted close to the end of the test section. One user array is introduced for the post-processing of the steam bubbles diameter.

The `Generality` panel, as shown in Figure 2.10, contains the physical settings of the simulation. For this case, the gravity is set to the standard value of $9.81m/s^2$ along y axis and the domain length scale is set to $0.01m$. Since the `water/steam` module is defined in the `Special` module panel, the CATHARE table, containing the physical properties of the water and steam phases, are automatically activated. In the `boiling parameter` section, the Extended Kurul-Podovsky model is chosen as heat transfer model from wall to fluid. The fluid properties are calculated at $y^+ = 250$ where y^+ is defined as $y^+ = \frac{y_P U^*}{\nu}$ where y_P is the distance to the wall. U^* defines the friction velocity and ν stands for the cinematic molecular viscosity. In the `Scalar` section, the interface water-

INPUT-OUTPUT-CONTROL <@pool>

? NEPTUNE CFD V1.0.8 param

CONTROLLED MEMORY ALLOCATION

Number of Integers 1000000

Number of Reals 10000000

GEOMETRY FILE

Use of ENVELOPPE module YES

Face joining

Other options

Mesh file name(s) prisme.des

TIME CONTROL

Nbr of time-steps 1000 Restart from previous run

Absolute max time -1

Ref Time-step, dt0 0.001 Saving frequency of restart file suiava 0

Dt mode time-dep Syrthes time step Neptune dt

VARIABLE DT

dt/dt0 min 1e-06 dt/dt0 max 1000000

max dt variation (increase) 0.1

max dt variation (decrease) 0.5

CFL-FOURIER LIMITS

USER

Number of user arrays 1

POST-PROCESS

chrono

output type each n t-step Iteration freq. of chrono outputs 10

Chrono outputs at the MED format

chrono output of nucleate boiling model

histo

output type each n t-step iteration freq. of histo output 1

saving frequency 1000

definition of probes defined in Edamox

number of probes 2

x_prob	y_prob	z_prob
0.006	0.5	0

Close Cancel Help...

Figure 2.9: Input-output control panel

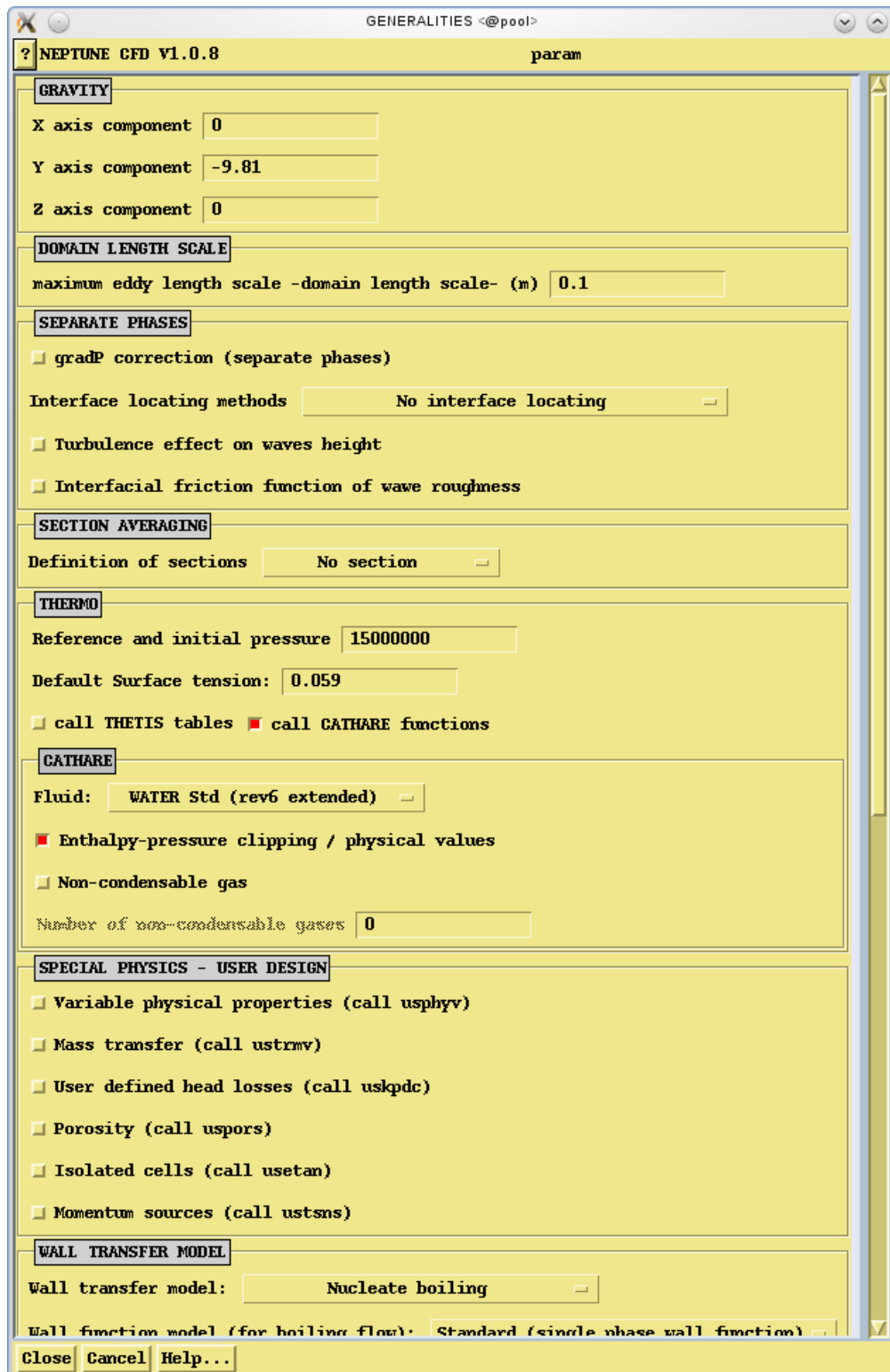


Figure 2.10: Generality panel

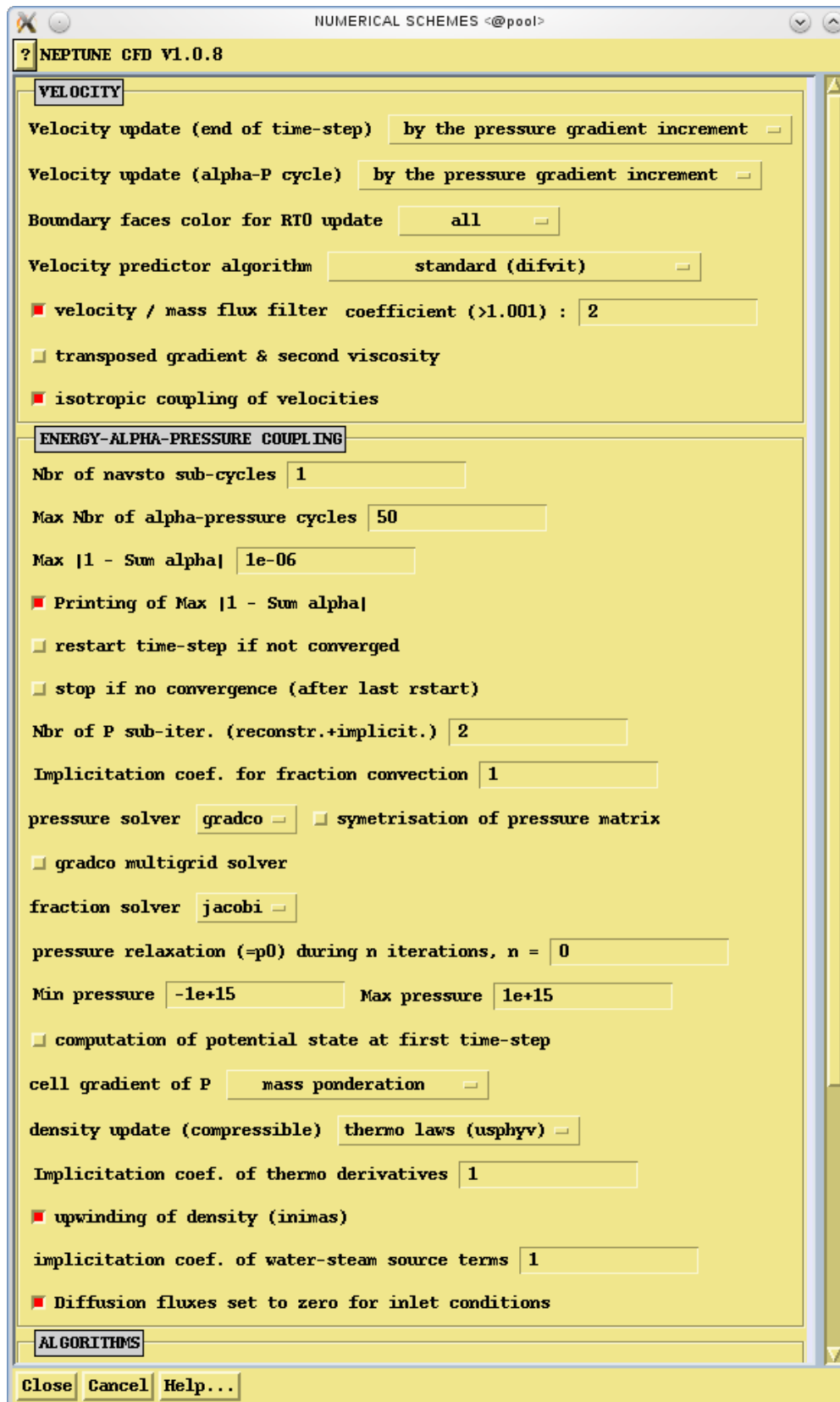


Figure 2.11: Numerical Scheme panel

Number of scalars <input type="text" value="2"/>				
convection	t-dep.	effective diffusion	lam. dyn. coef. (kg/m/s)	turbulent Schmidt
phase 1 <input type="text"/>	<input checked="" type="checkbox"/>	<input checked="" type="checkbox"/>	<input type="text" value="1e-05"/>	<input type="text" value="0.9"/>
phase 2 <input type="text"/>	<input checked="" type="checkbox"/>	<input checked="" type="checkbox"/>	<input type="text" value="1e-05"/>	<input type="text" value="0.9"/>
init. choice	sca. init. value	min val	max val	
at (T0,P0) <input type="text"/>	<input type="text" value="0"/>	<input type="text" value="-1e+20"/>	<input type="text" value="1e+20"/>	
at Hsat(P0) <input type="text"/>	<input type="text" value="0"/>	<input type="text" value="-1e+20"/>	<input type="text" value="1e+20"/>	
type	A-P-H Cycle		name	
total enthalpy <input type="checkbox"/>	<input checked="" type="checkbox"/>	<input type="text" value="totalH1"/>		
total enthalpy <input type="checkbox"/>	<input checked="" type="checkbox"/>	<input type="text" value="totalH2"/>		

Figure 2.12: Scalar panel

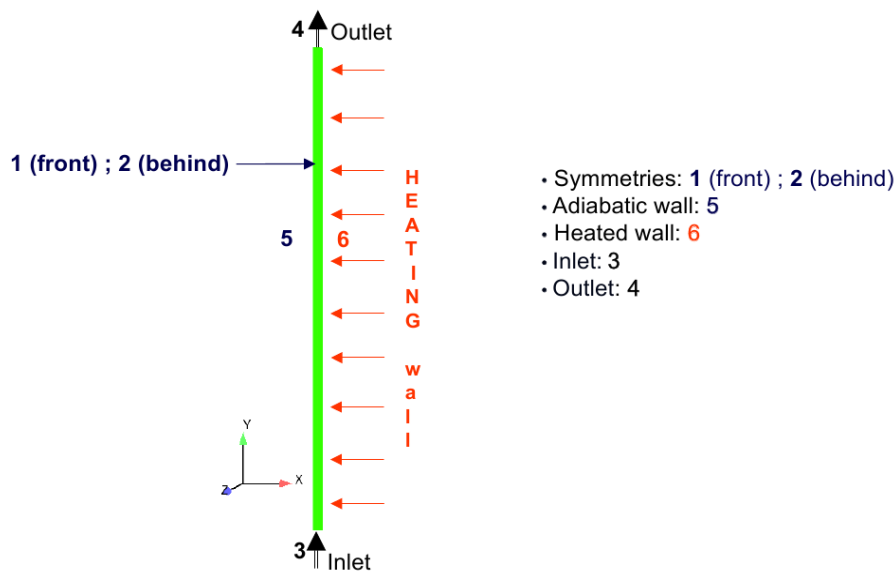


Figure 2.13: Boundary conditions applied on the boiling channel

steam energy transfer for the two phases is specified. For the water and steam phases, the standard bubble models for liquid and vapor are chosen respectively.

In the Numerical Scheme panel, shown in Figure 2.11, the numerical options are setting. For this case, the pressure is bounded between two values (1500000 Pa and 3000000 Pa.). This approach is preferred when thermodynamics tables are used. The

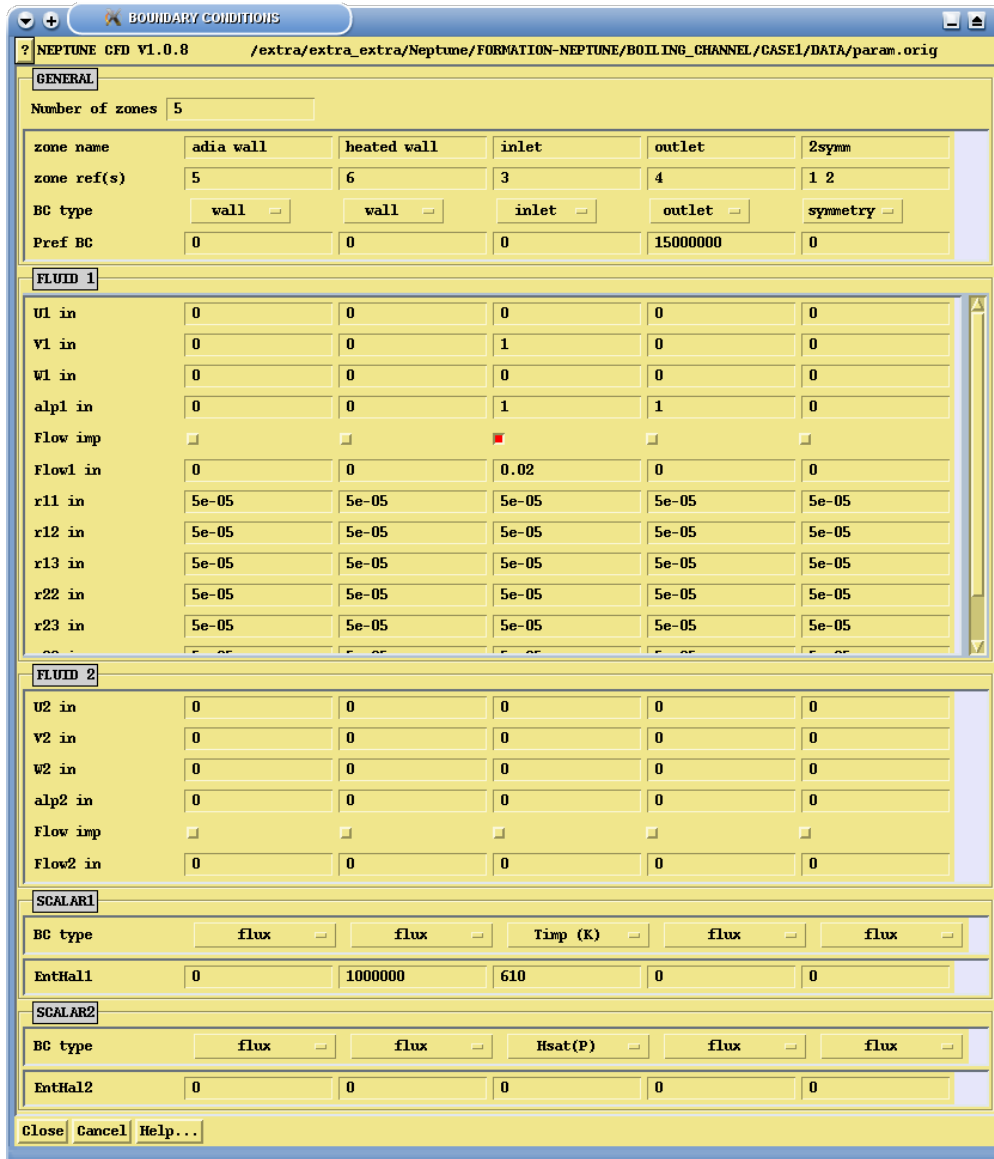


Figure 2.14: boundary conditions panel

restart time-step and the upwinding of the density are set.

In the `Scalar` panel the enthalpies of phase 1 and 2 are initialized respectively at the reference pressure and temperature, and at the enthalpy saturation, depending on the reference pressure P_0 . The Figure 2.4 shows the `Scalar` panel.

The `Boundary Conditions` panel is used to set the specific boundary conditions of the case. Figure 2.13 shows a simplify scheme of the boundary conditions applied

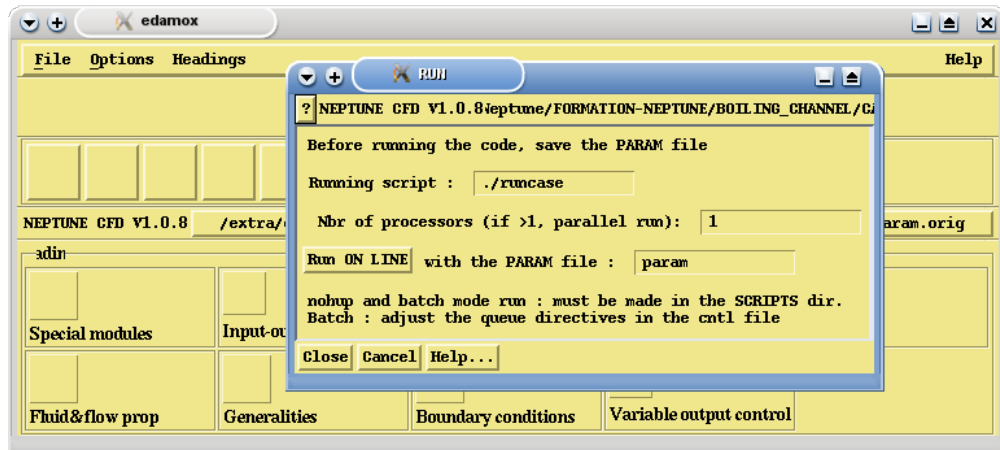


Figure 2.15: Run panel

on each wall. In particular, in the adiabatic wall (number 5), no sliding condition is applied and a Neumann condition is imposed on the two enthalpies. The wall number 6 is heated with an heat flux of 10^6 W/m^2 . The inlet conditions are applied on the wall number 3. For the liquid phase, the velocity is imposed along the y direction, the mass flow rate is set to 0.2 kg/s , and, the enthalpy is imposed for a temperature of 610 K . For the steam phase, the properties are taken at the enthalpy saturation point. The outlet conditions are applied on the wall number 4. In this wall, the reference pressure is imposed and a Neumann condition is applied on the two enthalpies. Figure 2.14 shows the structure of the Boundary Condition panel.

Finally, in the variable output control panel, the probe numbers for each variable and the post processing visualization are set. In this case, the probes are located with the purpose to measure pressure and temperature.

Before running the simulation, it is necessary to save the `param` file. The number of processors is set in the Run panel and the simulation is started with the button `Run on line`. Figure 2.15 shows this Run panel.

Chapter 3

The PERSEO Facility

3.1 The main features of the PERSEO test facility

3.1.1 Introduction

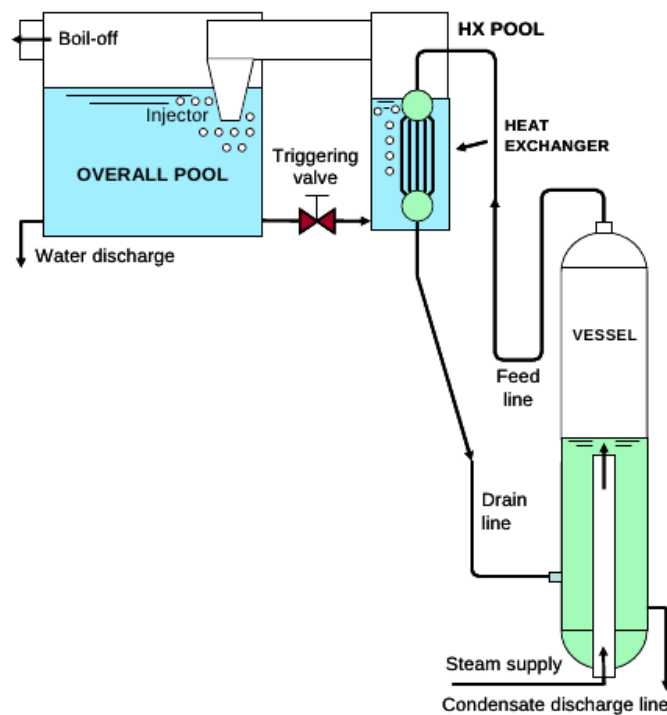


Figure 3.1: Scheme of the PERSEO facility

Within the frame of a research activity on innovative safety systems for Light Water Reactors at SIET laboratories (Piacenza) and in collaboration with ENEA, particular

attention is addressed to increase the reliability of Decay Heat Removal Systems that implement in-pool heat exchangers. In particular a system able to remove the decay power from the primary side of a LWR is studied, able to be actuated without installing any mechanical device (valve) on the primary loop [22].

In the past, two examples of energy removal systems utilizing in-pool heat exchangers were proposed to be installed in the GE-SBWR and in the Westinghouse *AP – 600*: the (IC) Isolation Condenser and the PRHR (Passive Residual Heat Removal), respectively. In both of these systems, the heat transfer was actuated by opening a valve installed on the primary side of the reactor [23]. The first proposal of moving the primary side valve (high pressure) to the pool side (low pressure) was studied by CEA and ENEA in the Thermal Valve concept. In this case, the valve was located, steam side, at the top of a bell covering the pool immersed heat exchanger. Closed during normal operation, the valve prevented the heat transfer due to the formation of steam under the bell, while in emergency conditions (e.g. primary circuit high pressure) the valve opening caused the discharge of the insulating steam and the beginning of heat transfer from the primary side to the pool.

The PERSEO (in-Pool Energy Removal System for Emergency Operation) project is an evolution of the Thermal Valve concept where the triggering valve is installed liquid side, on a line connecting two pools at the bottom. The valve is closed during normal operation and the pool containing the heat exchanger (HX Pool) is empty. The other pool (Overall Pool) is full of cold water. In emergency conditions the valve is opened, the heat exchanger is flooded with consequent heat transfer from the primary side to the pool. Moreover, the pools are connected at the top by means of a pipe, ending with an injector, accelerating the produced steam under water (from the HX Pool to the Overall Pool) in order to promote the circulation and the homogenization of water and to delay the boiling and steam release in the containment. A new experimental facility was designed and the system was simulated with the Relap5 code in order to optimize the dimensions of the HX Pool [24], [25]. The PERSEO facility was built at SIET laboratories by modifying the existing PANTHERS IC-PCC facility (Performance Analysis and Testing of Heat Removal System Isolation Condenser - Passive Containment Condenser), utilized in the past for testing a full scale module of the GE-SBWR in-pool heat exchanger.

3.1.2 Test facility geometry

The PERSEO facility mainly consists of two main facilities: the primary side and the pool side. Figure 3.1 shows the scheme of the PERSEO facility; Figures 3.2 and 3.3 show the specific schemes of primary and secondary loops.

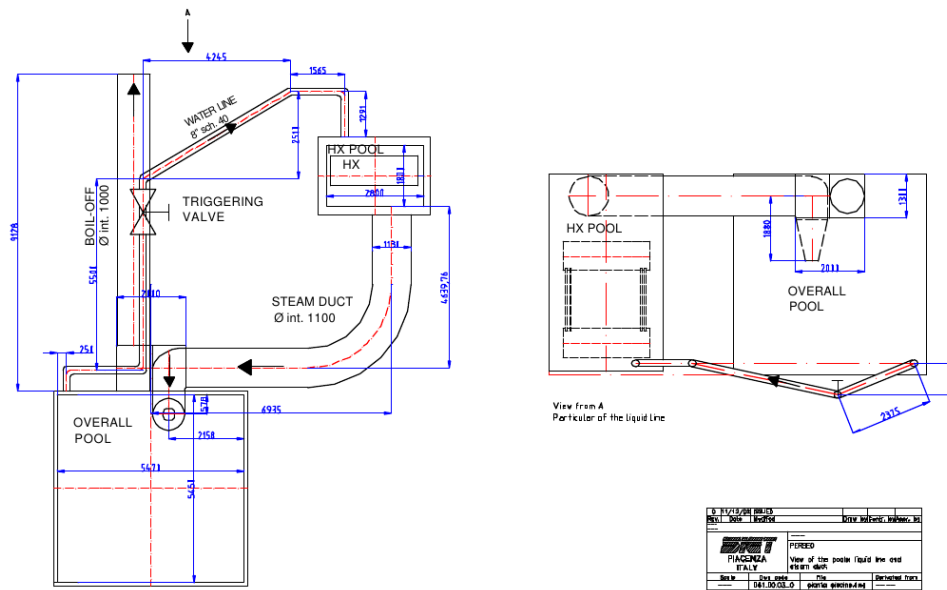


Figure 3.3: PERSEO facility Steam Duct and Liquid Line between the pools

The pressure vessel can operate at the thermal-hydraulic conditions typical of a BWR or the secondary side of a PWR steam generator. Its volume is 43 m^3 , the height is 13 m and it is partially filled with saturated water with a nominal level 7.04 m . It is provided with an internal vertical riser, a steam separator and dryer. The Heat Exchanger consists of two inconel 600 cylindrical headers and 120 vertical pipes. The header internal diameter is 0.63 m and thickness 0.06 m , the length is 2.48 m (covers included) and the volume is 0.732 m^3 . The pipe outer diameter is 0.0508 m and thickness 0.0023 m , average length 1.8 m . The Heat Exchanger is located in the HX Pool. The Steam Line is a 10 inch sch. 80 pipe connecting the pressure vessel to the heat exchanger inlet. The Drain Line is a 6 inch sch. 80 pipe connecting the heat exchanger outlet to the pressure vessel.

The HX Pool has a volume of 28.7 m^3 with a basis area of 5.04 m^2 and a height of 5.7 m . The HX Pool bottom is 0.1 m over the Overall Pool bottom. It consists of stainless steel sheets reinforced by iron beams. A diaphragm is located, slightly inclined, over the heat exchanger and contributes to the steam-water separation during the system operation. The Overall Pool has a volume of 173 m^3 with a basis area of 29.84 m^2 and a height of 5.8 m . It contains the old heat exchanger of the Panthers-PCC facility not used in these tests. It consists of fiberglass walls reinforced by iron beams.

The liquid line connecting the Overall Pool bottom to the HX Pool bottom is an 8 inch sch. 40 pipe. It contains the triggering valve (8 inch diameter manual valve). The Steam Duct is an horizontal fiberglass pipe (OD 1.13 m , ID 1.1 m) connecting the HX

Pool to the Overall Pool. The terminal part of the Steam Duct, ending into the Overall Pool, is a conical injector built in stainless steel.

3.1.3 Circuit configuration and operation

The PERSEO facility design features are listed in table 3.1

Description	Unit	Value
Power	20	<i>MW</i>
Vessel Pressure	10	<i>MPa</i>
Vessel temperature	310	$^{\circ}C$
Heat exchanger pressure	8.62	<i>MPa</i>
Heat exchanger temperature	302	$^{\circ}C$
Superheated steam flowrate	12	<i>kg/s</i>
De-superheating water flowrate	3	<i>kg/s</i>
Pool side pressure	0.15	<i>MPa</i>
HX Pool temperature	300	$^{\circ}C$
Overall Pool temperature	130	$^{\circ}C$
Pool side make up water flowrate	25	<i>kg/s</i>

Table 3.1: PERSEO facility design features

In order to simulate the execution tests, *initial conditions* are imposed to the facility. In particular, for the primary side, the pressure vessel is maintained in saturation conditions typical for BWRs or secondary side of PWR steam generators ($P = 7$ MPa). This is done by supplying properly de-superheated steam coming from a nearby power station. The pressure is kept constant by controlling the steam supply valve, while the water level in the vessel is maintained at the specified value for the test by discharge of water through the condensate discharge line at the vessel bottom. Moreover, at the initial state, the heat exchanger is full of saturated steam, the Overall Pool is full of cold water, the HX Pool is full of air or steam, depending on the specified test and the triggering valve is closed.

Once reached a steady state condition according to the test matrix, the triggering valve is opened and the HX Pool is flooded by cold water leading to steam condensation inside the HX tubes with power transfer from the primary side to the pool side. As soon as pool water boiling starts, the steam produced in the HX Pool is driven to the Overall Pool through the steam duct. The injector flowing about 1.3 m below the water level contributes to mix the Overall Pool water, thus limiting temperature stratification within the pool. The condensation of steam inside the Overall Pool leads to progressive cold water heat-up until reaching the boiling point. The steam produced in the Overall

Pool flows outside at atmospheric pressure through the boil-off pipe. When the injector is uncovered the Overall Pool level decreases according to the heat transfer rate since no condensation is present anymore and the steam flows outside directly through the boil-off pipe and the water reserve line of the HX Pool. During the system operation, the natural circulation which stabilizes on both primary and secondary sides determines the power evacuated by the system.

3.2 PERSEO experimental data

A set of instruments for conventional thermal-hydraulic measures is provided in the PERSEO facility. Direct measures of pressure, differential pressure, temperature and strain are performed. Hence, some of these quantities are utilized to obtain derived quantities like levels, flow rates and energies. Figures 3.4-3.5 shows the probes position in the two pools. For the protection of the plant, a pressure indicator is installed on the Main supply line to switching off the main steam valve in case of overpressure. All the instruments are calibrated in the SIET metro-logical laboratory. The nominal accuracy of the Differential Pressure Transmitters is $\pm 0.1\%$ of the instrument full scale. The nominal accuracy of the Pressure Transmitters is $\pm 0.25\%$ of the instrument full scale while the nominal accuracy of the Differential Pressure Transducers is $\pm 0.25\%$ of the instrument full scale. The nominal accuracy of the thermocouples and the nominal accuracy of the Resistor Thermal Detector are, respectively, $\pm 1.05^\circ C$ and $\pm 1.5^\circ C$.

3.3 Experimental text MATRIX

The PERSEO facility set-up was conducted by executing a series of shake down tests suitable to verify the correct plant operation and to characterize the main parameters of the facility, in particular the water pouring-off from the Overall Pool to the HX Pool. The shake down tests matrix and a short description of tests are reported in Table 3.2. Two different kinds of PERSEO actual tests are suitable for the system concept demonstration, *Integral tests* and *Stability tests*. The integral tests aimed at demonstrating the behavior of the system following a request of operation and during all phases of a long accidental transient. These tests are executed at two different primary side pressures: 4 and 7 MPa.

The stability tests are finalized to study particular critical problems happening in case of sudden condensation at the steam-water interface in the Injector or in case of triggering valve re-opening with cold water inlet in presence of steam. These tests are performed at 7 MPa primary side pressure. The PERSEO tests matrix, the main conditions and a short description of tests are shown in Table 3.3.

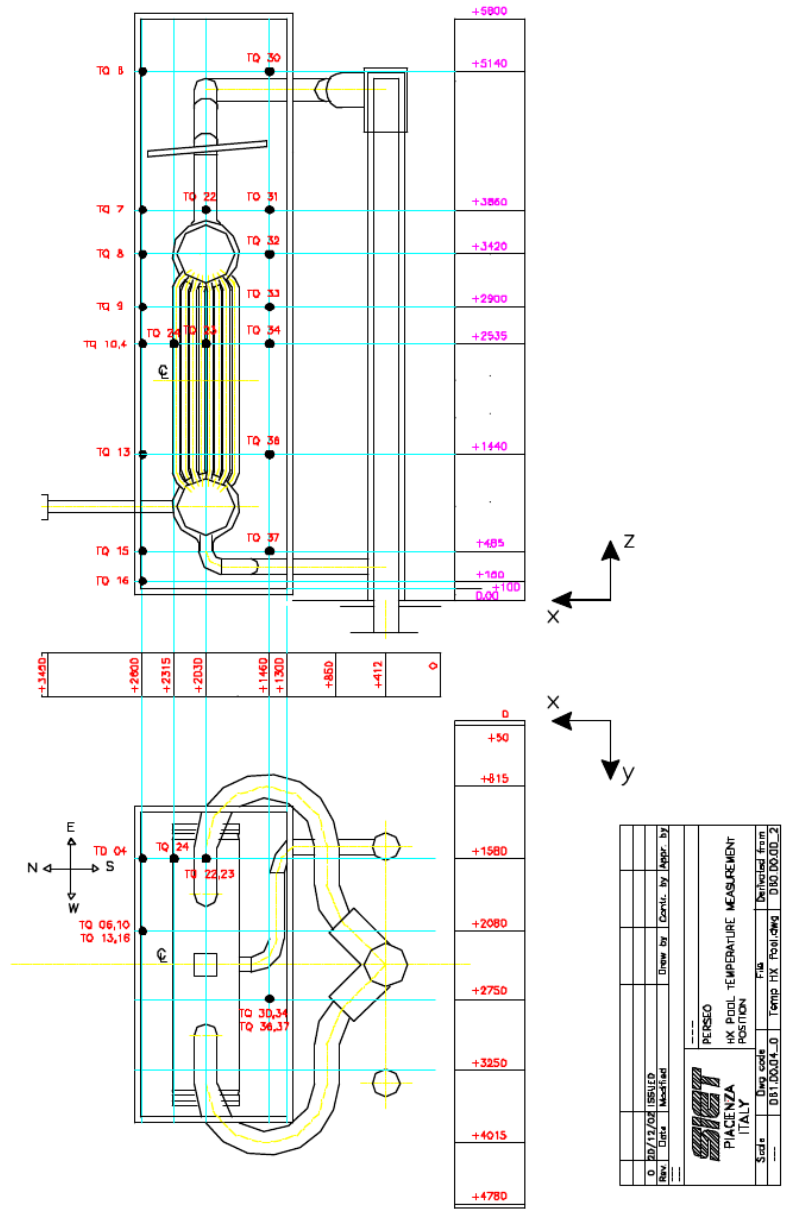


Figure 3.4: Hx Pool temperature measurement position

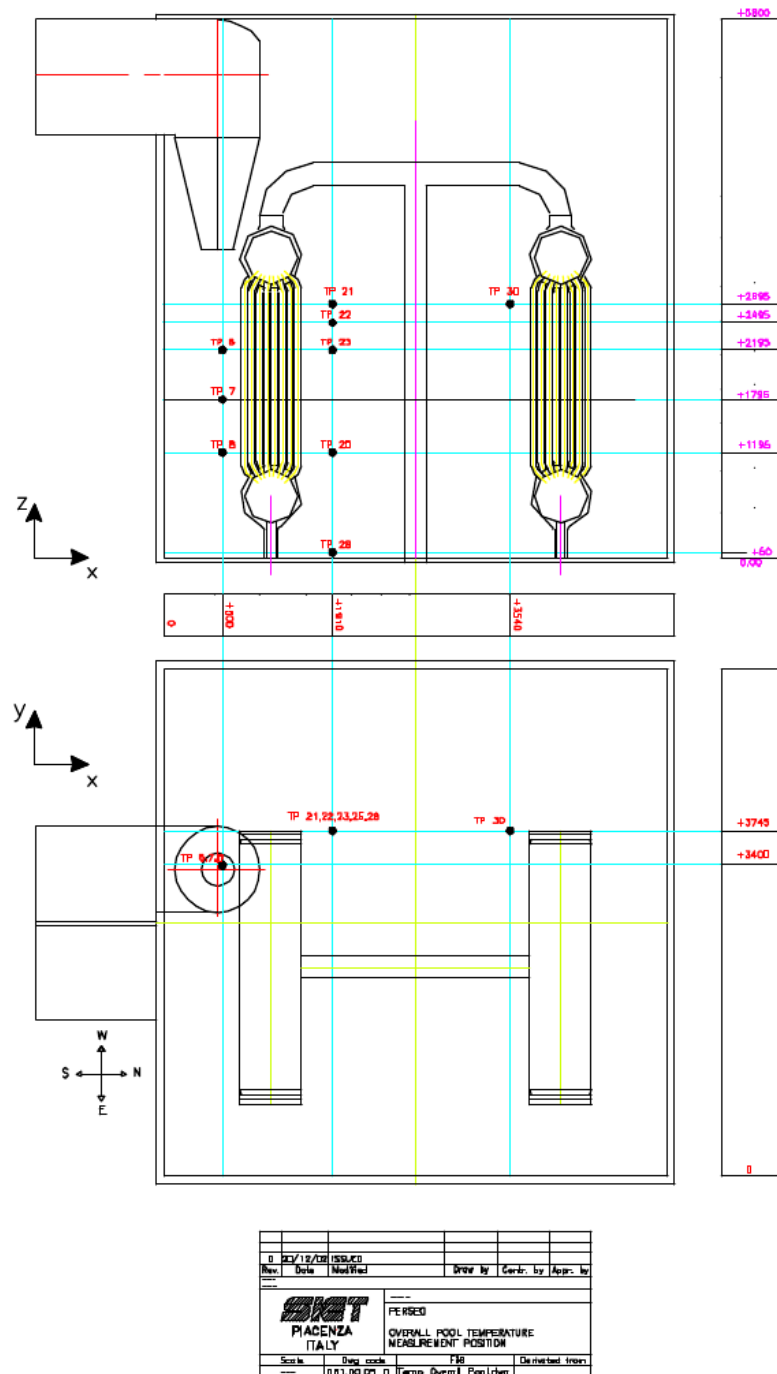


Figure 3.5: Overall Pool temperature measurement position

Test	Test conditions	Description
1	Atmospheric pressure, cold conditions.	Pool side check: cold water poor-off from Overall Pool to HX Pool with HX Pool uncovered
2	Atmospheric pressure, cold conditions.	Pool side check: cold water poor-off from Overall Pool to HX Pool with HX Pool covered
3	Primary side pressure up to 6 MPa in saturation conditions.	Adiabatic test: pressurization and heat-up of the primary side with HX Pool empty.
4	Primary side pressure: 4 MPa	Integral test.
5	Primary side pressure up to 9 MPa. Cold conditions.	Primary side pressurization

Table 3.2: PERSEO shake-down test matrix

Test	Test conditions	Description
6	Primary side pressure: 7 MPa	Integral test interrupted at the beginning of the pool level decreasing.
7	Primary side pressure: 7 MPa	Stability and integral test Partial and subsequent HX Pool filling with reaching of boiling conditions and level decreasing.
8	Primary side pressure: 7 MPa	Stability test Partial HX Pool filling with reaching of boiling conditions.
9	Primary side pressure: 4 MPa	Integral test.

Table 3.3: PERSEO test matrix

The main steps of the integral test procedure are the following:

1. pressurization of the primary circuit to the required pressure
2. opening of the triggering valve
3. reaching of saturation conditions in HX Pool and Overall Pool
4. level decrease in the pools down to Injector outlet uncovering
5. level decrease accelerated down to about 3 m from the pool bottom by water discharge
6. triggering valve closure and HX Pool boil-off
7. depressurization of the primary circuit

Moreover, the main steps of the stability test procedure are the following:

1. HX pool full of air
2. pressurization of the primary circuit to the required pressure
3. opening of the triggering valve
4. closure of the triggering valve when HX Pool water level reaches the heat exchanger pipe bottom
5. wait for steam production and check for condensation and instabilities
6. re-opening of the triggering valve
7. check for condensation and instabilities with cold water inlet into the HX pool in presence of steam

The tests confirmed the effectiveness of the PERSEO innovative system: the heat transfer from the primary to the pool side is soon actuated after the triggering valve opening, it is stable and decreases according to the HX Pool level. The Steam generated in the HX Pool and accelerated into the Overall Pool by the Injector promotes the water circulation and avoids the thermal stratification in the Overall Pool. Instabilities due to sudden steam condensation, evidenced after an early interruption of the heat transfer and during the HX Pool re-flooding to restart the heat removal, are dumped very soon by means of the vacuum breaker valve at HX Pool top or on the Steam Duct.

In the present work, the stability (Phase 1) and integral (Phase 2) Test n.7 and the integral Test n.9 have been analyzed and studied with CATHARE code and Neptune.CFD code.

3.3.1 Test n.7

Parameter	Unit	Test n.7
Primary side Pressure	<i>MPa</i>	7
Primary side Temperature	<i>°C</i>	285
Primary steam flowrate	<i>kg/s</i>	13
HX extracted Power	<i>MW</i>	20
HX Pool side Pressure	<i>MPa</i>	0.12
HX Pool side Temperature	<i>°C</i>	105
HX Pool Steam flowrate	<i>kg/s</i>	9

Table 3.4: Main PERSEO test 7 parameters in phase 1

The test n.7 foresees the system actuation with partial HX Pool fill-up (Phase 1) followed by the HX Pool total fill-up with reaching of boiling conditions and pool level decreasing (Phase 2), with the primary side pressure of 7 MPa . The main Test parameters at full power operation during the transient phase are listed in Table 3.4. This test is defined to investigate the system actuation and the trend of power with a low HX Pool level, the presence of instabilities due to steam condensation at the interface between water and steam in the Injector. Moreover, this test verifies the system re-actuation consequent to the HX Pool filling-up and reaching of the thermal regime in both the pools, the effectiveness of the Injector in mixing the Overall Pool water, the power and flow regime variation after the Overall Pool level decreases below the Injector outlet and the trend of power as a function of the water level in the pools, decreasing for the loss of mass through the boil-off.

Test 7 - phase 1

Event and phenomena	Time (s)	Quantity
HX Pool partial flooding		
1 st partial triggering valve opening and closure	300-433	
2 st partial triggering valve re-opening and re-closure	446-480	
Maximum level in the HX Pool (1.41 m)	508	
Maximum exchanged power		3.5 MW
Minimum level in the HX Pool (1.40 m)	874	
Overall Pool average temperature		17°C
Instabilities for steam condensation in the Injector	755-1115	
HX Pool total flooding		
3 st partial triggering valve opening and closure	864-1085	
Maximum level in the HX Pool (3.4 m)	875	
Maximum exchanged power		21.5 MW
HX Pool minimum level (1.25 m)	4625	
Overall Pool average temperature		70°C

Table 3.5: Chronology of main events of Phase 1

The Phase 1 of Test n. 7 foresees the system actuation with partial HX Pool fill-up without reaching of boiling conditions in the Overall Pool. This test phase is aimed at verifying the system behavior during start-up. The chronology of main events characterizing the conduct of the test is shown in Table 3.5.

In the initial status the Overall Pool is full of cold water at 4.62 m level from the pool bottom, the HX Pool is empty and covered and the primary side is active.

The triggering valve begins to be opened slowly at time 300 s, then it is completely

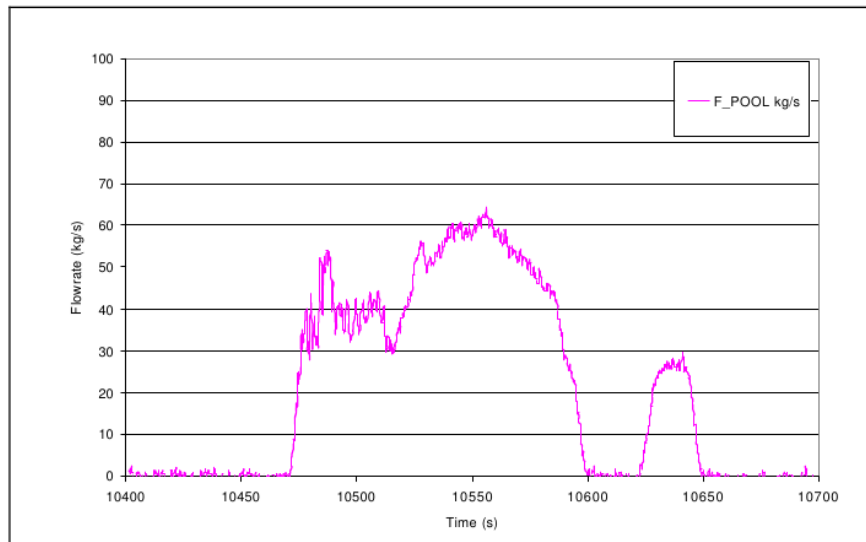


Figure 3.6: Water flowrate between the pools (partial HX Pool fill-up)

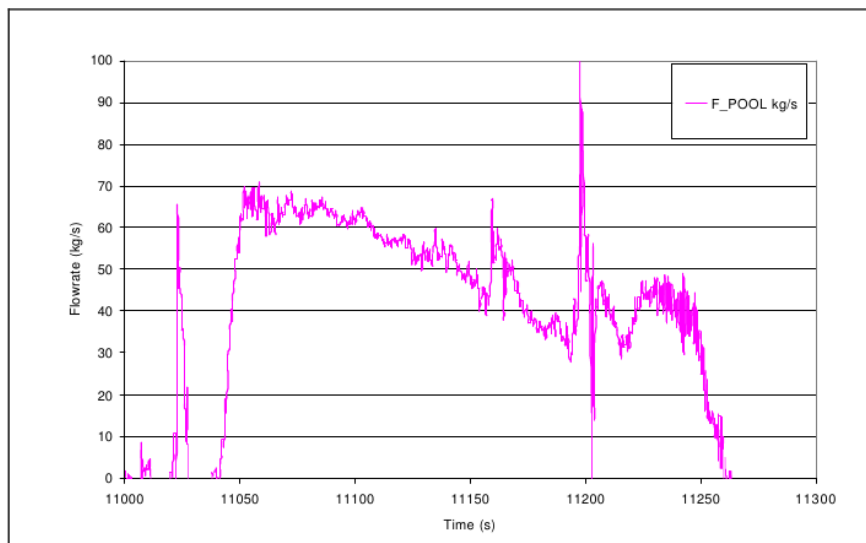


Figure 3.7: Water flowrate between the pools (total HX Pool fill-up)

closed at 433 s. At time 446 s a further opening is actuated and the valve is completely closed at 480 s. This sequence valve opening and closure represents the first step of water injection.

The second step of water injection occurs when the valve is opened at 864 s and completely closed at 1085 s. The water flowrate between the pools (derived by the HX Pool level) for the first and second phase of injection is reported in Figures 3.6 and 3.7,

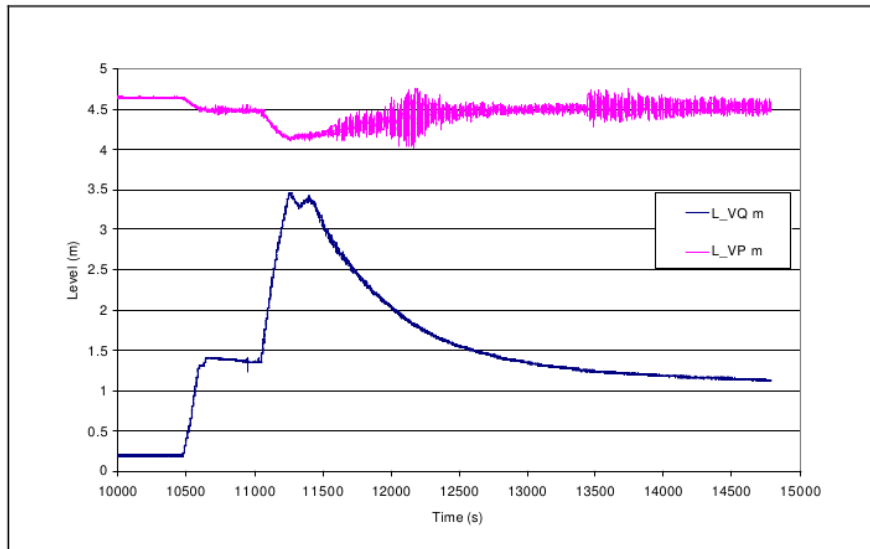


Figure 3.8: HX Pool and Overall Pool levels

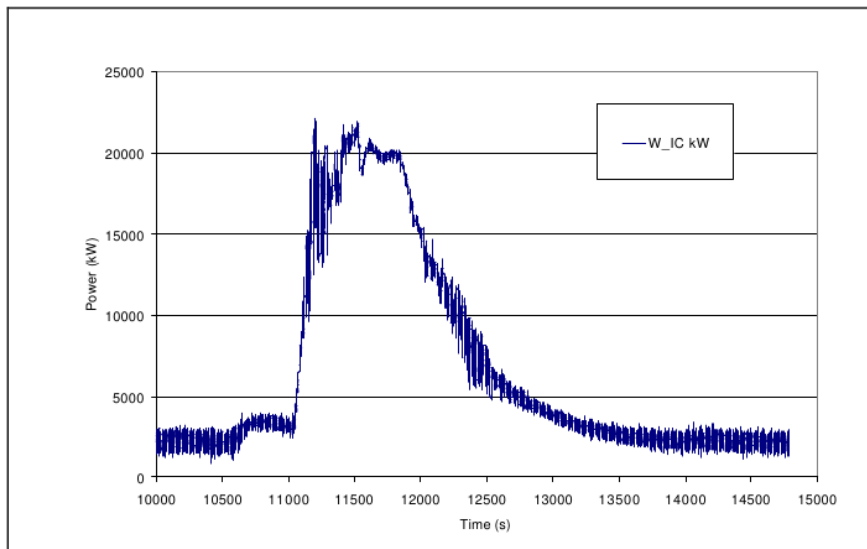


Figure 3.9: HX exchanged power

respectively. The HX Pool level begins to increase at time 308 s. At time 508 s, the HX Pool reaches the level of about 1.41 m, then it decreases slowly down to about 1.40 m (Figure 3.8). At time 905 s, level increases again up to 3.4 m, following the second water injection. Then, level decreases down to the minimum value of 1.3 m. The Overall Pool level decreasing is observed during the two water pouring-off towards the HX Pool (Figure 3.8), then level increases slowly due to the Overall Pool water heat-up and

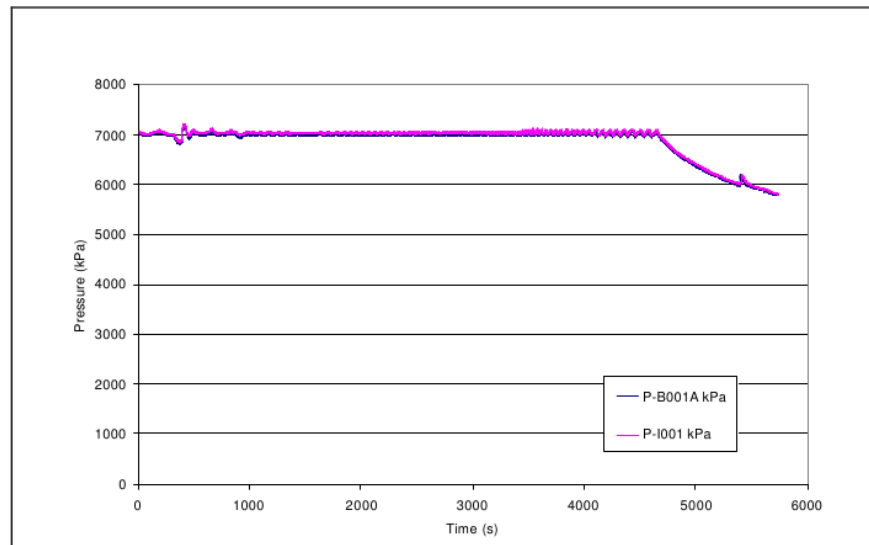


Figure 3.10: Primary side pressure

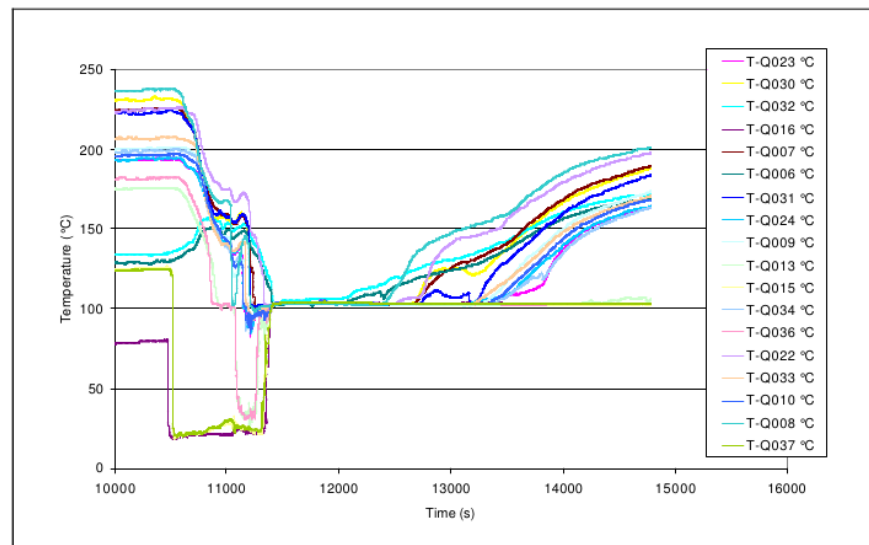


Figure 3.11: HX Pool temperatures

density diminution.

After the first step of water pouring-off, power exchanged from the primary to the pool side is quite low (around $3.5 MW$), because of the low water level in the HX pool, while it increases by increasing the level up to reaching the maximum value of about $21 MW$. Later, power decreases following the trend of level in the HX Pool, as shown in Figure 3.9. When level reaches the minimum value of $1.3 m$, the exchanged power

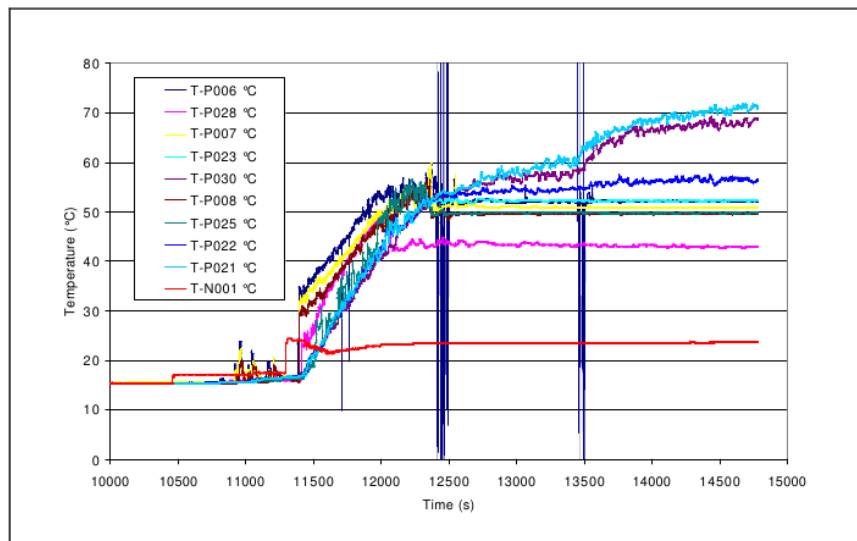


Figure 3.12: Overall Pool temperatures

is about 2.5 MW. After the triggering valve is opened for the second injection and power begins to be exchanged heavily from the primary to the pool side, the primary side pressure decreases rapidly, so it is manually increased in order to compensate the pressure decreasing due to the heat removal. After about 550 s, the pressure average value returns to 7 MPa, (Figure 3.10).

The HX Pool temperatures are shown in Figure 3.11. Before the water injection, the air contained in the pool is hot, due to the HX radiation. Then, after the first step of the water injection, temperature decreases slowly for the steam production. Successively, after the second step of water injection, the Temperature decreases more rapidly. The saturation is reached early and temperature stabilizes around 104 °C, corresponding to the saturation at the pressure in the pool.

The Overall Pool temperatures are shown in Figure 3.12. In this condition, even if the steam is not sufficient to circulate water in the Overall Pool, no depressurization strike is observed because the water temperature at the steam-water interface in the Injector is high (around 70 °C).

Test 7 - phase 2

The Phase 2 of Test n.7 foresees the system actuation with total HX Pool fill-up followed by reaching of boiling in the OP and water level decreasing. This phase of the test is aimed at demonstrating the correct system behavior during long term accidental transient. The chronology of main events characterizing the conduct of the test is shown in

Event and phenomena	Time (s)	Quantity
HX Pool partial flooding		
Triggering valve opening	326 (opened in 26 s)	
Maximum level in the HX Pool (3.25 m)	531	
Maximum exchanged power		21 MW
Overall Pool average temperature		85°C
Overall Pool water discharge opening	1150	
Onset of the Overall Pool water boiling	1400	
Overall Pool water discharge closure	3230	
HX Pool level (2.07 m)	3230	
Triggering valve closure	3338 (closed in 123 s)	
Maximum level in the HX Pool (3.4 m)	11050	
Maximum exchanged power		21.5 MW
Primary side depressurization beginning for end of test	4685	

Table 3.6: Chronology of main events of Phase 2

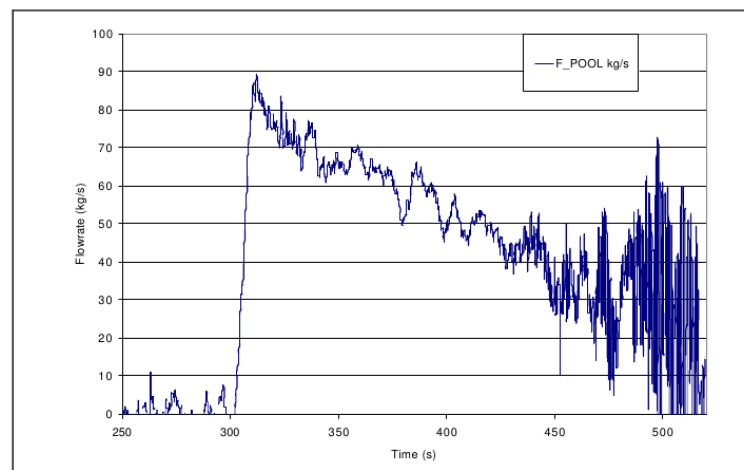


Figure 3.13: Water flowrate between the pools (2 Phase)

Table 3.6.

The second part of the test starts with the HX Pool water level of 1.2 m in saturation conditions, the Overall Pool full of warm water and the primary side pressure at 7 MPa. The triggering valve begins to be opened at time 300 s and it is completely open at 326 s. Then it is closed at 3338 s in 123 s in order to isolate the two pools and investigate the trend of power as a function of the HX Pool level.

The water flowrate between the pools (derived by the HX Pool level) is reported in Figure 3.13 and it is valid only for the first phase of the water injection (300 s to 500 s).

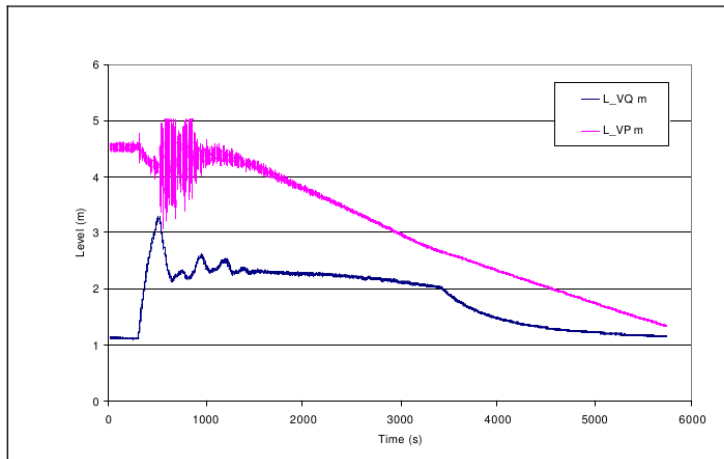


Figure 3.14: HX Pool and Overall Pool water level (2 Phase)

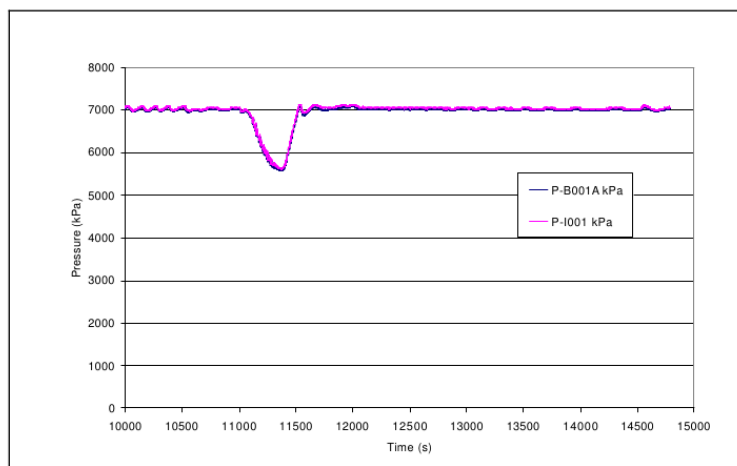


Figure 3.15: Primary side pressure (2 Phase)

The HX Pool level begins to increase at time 310 s. At time 531 s, the HX Pool reaches the maximum level of 3.25 m, then oscillations follows until about 1500 s Figure 3.14. The Overall Pool level is reported in the same figure. After the early level decreasing for the water pouring-off to the HX Pool, strong and fast oscillations are observed, due to the condensation of steam produced in the HX Pool and flowing through the Steam Duct. At time 1150 s, when the Overall Pool temperature is between 80°C and 90°C, the level decreasing in the pools is accelerated by opening the discharge valve. When the Overall Pool level is around 2.8 m (about 3230 s), the discharge valve is closed. At this point, the Injector outlet is uncovered and the steam flows directly outside through

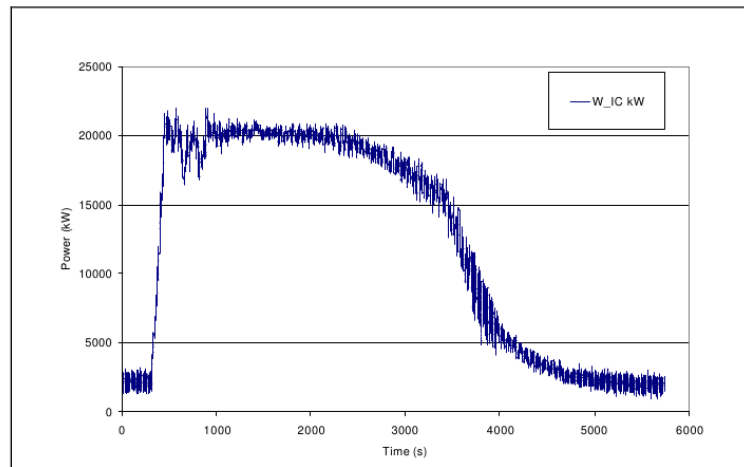


Figure 3.16: HX exchanged power (2 Phase)

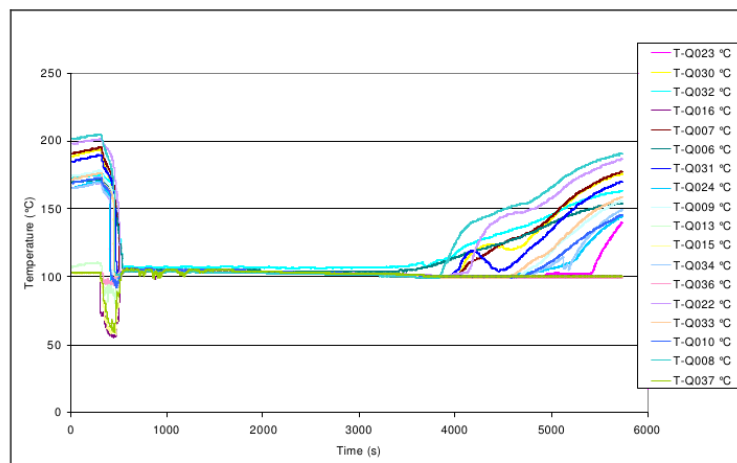


Figure 3.17: HX Pool temperatures (2 Phase)

the boil-off pipe.

In order to compensate the pressure decreasing due to the heat removal, the primary side pressure is manually increased. After some oscillations, the pressure average value returns to 7 MPa remaining stable until the depressurization of the plant is started at 4685 s (Figure 3.15).

The exchanged power is shown in Figure 3.16. After the triggering valve between the two pools is closed, the HX Pool level decreases more rapidly and consequently the exchanged power. The condensed steam flowrate at the maximum exchanged power is about 13 kg/s .

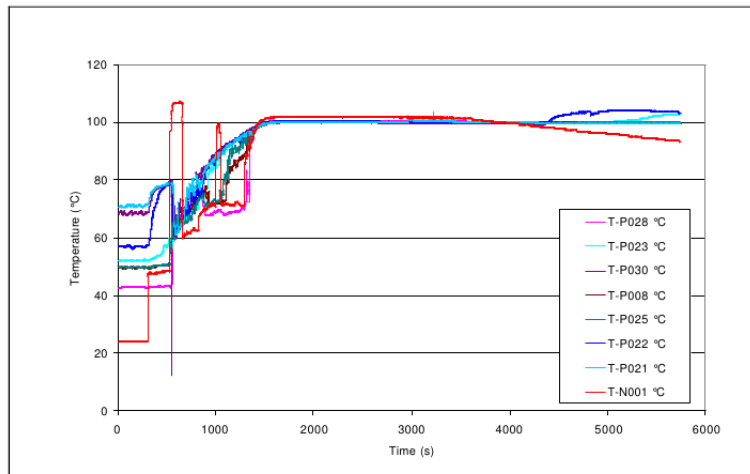


Figure 3.18: Overall Pool temperatures (2 Phase)

The HX Pool temperatures are shown in Figure 3.17. Before the water injection, superheated steam (due to the HX radiation) is contained in the upper part and sub-cooled water in the lower one. After the HX Pool flooding and water boiling, all temperature stabilize around 104°C , corresponding to the saturation at the pressure in the pool. Steam, accelerated into the Overall Pool by the Injector, promotes the water circulation and mixing until the Overall Pool decreasing is accelerated and the Injector outlet uncovered.

The Overall Pool temperatures are shown in Figure 3.18. The peaks observed around 650 and 1040 s are due to level oscillations between the pools and water transfer from the HX to the Overall Pool through the water line.

3.3.2 Test n.9

Parameter	Unit	Test n.9
Primary side Pressure	MPa	4
Primary side Temperature	$^{\circ}\text{C}$	250
Primary steam flowrate	kg/s	8
HX extracted Power	MW	14
HX Pool side Pressure	MPa	0.12
HX Pool side Temperature	$^{\circ}\text{C}$	105
HX Pool Steam flowrate	kg/s	6.5

Table 3.7: Main PERSEO test 9 parameters

Event and phenomena	Time (s)	Quantity
HX Pool partial flooding		
Triggering valve opening	142 (opened in 21 s)	
Maximum level in the HX Pool (3.33 m)	416	
Maximum exchanged power		21 MW
Overall Pool average temperature		85°C
Overall Pool water discharge opening	2790	
Onset of the Overall Pool water boiling	3200	
Overall Pool water discharge closure	4840	
HX Pool level (2.07 m)	4840	
Triggering valve closure	4887 (closed in 93 s)	
Maximum level in the HX Pool (3.4 m)	11050	
Maximum exchanged power		21.5 MW
End of the test	7708	

Table 3.8: Chronology of main events of test 9

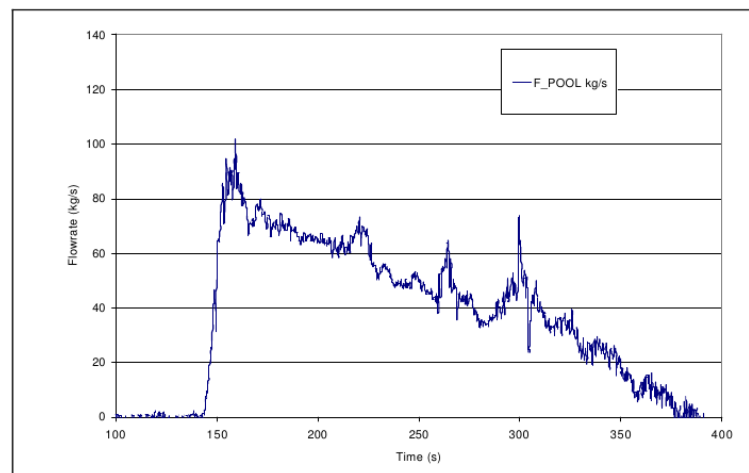


Figure 3.19: Water flowrate between the pools

Like in Test n. 7, the Test n. 9 foresees the system actuation with total HX Pool fill-up followed by reaching of boiling conditions and pool level decreasing. Table 3.7 shows the main test parameters.

This test is aimed at demonstrating the correct system behavior during long term accidental transient under reduced primary side pressure (4.1 MPa). It is performed to investigate the system actuation consequent to the HX Pool fill-up and reaching of the thermal regime in both the pools, the effectiveness of the Injector in mixing the Overall Pool water, the power and flow regime variation after the Overall Pool level decreases

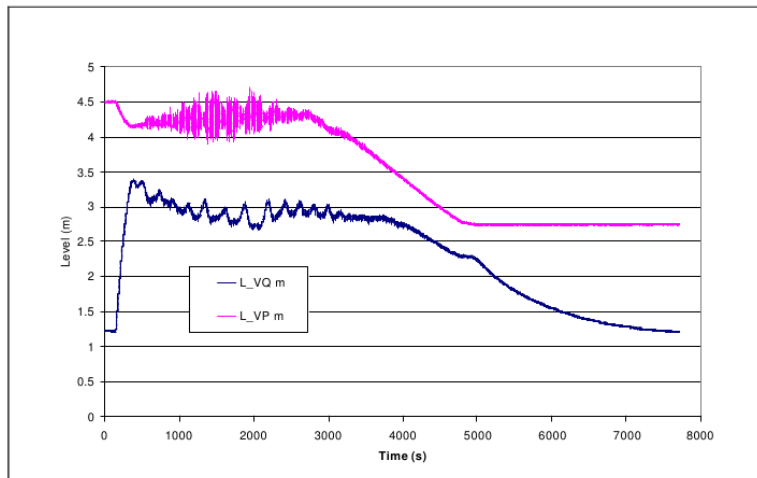


Figure 3.20: HX Pool and Overall Pool water level

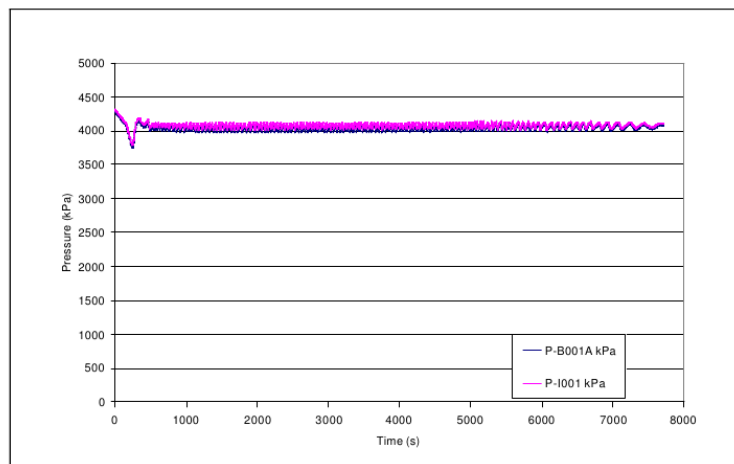


Figure 3.21: Primary side pressure

below the Injector outlet and the trend of power as a function of the water level in the pools, decreasing for the loss off mass through the boil-off.

The chronology of main events characterizing the conduct of the test is shown in Table 3.8.

The described transient begins with the primary side pressure at about 4.1 MPa and the HX Pool water level of 1.2 m . The triggering valve begins to be opened at time 142 s and it is completely opened at 163 s (21 s opening time). The water flowrate between the pools (derived by the HX Pool level) is reported in Figure 3.19. After full opening of the

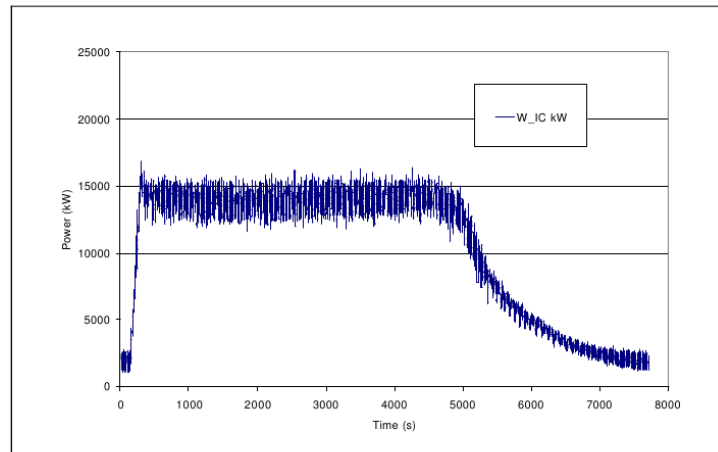


Figure 3.22: HX exchanged power

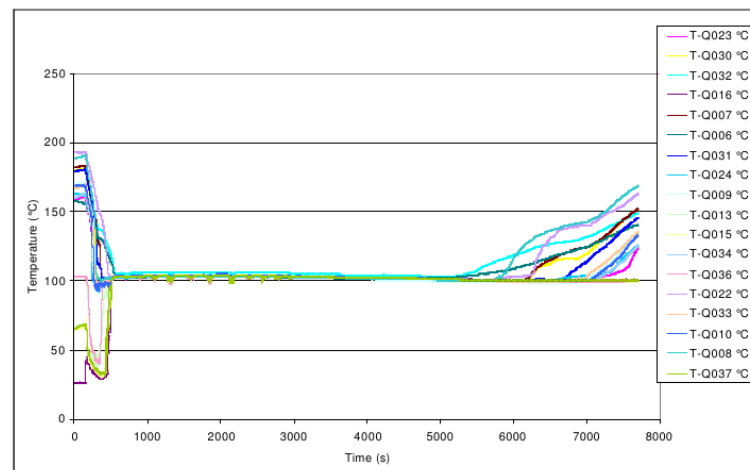


Figure 3.23: HX Pool temperatures

triggering valve the collapsed water level in the HX Pool quickly increases stabilizing close to the top of tube bundle (see Figure 3.20). The Overall Pool level is reported in the same figure. The progressive decrease of the Overall Pool level is started by water discharge from the bottom at 2790 s, approximately 400 s before the onset of boiling. The water discharge is stopped at 4840 s, that is 140 s before complete triggering valve closure. At this point, the Injector outlet is uncovered and steam flows directly outside through the boil-off pipe.

After the triggering valve is opened and power begins to be exchanged from the primary to the pool side, the primary side pressure is manually increased in order to com-

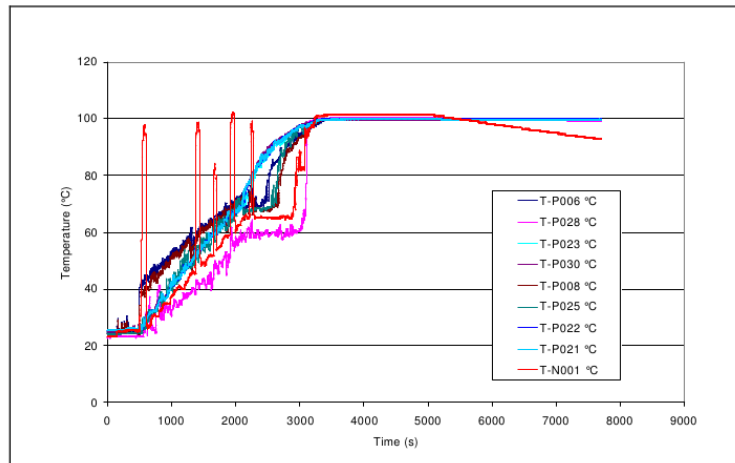


Figure 3.24: Overall Pool and pool connecting line temperatures

compensate the pressure decreasing due to the heat removal. After some oscillations, the pressure average value returns to 4.1 MPa remaining stable until the end of test (see Figure 3.21).

The exchanged power is shown in Figure 3.22. After the triggering valve between the two pools is closed (from 4887 s to 4980 s), the HX Pool level decreases more rapidly and consequently the exchanged power.

The HX Pool temperatures are shown in Figure 3.23. Before the water injection, superheated steam (due to the HX radiation) is contained in the upper part and sub-cooled water in the lower one. After the HX Pool flooding and water boiling, all temperature stabilize around $103.5 \text{ }^\circ\text{C}$, corresponding to the saturation at the pressure in the pool. Steam, accelerated into the Overall Pool by the Injector, promotes the water circulation and mixing until the Overall Pool decreasing is accelerated and the Injector outlet uncovered. The Overall Pool temperatures are shown in Figure 3.24.

Chapter 4

CATHARE Modeling of PERSEO facility

A complete assessment of the reliability and efficiency of the PERSEO innovative system requires a numerical analysis of the overall plant response to selected accidental scenarios. Industrial system codes like CATHARE are suitable to this purpose. Within the frame of the research program a benchmark approach has been adopted for the numerical analysis: detailed models of the PERSEO facility have been developed with the the last V2.5 mod8.1 version of CATHARE code and widely utilized for the design support and the pre-test analysis. Finally, the post-test analysis has allowed an accurate assessment of such models: verification of the set of closure relationships (heat transfer in condensation and pool boiling conditions, direct contact condensation etc.) and qualification of the nodalization [27].

4.1 The CATHARE model

The Figure 4.1 shows the CATHARE nodalization scheme of the PERSEO facility. In this configuration scheme, the 0D two-node module (volume) is chosen to represent the primary vessel, the HX collectors, the HX Pool lower and upper plenum and the Overall Pool (complete mixing). The volumes are interconnected by axial elements (pipe) representing the HX tube bundle, the water lines and the steam lines. Axial elements with cross-flow junctions are used to best simulate 2D recirculation within the HX Pool.

Empirical correlations specifically derived at atmospheric pressure are implemented in the code for this specific case study. The main correlations are *EPICE* correlation for boiling heat transfer in the HX Pool and *SUPERCLAUDIA* correlation for direct contact condensation in the Overall Pool [28]. The last correlation is implemented in order to

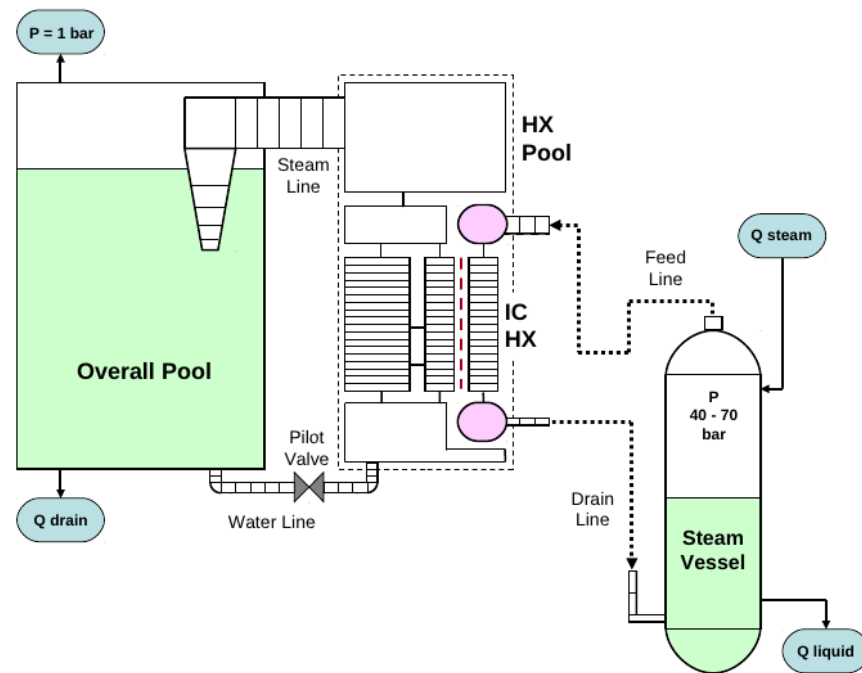


Figure 4.1: CATHARE nodalization scheme

overcome some deficiencies evidenced using CATHARE standard models and better reproduce the experimental data.

4.2 Analysis of the PERSEO Tests

A test campaign on the PERSEO facility has been conducted in order to verify the correctness of the proposal and the effectiveness of heat removal (section 3.3 explains in detail the PERSEO tests features). In the present work, the Test n.7 (Phase 1 and Phase 2) and the Test n.9 have been performed with CATHARE V2.5 mod8.1 and the results are compared with the experimental data for code validation purposes. In the comparison Figures shown in the next sections, the numerical and the measured values are reported with a different thickness line, the thicker lines represent the code results, while the thinner ones represent the test measurements.

4.2.1 Test n.7 - Phase 1

The Phase 1 of Test n.7 is aimed to verify the system behavior during start-up. In this phase, the system actuation with partial HX Pool fill-up without boiling conditions in the Overall Pool is performed. In section 3.3.1 a detailed explanation of the test n.7 is

Event	Time (s)
Beginning of the test	0
1 st partial triggering valve opening and closure	300-433
2 st partial triggering valve re-opening and re-closure	446-480
3 st partial triggering valve opening and closure	864-1085
Primary side depressurization	900-1400
End of the test	4609

Table 4.1: Chronology of main events of Phase 1

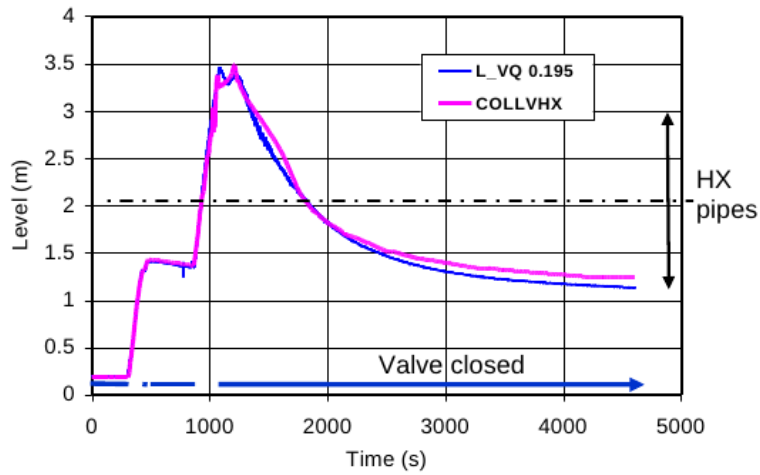


Figure 4.2: HX Pool collapsed water level

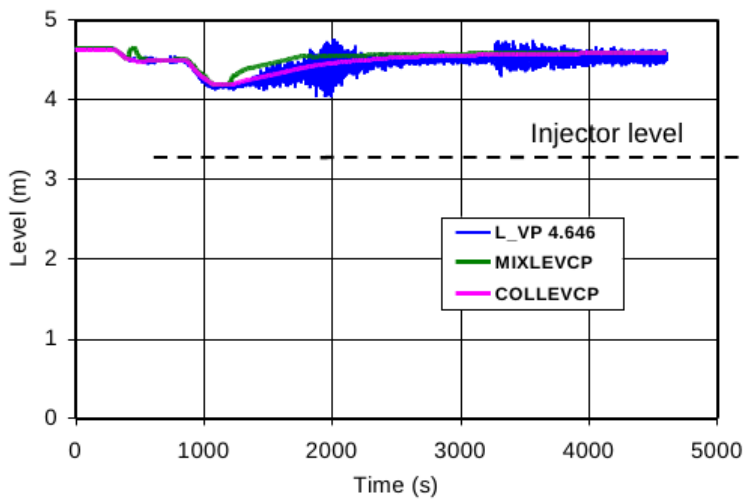


Figure 4.3: Overall Pool collapsed water level

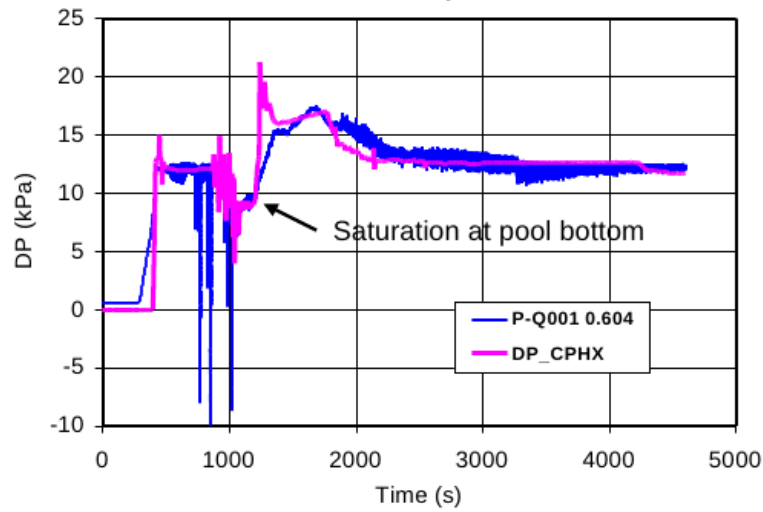


Figure 4.4: HX Pool relative pressure

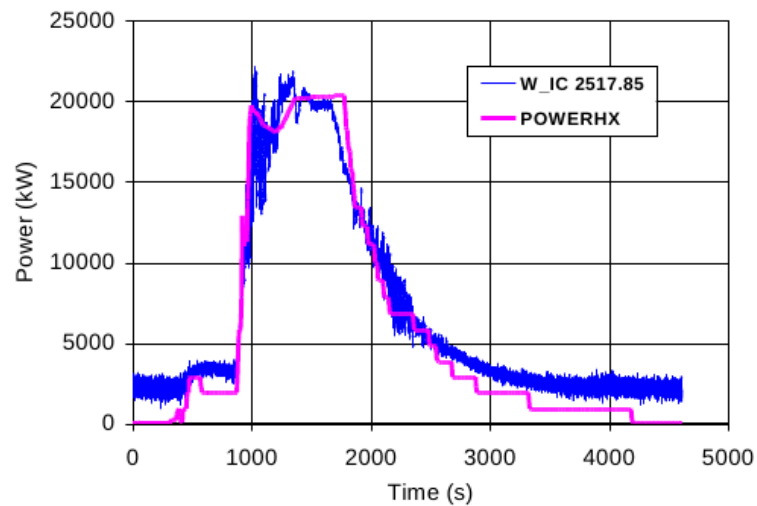


Figure 4.5: HX exchanged power

described. Table 4.1 shows the chronology of main events.

The comparison between the experimental results and the calculated ones is shown from Figure 4.2 to Figure 4.7.

Water Level behavior. After partial triggering valve openings, the HX Pool water level increases producing a corresponding decrease of the Overall Pool level according to the pool area. As soon as the HX tubes are covered by water (after about 900 s from

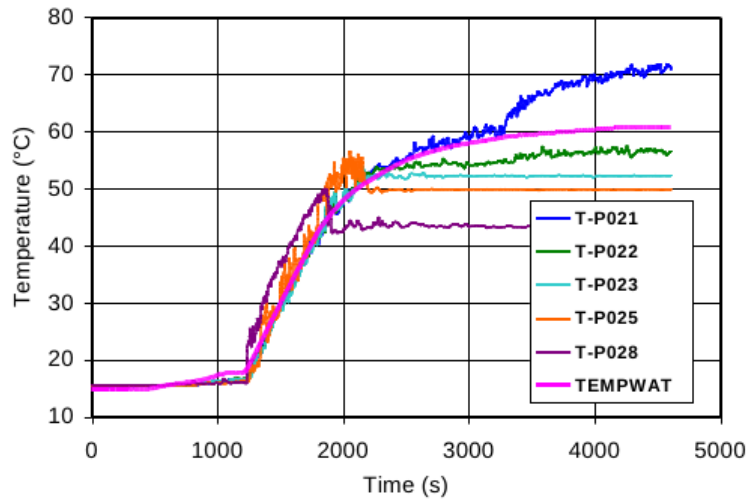


Figure 4.6: Overall Pool temperatures

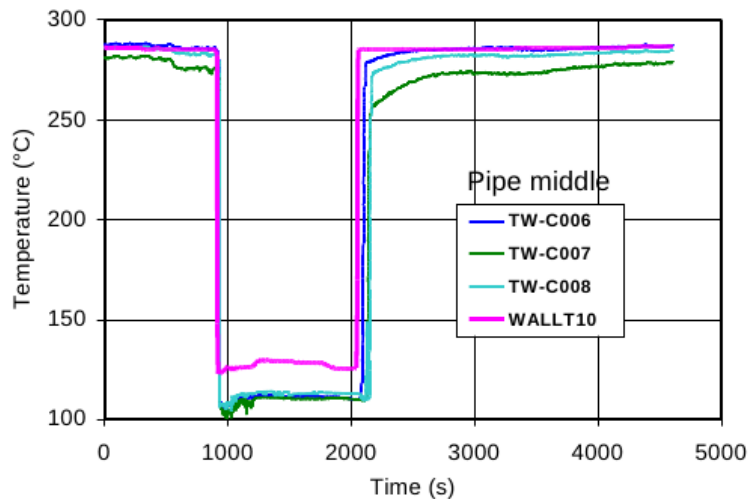


Figure 4.7: HX tube wall temperatures

the beginning of the transient), the power exchange becomes more significant leading to HX pool boiling conditions. The steam produced flows to the Overall Pool through the steam duct and the injector, with consequent Overall Pool water temperature progressive increase. At time $t = 1085$ s the triggering valve is closed and the HX water level decreases. Moreover, a temperature stratification phenomena is observed in the Overall Pool. Unless of a small underestimation of level decrease in the second part of the transient, the HX collapsed and the Overall Pool water level are well predicted by the code (Figure 4.2 and Figure 4.3). Oscillations of the Overall Pool level observed in

the test, produced by free surface fluctuations, cannot be taken into account by the code.

Relative Pressure and Power profiles. The injector differential pressure calibration allows a good representation of the HX Pool relative pressure (Figure 4.4). At the beginning of the test, the injector is full of water and the HX relative pressure respect to the Overall Pool pressure, is close to zero. Around $t = 400\text{ s}$ the injector empties and the HX relative pressure stabilizes at 12 kPa according to the Overall Pool water level. The largest discrepancy is observed at $t = 1200\text{ s}$, when the saturation conditions are reached at the HX pool bottom, due to water recirculation. As result, the sudden vaporization calculated at the bottom shows a pressure peak in the pool, steam duct and through the injector, since the triggering valve is closed. On the other hand, the experimental results shows that the transition to boiling at the HX Pool bottom is more smooth respect to the numerical results and the peak pressure is not observed. The 2 kPa deviation around $t = 2000\text{ s}$ is in accordance with the extracted power underestimation, leading to a reduced steam flowrate through the injector during the same period of time ($t = 1800 - 2200\text{ s}$). At the end of the test, the injector is full of saturated steam and the differential pressure of 12.4 kPa equals the hydraulic head of the water column between the injection level and the pool free surface. The Overall Pool level, which increases after triggering valve closure at $t = 1085\text{ s}$ due to water thermal expansion, is well predicted by the code. As a consequence, the HX Pool relative pressure is well predicted too. The power extracted by the HX, reaching a maximum of about 20 MW when the HX tubes are fully submerged by water-steam mixture, is well simulated (Figure 4.5) and the temporary power reduction during primary side depressurization between $t = 900 - 1400\text{ s}$ is captured.

Temperature profiles. Figure 4.6 shows that the mean Overall Pool temperature increase is well predicted by the code, while there is a large gap in the temperature stratification calculation. The HX pool Temperature at the middle plane of HX tube bundle is well simulated as shown in Figure 4.7. Under the wet side, the external wall temperature of HX tubes is over predicted (about 20°C over the experimental data). However, this discrepancy is probably caused by uncertainties in the thermocouple measurements.

4.2.2 Test n.7 - Phase 2

The Phase 2 of Test n.7 is aimed to verify the correct system behavior during long term accidental transient. In this phase, the system actuation with total HX Pool fill-up and the boiling conditions reached in the Overall Pool are performed. The chronology of

Event	Time (s)
Beginning of the test	0
Triggering valve opening	300 (opened in 26 s)
Overall Pool water discharge opening	1150
Onset of the Overall Pool water boiling	1400
Overall Pool water discharge closure	3230
Triggering valve closure	3338 (closed in 123 s)
Primary side depressurization beginning for end of test	4685
End of the test	5736

Table 4.2: Chronology of main events of Phase 2

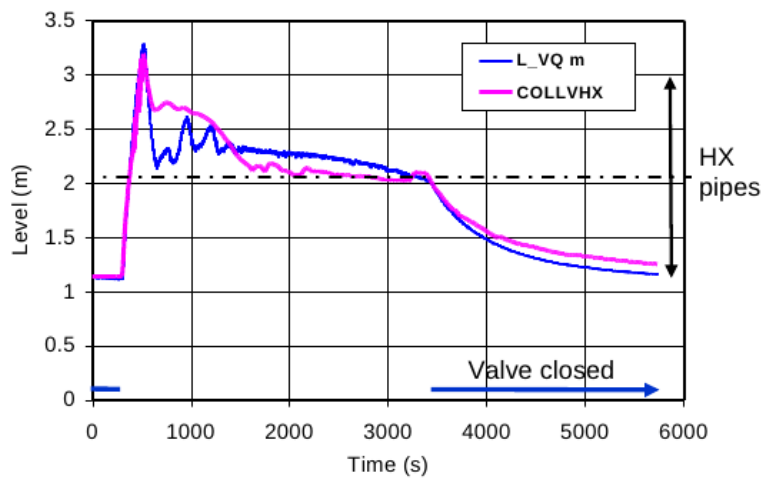


Figure 4.8: HX Pool collapsed water level

the main events (better described in section 3.3.1) is shown in Table 4.2.

The comparison between the experimental results and the calculated ones is shown from Figure 4.8 to Figure 4.13.

Water Level behavior. After full opening of the triggering valve at $t = 326$ s the water level in the HX Pool quickly increases. When boiling is reached in the pool at $t = 500$ s, the collapsed water level decreases, stabilizing around 0.25 m. In the Overall Pool, a progressive water level decrease begins at $t = 1150$ s by water discharge valve opening at the pool bottom. After 1400 s the Overall Pool reaches the boiling conditions and the water level decreases more quickly due to mass loss through the boil-off pipe. Around $t = 3400$ s the triggering valve is closed and the HX Pool level begins to rapidly decrease, until boiling is finished and the HX tube bundle is fully uncovered. The initial water level increase in the HX Pool is well captured by CATHARE (Figure 4.8). How-

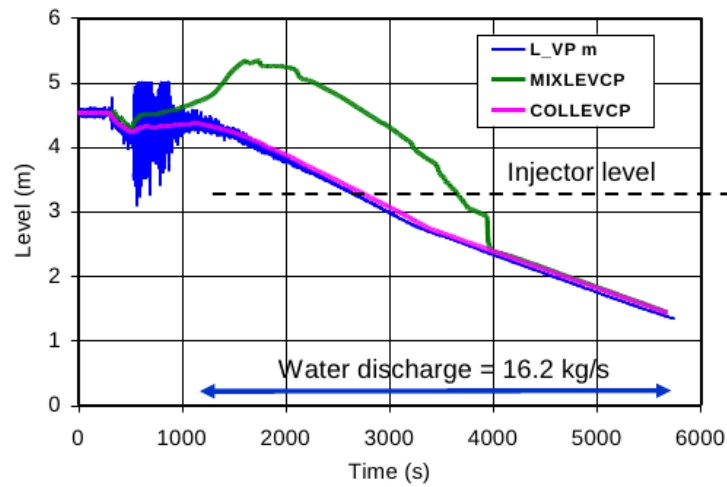


Figure 4.9: Overall Pool collapsed water level

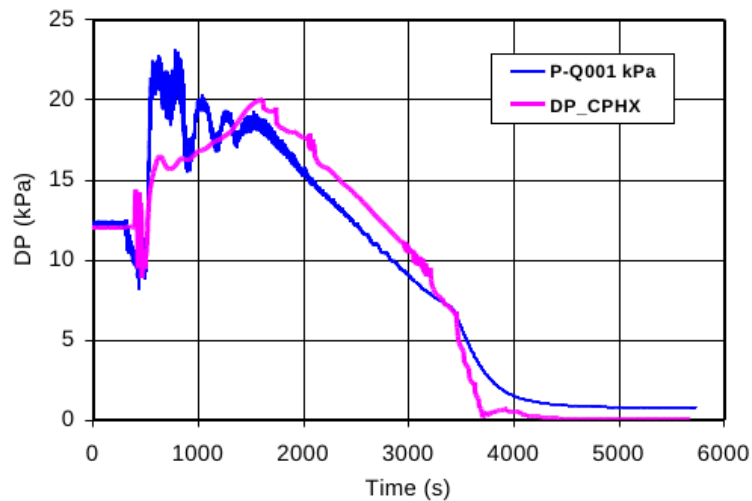


Figure 4.10: HX Pool relative pressure

ever the level is initially overestimated until $t = 1400$ s and then underestimated until triggering valve closure ($t = 3338$ s). Finally, at the end of the transient, the level is slightly overestimated. Large oscillations of the Overall Pool level are observed in the test after the steam injection at $t = 500$ s. These oscillations are produced by free surface fluctuations and cannot be reproduced by the 0-D module used to represent the Overall Pool (Figure 4.9).

Relative Pressure and Power profiles. Starting from the initial value of 12 kPa with water-empty injector, the HX Pool relative pressure decrease after triggering valve

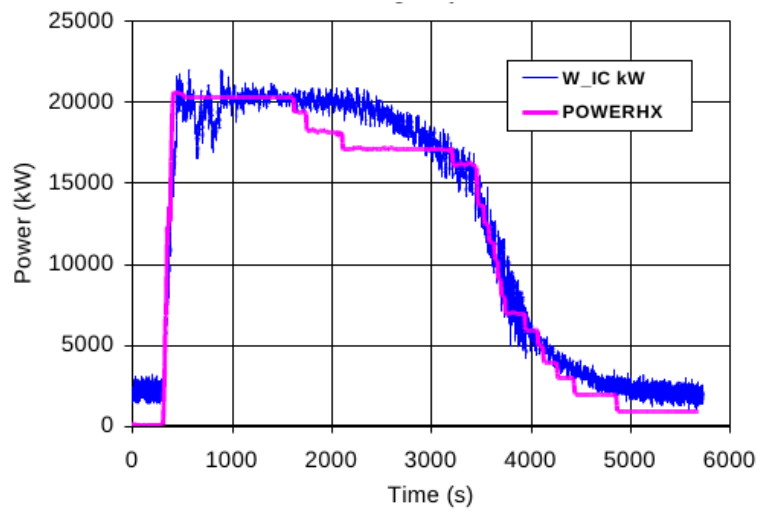


Figure 4.11: HX exchanged power

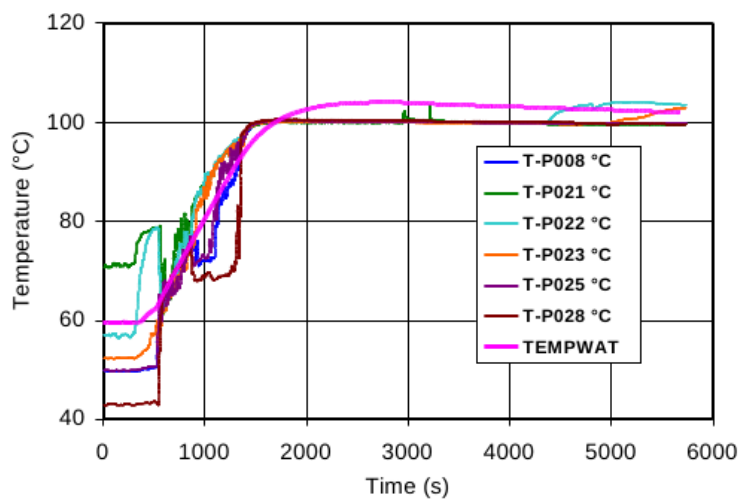


Figure 4.12: Overall Pool temperatures

opening at $t = 300 \text{ s}$ is roughly estimated (Figure 4.10). The large pressure underestimation after onset of HX Pool boiling, associated to Overall Pool level oscillations, produces the HX Pool level error shown in Figure 4.8 (time between $t = 500 - 1400 \text{ s}$). For the same reason, the relative pressure over prediction between $t = 1400 - 3200 \text{ s}$ causes the discrepancy in HX Pool level during the same period of time. The 20 MW power extracted by the HX is well predicted by the code until $t = 1600 \text{ s}$ (Figure 4.11).

Temperature profiles. Starting from temperature stratified phenomena reached at the

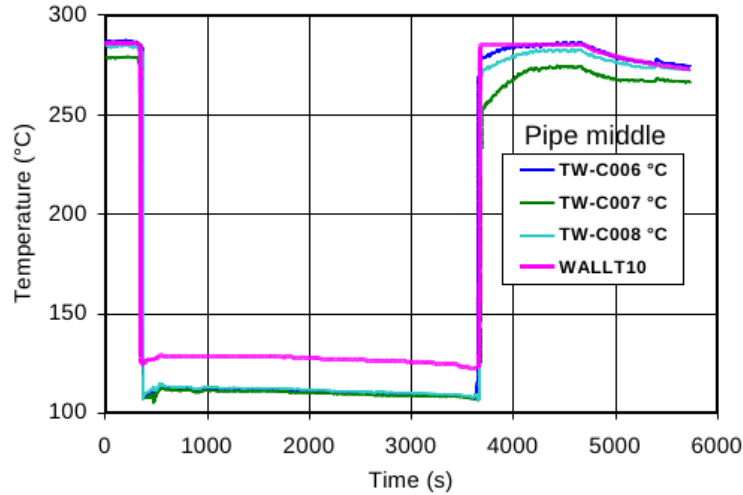


Figure 4.13: HX tube wall temperatures

end of Phase 1, the Overall Pool temperatures are mixed by the injector until onset of boiling (around 1600 s) (Figure 4.12). The calculated saturation temperature is higher than the measured value of 100°C at atmospheric pressure, since the Overall Pool pressure and corresponding saturation temperature are calculated by CATHARE at the middle of water pool height, where the pressure is up to 20 kPa above the atmospheric value. HX Temperature at the middle tube plane is very well predicted by the code (Figure 4.13). Furthermore, the same discrepancy is verified in the calculation of external wall temperature of HX tubes.

4.2.3 Test n.9

The Test n.9 provides the system actuation with total HX Pool fill-up and the reaching of boiling conditions in the Overall Pool. This test is performed to verify the correct system behavior during long term accidental transient under reduced primary pressure (4 MPa). The chronology of main events is shown in Table 4.3. The comparison between the experimental results and the calculated ones is shown from Figure 4.14 to Figure 4.19.

Water Level behavior. After full opening of the triggering valve at $t = 163\text{ s}$ the collapsed water level in the HX Pool quickly increases stabilizing close to the top of the tube bundle. The progressive decrease of the Overall Pool level is started by water discharge from the bottom at $t = 2790\text{ s}$. The water discharge valve is closed at $t = 4840\text{ s}$. From this time, the Overall Pool level decrease is terminated and the extracted power tends to zero according to the full uncover of HX tube bundle reached at

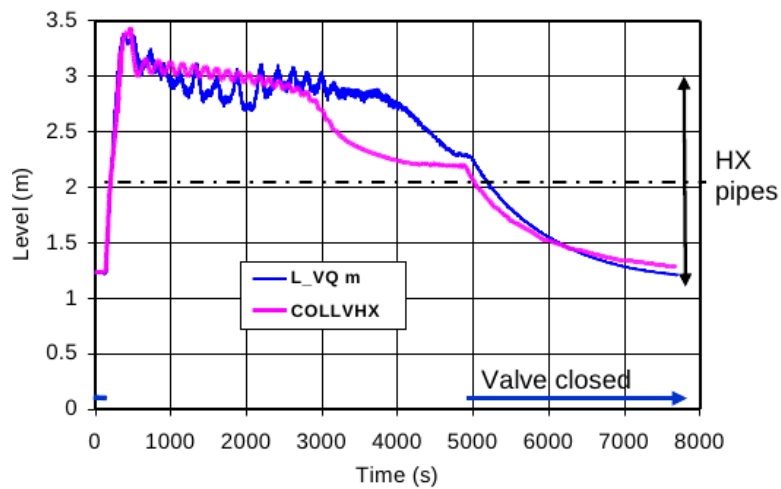


Figure 4.14: HX Pool collapsed water level

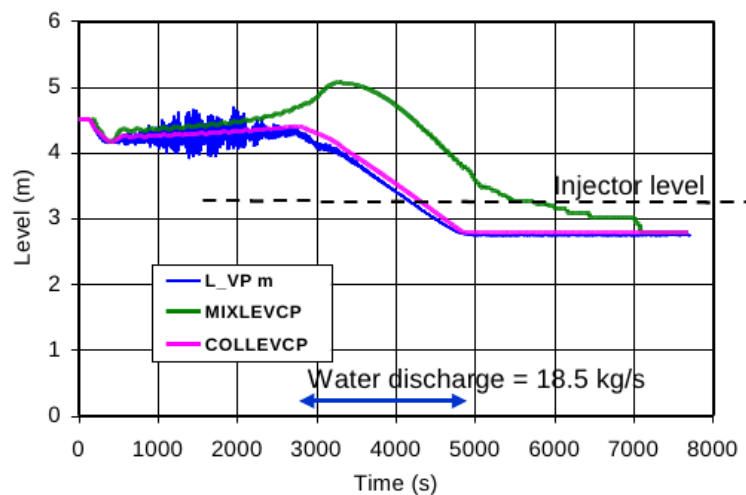


Figure 4.15: Overall Pool collapsed water level

the end of test. The initial water level increase in the HX Pool is very well captured by CATHARE (Figure 4.14), while the level is overestimated in the first part of the transient ($t = 900 - 2100$ s) and then largely underestimated from $t = 2900$ s until the triggering valve is closed. The decrease of the HX Pool level during the last phase of the transient is well reproduced until the end of the test. The Overall Pool collapsed water level behavior is well predicted by CATHARE during the whole transient (Figure 4.15). The oscillatory behavior observed in the test before Overall Pool water boiling might be produced by sudden steam condensation at the injector outlet, inducing fluctuations at the pool free surface.

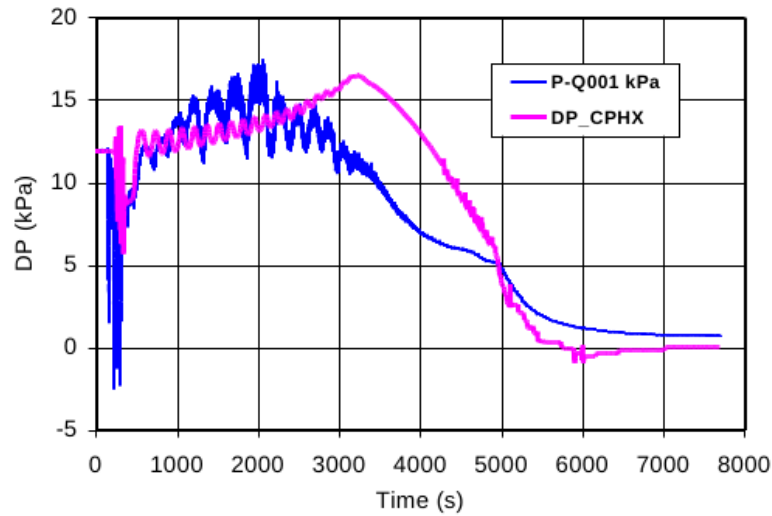


Figure 4.16: HX Pool relative pressure

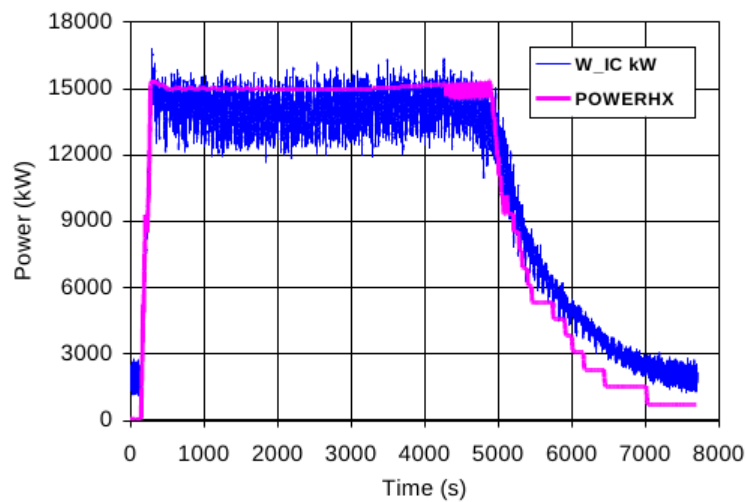


Figure 4.17: HX exchanged power

Relative Pressure and Power profiles. The HX Pool relative pressure overestimation between $t = 2700 - 5000$ s (see Figure 4.16) is consistent with the corresponding HX Pool level underestimation. The calculated extracted power in Figure 4.17 is 15 MW, slightly higher than the measured one (14 MW). The power diminution predicted by the code after triggering valve closure at about $t = 5000$ s is slightly more accelerated than the one observed in the test.

Temperature profiles. The onset of boiling in the Overall Pool occurring around $t = 3200$ s is very well captured by the code (Figure 4.18). Figure 4.19 shows the HX Tem-

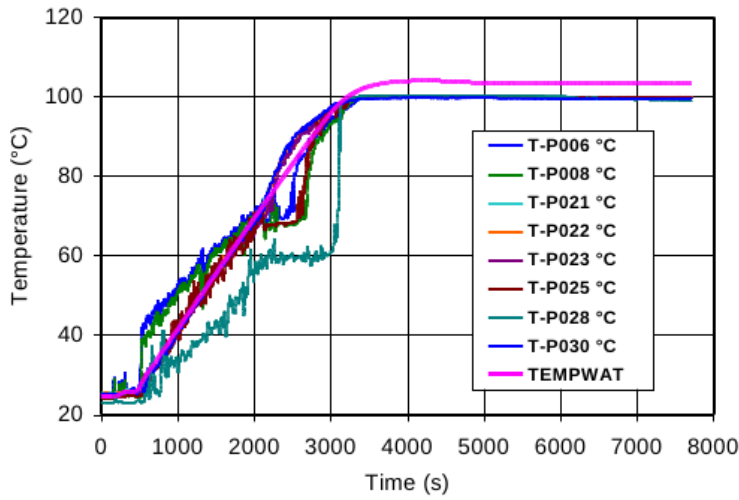


Figure 4.18: Overall Pool temperatures

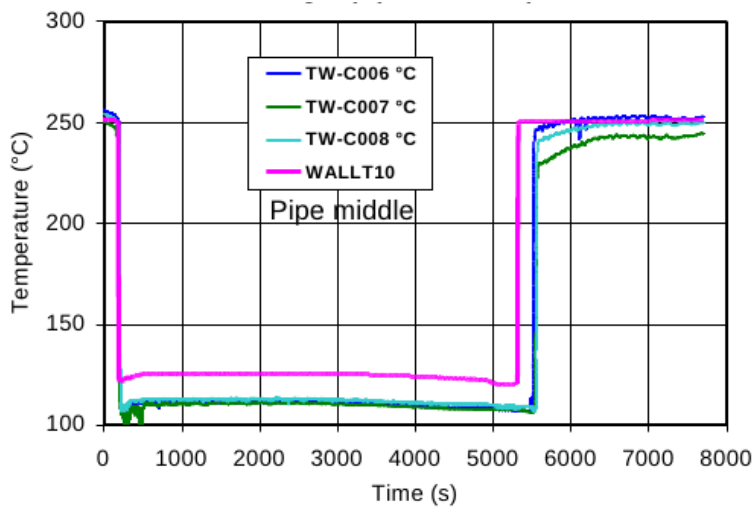


Figure 4.19: HX tube wall temperatures

perature profile. Once more, the HX tube wall temperature is over predicted.

4.3 3D Overall Pool modeling

In the previous section, the results obtained shown the general capability of CATHARE to evaluate main natural circulation and heat transfer phenomena occurring during the PERSEO tests. Apart from temperature stratification and free level oscillation effects in the Overall Pool, discrepancies have been found in the calculation of the HX Pool rela-

Event	Time (s)
Beginning of the test	0
Triggering valve opening	142 (opened in 21 s)
Overall Pool water discharge opening	2790
Onset of the Overall Pool water boiling	3200
Overall Pool water discharge closure	4840
Triggering valve closure	4887 (closed in 93 s)
End of the test	7708

Table 4.3: Chronology of main events of test 9

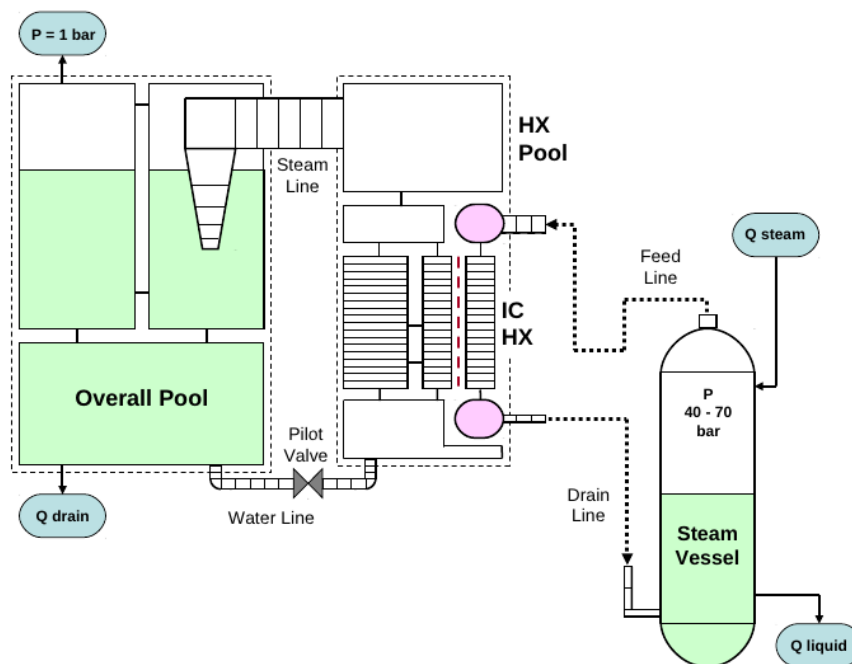


Figure 4.20: 3D volume Overall Pool modeling scheme

tive pressure and collapsed water level behavior, after boiling is reached in the Overall Pool. The HX Pool relative pressure against the Overall Pool pressure (atmospheric value) strongly depends on the hydraulic head of the water column above the steam injector outlet in the Overall Pool. This hydraulic head increases under Overall Pool boiling conditions depending on void formation in the pool and swollen level effect (see Figure 4.9 and Figure 4.15). Likely this swollen level effect is overestimated by the 0D module of CATHARE representing the Overall Pool, because of homogeneous distribution of voids considered in the boiling water pool, which could be in contrast with non uniform radial and axial distribution of voids expected in the tests. The use of a

3D volume Overall Pool modeling has been evaluated in this study in order to verify the Overall Pool swollen level effect and try to reduce the discrepancies with the test measurements. The implementation of the new Overall Pool modeling in the original nodalization scheme is shown in Figure 4.20. The height of the Overall Pool bottom volume is different for the two tests according to the respective extracted power value and then different boiling rate within the Overall Pool.

The Phase 2 of the Test n. 7 and the Test 9 in which boiling conditions are reached in the Overall Pool have been recalculated with the new modeling and the obtained results are presented in the following sections.

4.3.1 Test n.7 - Phase2

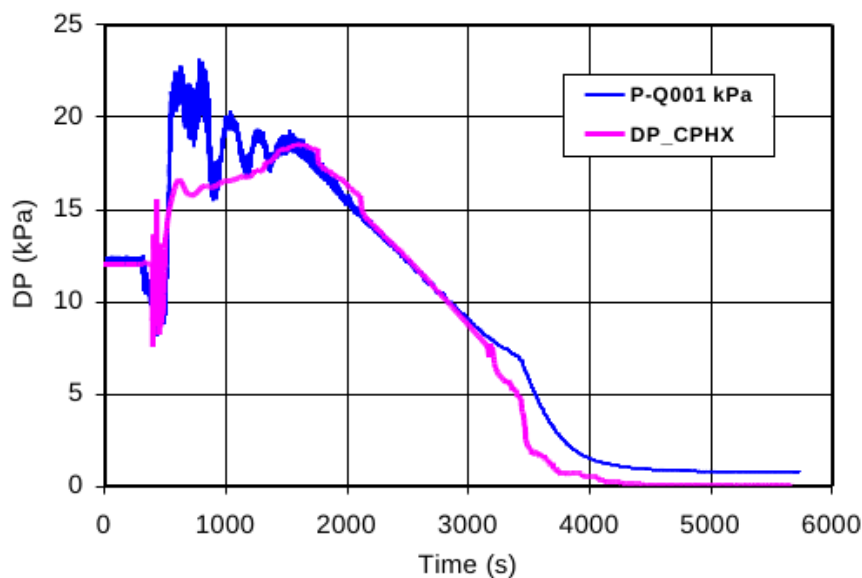


Figure 4.21: HX Pool relative pressure

The new code results for the Phase 2 of Test n.7 regarding the HX Pool relative pressure, the water level in the two pools and the HX exchanged power are shown from Figure 4.21 to Figure 4.23 in comparison with the test measurements. As expected, the differences with previous results become significant only after the onset of Overall Pool boiling around $t = 1400s$. After this time, the deviations from the experimental trend are in general reduced, allowing the best simulation of all phenomena concerned in the test.

The HX Pool relative pressure is very well predicted after the onset of boiling (Figure 4.21). The reduced pressure value reflects in a more accurate evaluation of the HX

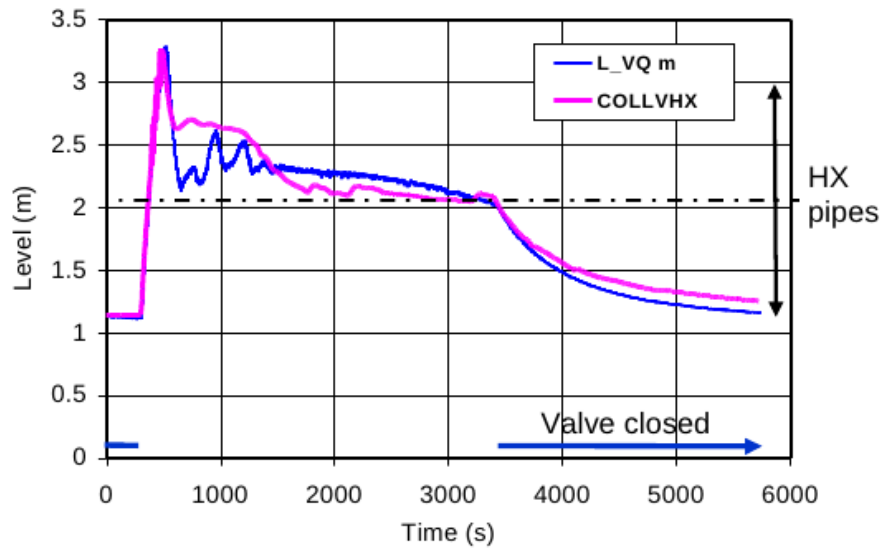


Figure 4.22: HX Pool collapsed water level

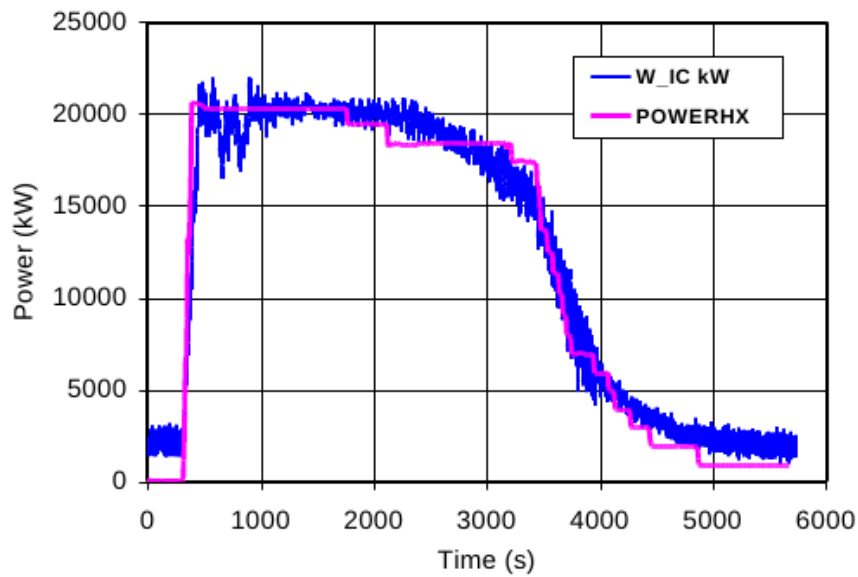


Figure 4.23: HX exchanged power

Pool collapsed level which slightly increases in better agreement with the test measurement (Figure 4.22). Moreover, the small HX Pool level difference better predict the exchanged power diminution curve observed in the test (Figure 4.23) during the Overall Pool level decreasing phase. In the time $t = 1600 - 3500s$, due to a greater HX power with corresponding increase of Overall Pool boiling rate, the recalculated Overall Pool collapsed water level is very similar to the measure one (Figure 4.24).

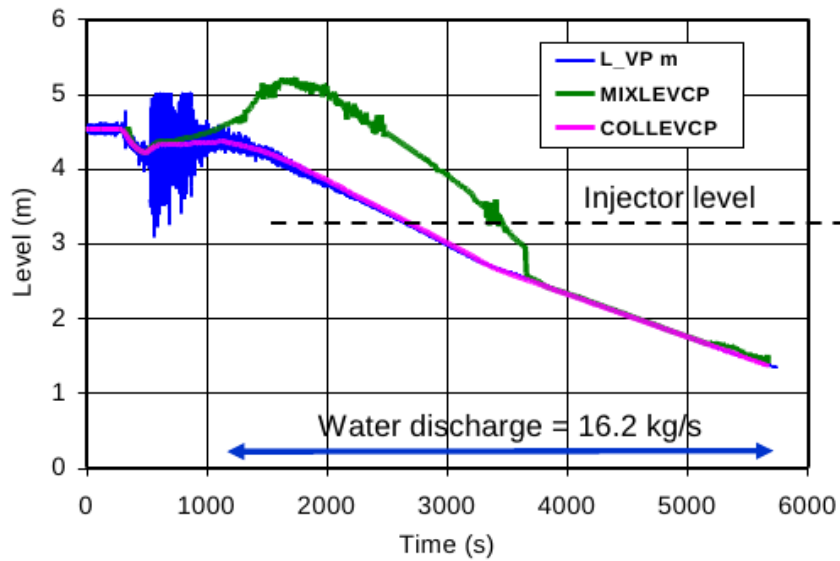


Figure 4.24: Overall Pool collapsed water level

4.3.2 Test n.9

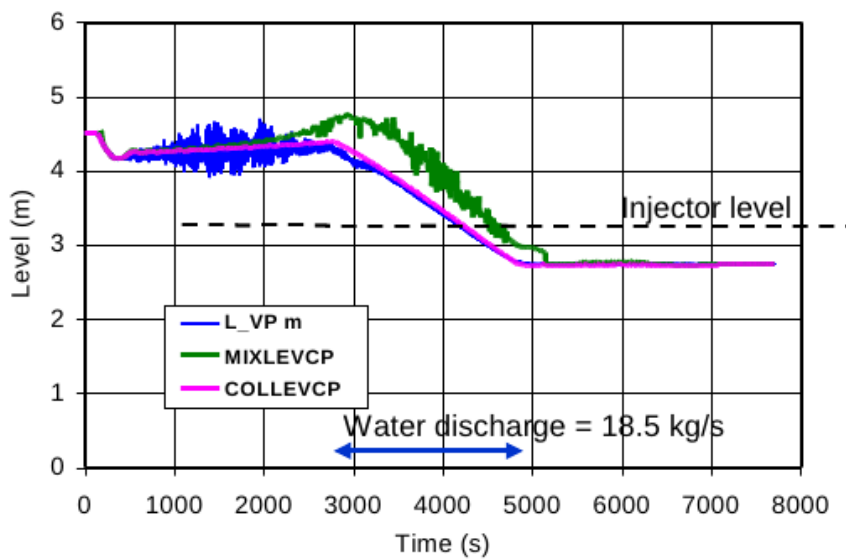


Figure 4.25: Overall Pool collapsed water level

The new code results for the Test n.9 regarding the water level in the two pools, the HX Pool relative pressure and the HX exchanged power are shown from Figure 4.25 to Figure 4.28 in comparison with the test measurements.

As expected, the differences with previous results become significant only after on-

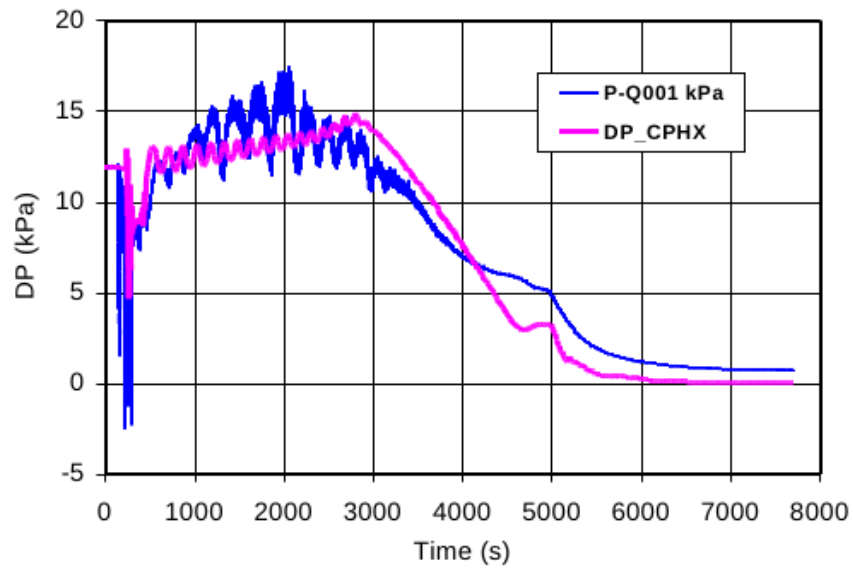


Figure 4.26: HX Pool relative pressure

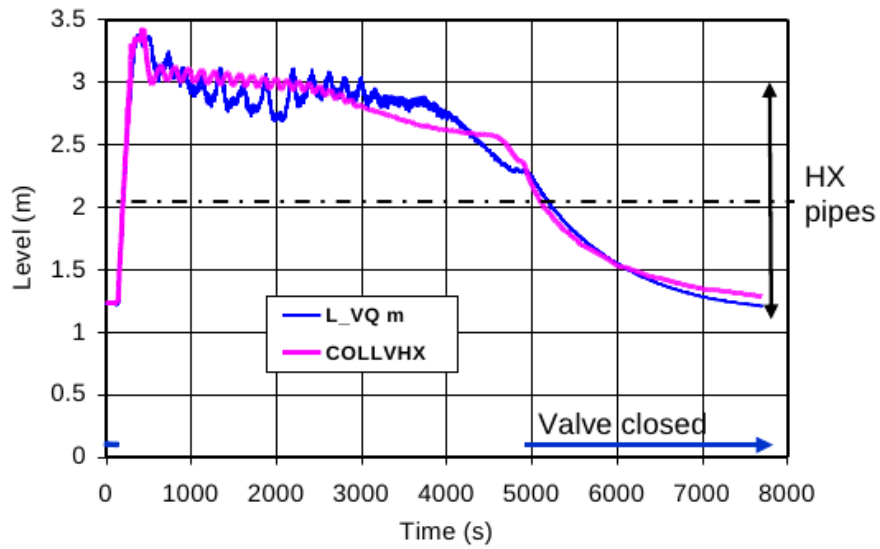


Figure 4.27: HX Pool collapsed water level

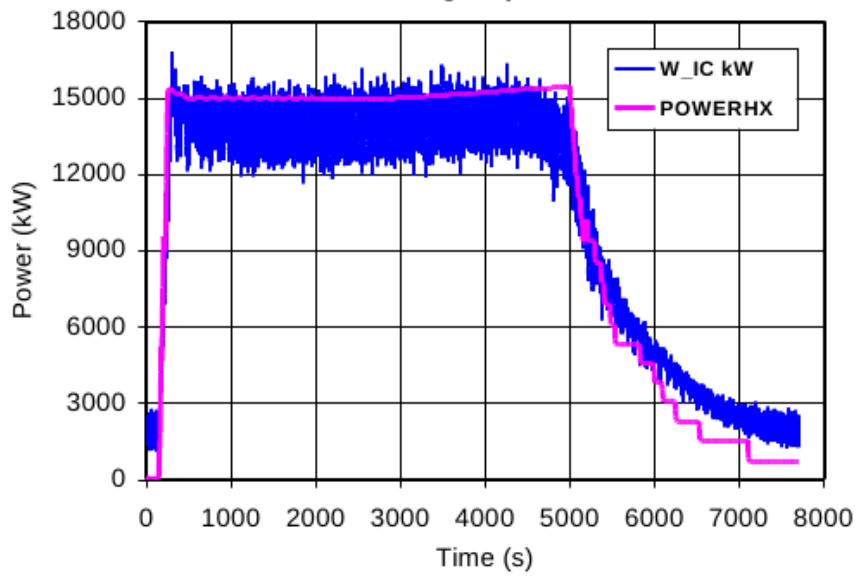


Figure 4.28: HX exchanged power

set of Overall Pool water boiling around $t = 3200$ s. After this time, due to significant reduction of the calculated Overall Pool swollen level (Figure 4.25), the HX Pool relative pressure is much better predicted (Figure 4.26). Moreover, the right pressure trend reflects in more accurate calculation of the HX Pool collapsed level (Figure 4.27). No significant changes are shown in the HX exchanged power (Figure 4.28).

Chapter 5

NEPTUNE_CFD modeling of PERSEO facility components

5.1 Introduction

In the previous chapter, the CATHARE code has been employed for the analysis of two main tests of the PERSEO facility. This system code does not reproduce a detailed simulation of a specific component. Therefore a CFD simulation of this component by means of the NEPTUNE CFD code has been performed in order to analyze carefully the system transient in the Overall Pool and in the injector. This should allow us to give an evaluation of the non-homogeneous distribution of the void fraction in the pool.

In the next sections, a two dimensional model of the overall pool and the injector (also called OP-injector system) and the results as well obtained by the simulations will be analyzed. Then, a three dimensional model of the components will be presented. All the simulations are obtained considering the test n.9 of the PERSEO tests (in section 3.3.2 this test is analyzed in detail).

5.2 CATHARE-NEPTUNE coupled simulation

A simple scheme of OP-injector system and the coupling with CATHARE results is shown in Figure 5.1. The water discharge (WD) is a line that allows water removal in order to accelerate the decrease of the water level in the Overall Pool. The water-to-HX-pool line (WL) is the feed line that joins the Overall Pool to the HX pool. The steam line allows the steam to flow from the HX pool to the injector, while both steam and air flow out the system through the boil-off section.

In order to analyze the Overall pool and the injector of the PERSEO facility, it is necessary to impose specific boundary conditions of the case study. To do this, a weak

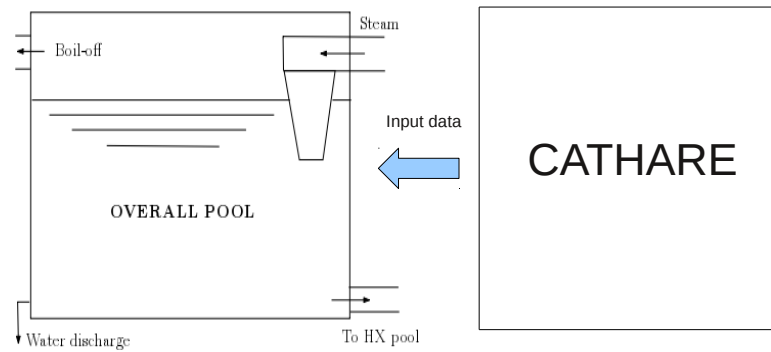


Figure 5.1: Coupling CATHARE-NEPTUNE

coupling between CATHARE code and NEPTUNE_CFD code is performed. This coupling allows first the solution of the CATHARE code over all the domain and then the solution of the overall pool and injector components with the NEPTUNE_CFD code using the previously results obtained as boundary conditions. The boundary conditions required for the weak coupling between the OP-injector system and the rest of the PERSEO facility are the mass flow rates through the water discharge and the water-to-HX-pool lines. Atmospheric pressure is imposed at the boil-off section for the outgoing gas flow while at the inlet section of the injector both temperatures and mass flowrate (or steam velocity) are required. The boundary velocities for the NEPTUNE_CFD code can be computed from the mass flowrate predicted by the CATHARE code. Since the state variables in CATHARE are 1D along the axis, uniform fields across each boundary section have been considered.

The aim of this simulation is to reproduce the correct temperature behavior from PERSEO test 9. Figure 5.2 shows the layout of the overall pool temperature measurement positions while the experimental results are reported in Figure 5.3. The computed temperatures at the probe positions denoted by TP6, TP8, TP23 and TP25 are chosen for this case study and are listed in the *Input-Output-Control* module. The exact location of the probes can be found in Table 5.1.

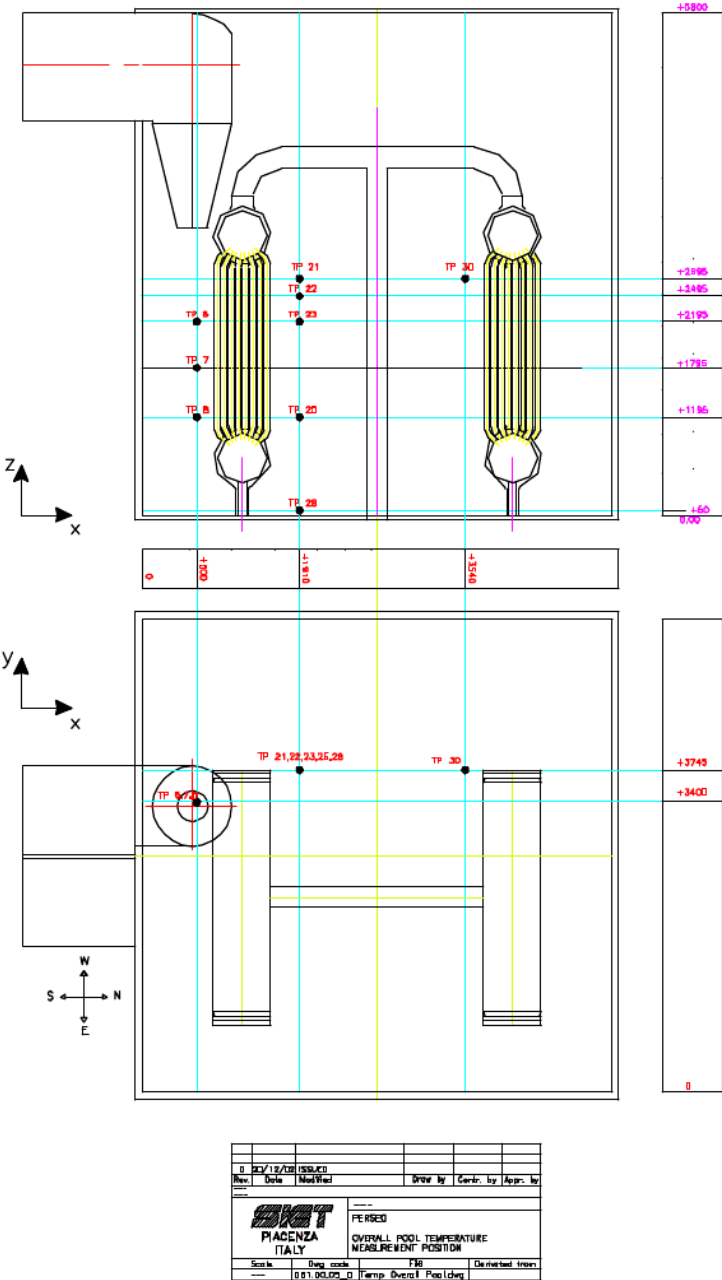


Figure 5.2: Overall pool temperature measurement positions.

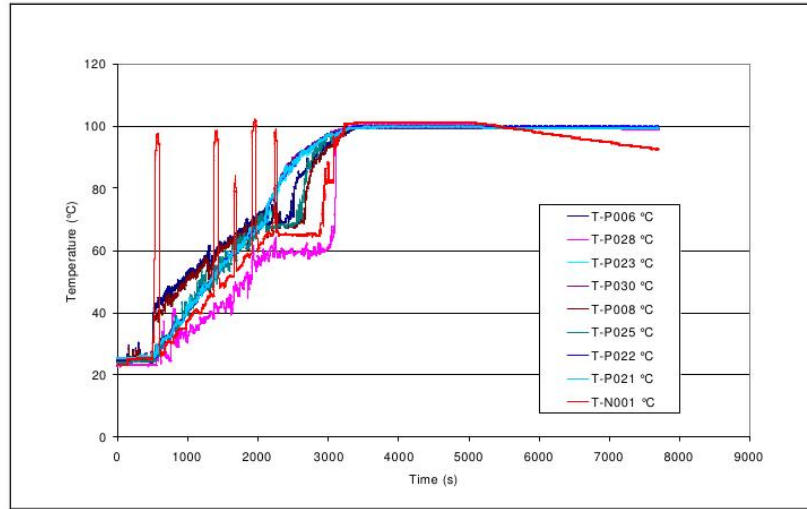


Figure 5.3: Overall pool temperatures for different probes.

Position	X	Y	Z	Code
Overall pool under the Injector	500	3400	2195	TP006
Overall pool under the Injector	500	3400	1795	TP007
Overall pool under the Injector	500	3400	1195	TP008
Overall pool central area	1910	3745	2695	TP021
Overall pool central area	1910	3745	2195	TP023
Overall pool central area	1910	3745	1195	TP025
Overall pool central area	1910	3745	50	TP028
Overall pool central area	3540	3745	2695	TP030
Overall pool central area	1910	3745	2495	TP022

Table 5.1: Exact locations (in *mm*) of the probes for temperature measurements with respect to the reference frame indicated in Figure 5.2.

5.3 The two-dimensional model

5.3.1 Geometry and Boundary conditions for the Test 9

The two dimensional geometry and mesh modeling of the OP-injector system are shown in Figure 5.4. The mesh consists of three-dimensional hexahedral cells with unitary thickness and is refined near the injector outlet. The water-to-HX-pool line and the water discharge line are considered as an unique line. The injector is positioned outside the pool to simplify the simulation [30]. As described in the previously section, the boundary conditions for the NEPTUNE code are obtained from the CATHARE solution (Figures 5.5 and 5.6). In particular, Figure 5.5 shows the steam mass flowrate

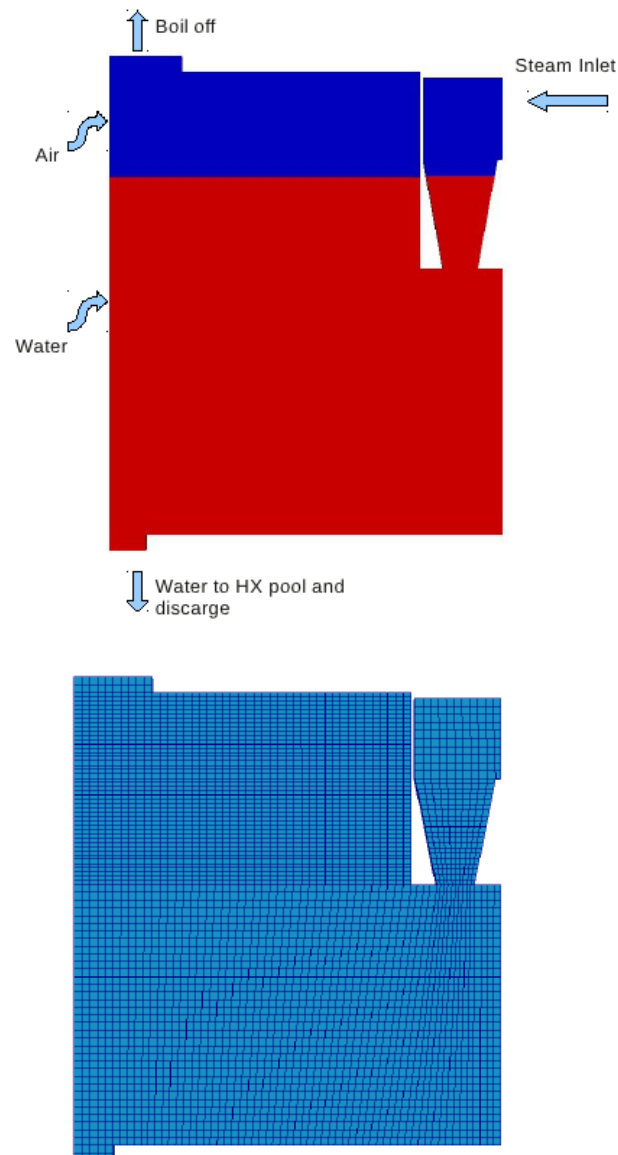


Figure 5.4: 2D geometry and mesh of OP-injector system

through the main duct connecting the HX to the OP pool. On the right of Figure 5.6 the CATHARE solution for the mass flowrate through the water discharge (WD) line is reported. This line allows a faster water removal to accelerate the decrease of the water level in the OP pool. On the left of the same figure the mass flowrate of water from the overall pool to the water-to-HX-pool (WL) line is presented.

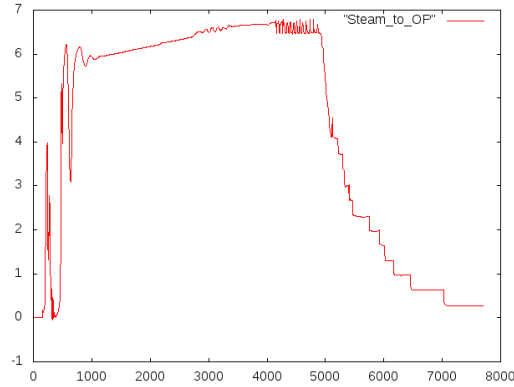


Figure 5.5: Steam Mass flowrate to OP pool

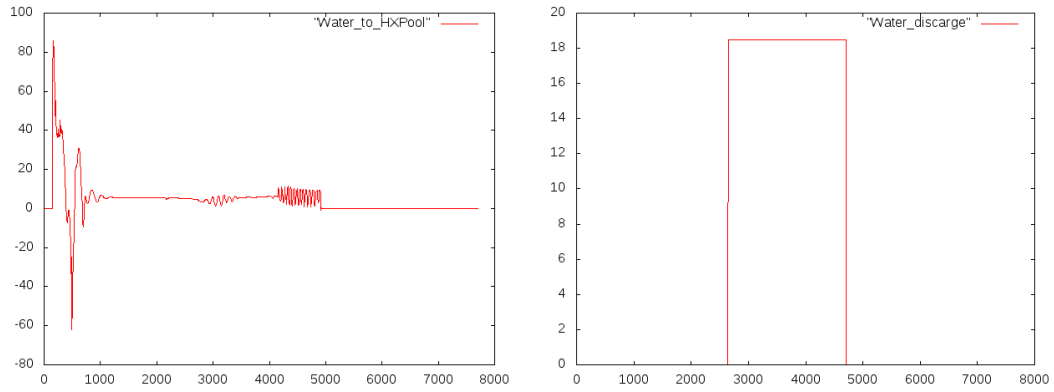


Figure 5.6: Water Mass flowrate to HX pool (left) and water discharge Mass flowrate (right)

5.3.2 Physical properties and models set in the `param` file

The `param` file

Fluid	T (K)	$\rho(Kg/m^3)$	$\mu(Pa s)$	$C_p(W/m^3 K)$
steam	297.75	Cathare table	Cathare table	Cathare table
water	297.75	Cathare table	Cathare table	Cathare table
air	gas law	2	2×10^{-5}	1006

Table 5.2: Fluid and flow properties selected for PERSEO test 9

The `param` file is the dataset file in which physical properties, models and boundary conditions are imposed to the case study (section 2.3.2 gives a detail description the file). As shown in Figure 5.4 in the OP-injector system three fluids are present: water,

steam and air. The main physical properties of the fluids are reported in Table 5.2. In this simulation the special module *water/steam* which allows the use of Cathare table for water/steam systems is enable.

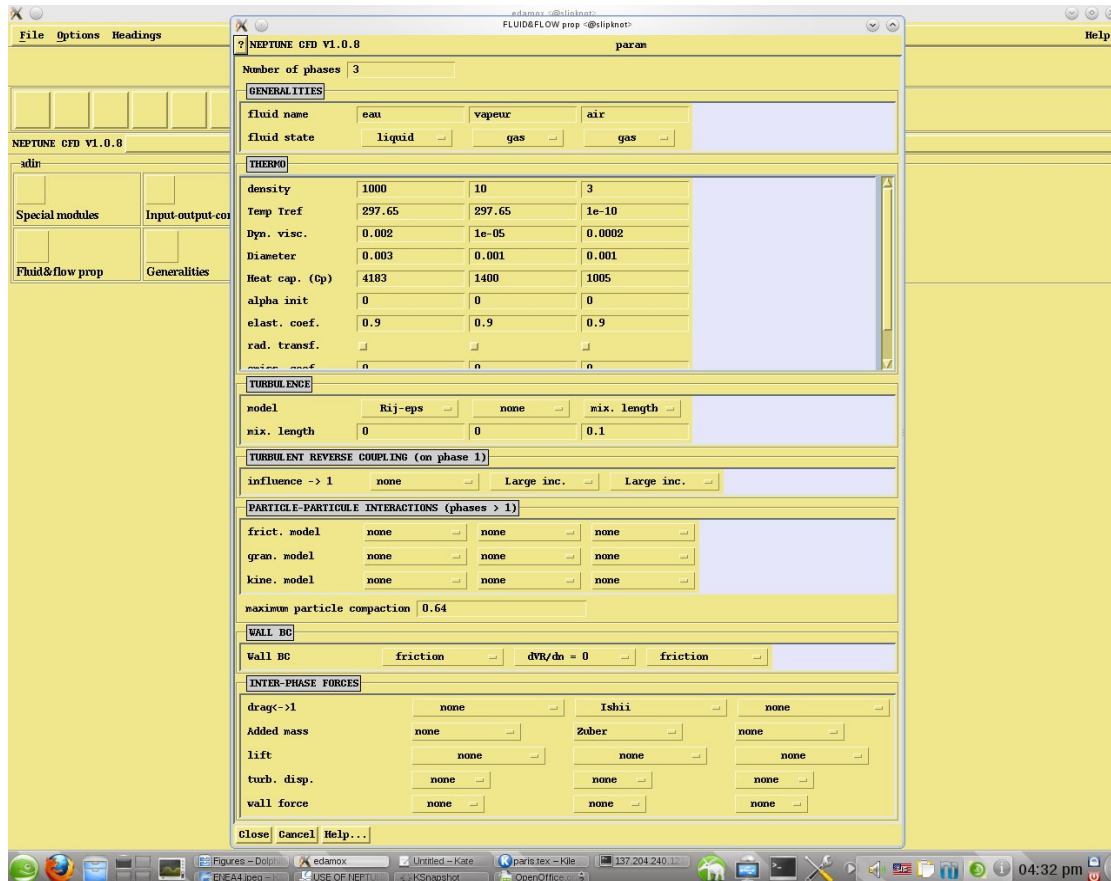


Figure 5.7: Physical properties.

The label “Cathare table” refers to an internal database that correlates pressure and temperature of water and steam to other physical properties. The reference (and initial) pressure is set to $p = 1 \text{ atm}$.

Figure 5.7 shows the *Fluid and flow properties* module of the `param` file for this specific test case. The turbulence model in water is the *Rij – model* recommended by NEPTUNE. Mixing length model for air is set, while no turbulence model is set in the steam component. The *Separated Phases* drag model and the *Large interface* model have been used for steam/water and air/water interactions, respectively. Simple source terms for enthalpy and momentum between air and steam have to be included in order to prevent these quantities to diverge during the calculation in the regions where each phase

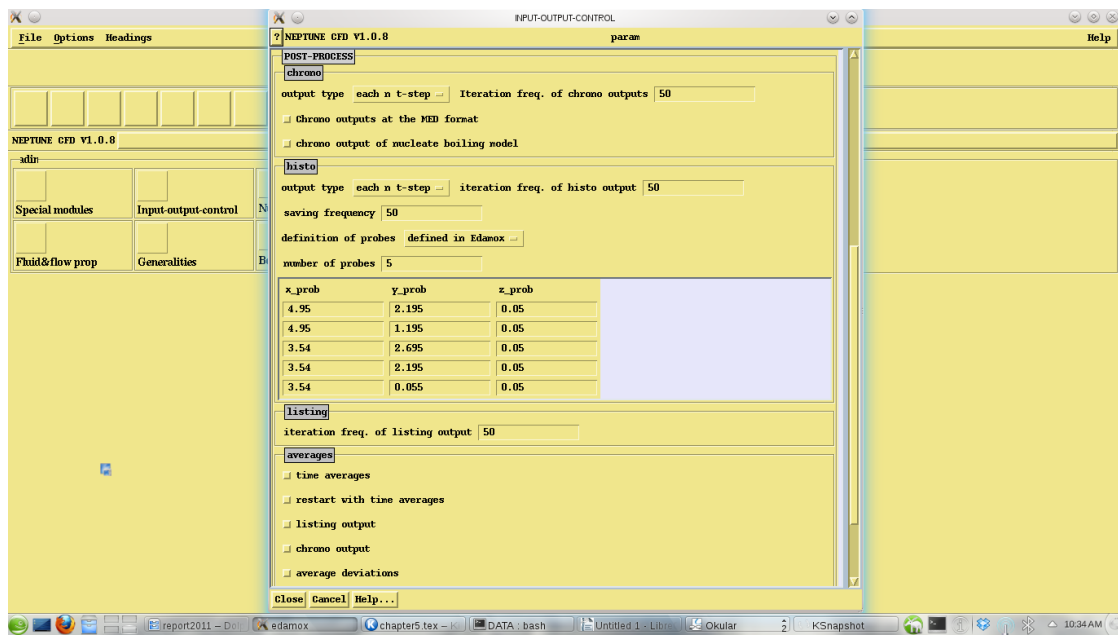


Figure 5.8: Input-Output control

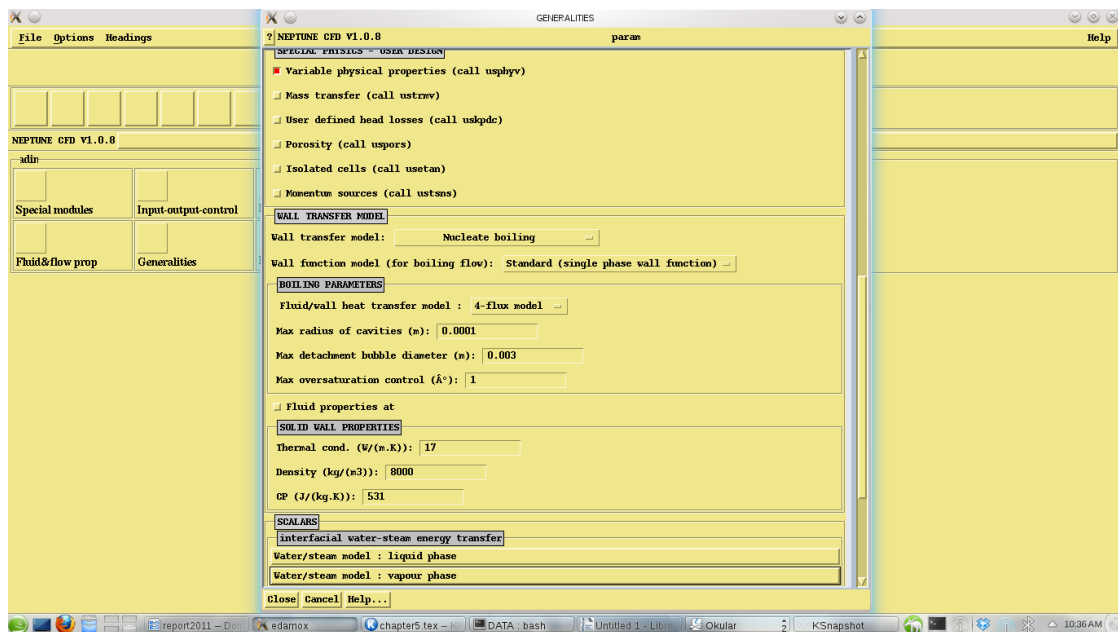


Figure 5.9: Physical models

was only present with small traces. Actually, the numerical method allows a phase to appear below a given tolerance even where they are not physically expected to be. The conserved quantities of these “spurious phases” must be kept under control through

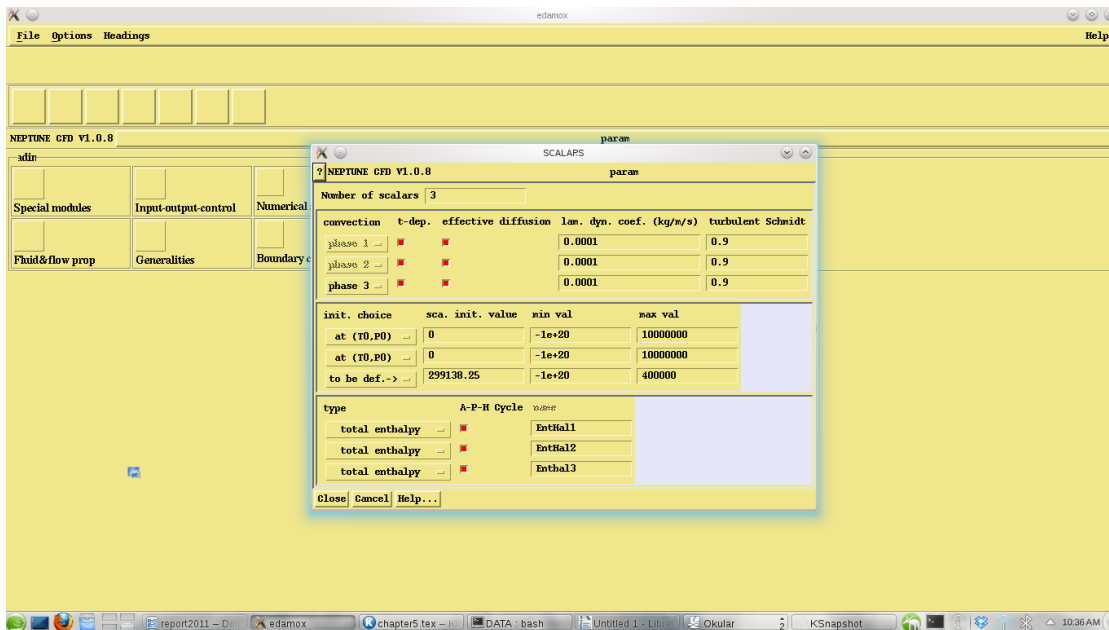


Figure 5.10: Scalars

proper source terms in order to prevent the calculation from diverging. To consider these source terms, the user defined routines `usth12.F` and `ustsns.F` are adjoint in the simulation (for a detail description, see the next section). On the wall, friction boundary conditions for water and air and zero velocity normal derivative for steam are used. The Ishii drag model and the Zuber added masses model for the steam phase are used.

In Figure 5.8 is shown the *Input-Output-Control* module. Here the mesh, the post-processing saving frequency and the probes location are set.

In the *Generalities* module, shown in Figure 5.9, the gravity force is set. The wall transfer model chosen is the Nucleate Boiling model with a standard wall function and the interfacial water-steam energy transfer model chosen is the Standard model both for the steam and the water.

Three scalars are set in the module shown in Figure 5.10: the total enthalpies for each fluid. Two of these are enable automatically when the *steam/water* module is selected in the *Special modules*: the total enthalpies for water and steam phases. The third scalar is adjoint to consider the air phase and the initial value of this scalar is defined as

$$H_{in3} = C_p * T_{in} \quad (5.1)$$

As shown in Figure 5.11 the boundary conditions consists of seven regions: steam in-

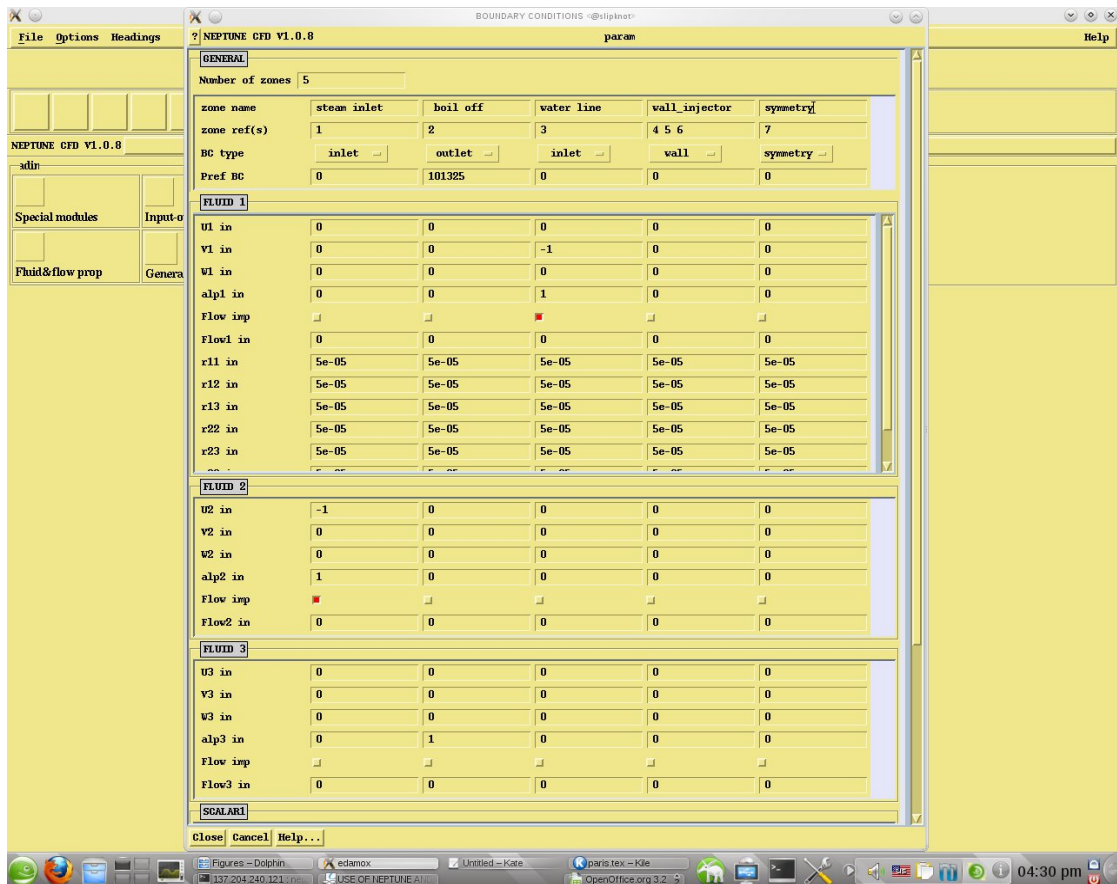


Figure 5.11: Boundary conditions.

let, boil-off, water line, injector wall, top pool wall, pool wall and symmetry boundary region. The names are self describing; the steam inlet is the inlet of the steam in the injector and the boil-off is the outlet boundary at the top of the pool. The injector wall, top pool wall and pool wall appear in Figure 5.11 as a unique column since all these regions can be considered as standard walls with the same kind of boundary conditions. The mesh is three-dimensional with unitary thickness. Since in finite volume discretization, fields are constant in the cell and located at the center of the cell. The symmetry boundary conditions are needed to simulate two-dimensional geometries with three-dimensional meshes. For details see [29]. On the steam inlet region only steam can enter with direction normal to the surface and mass flowrate is defined in the appropriate file (`uscLim.F` user routine) as a function of time by the previously solved CATHARE solution. The temperature condition is set to T_{Sat} option which denotes the saturation temperature at the corresponding pressure. The boil-off boundary condition is the standard outflow condition at atmospheric pressure for air while wa-

ter and steam are not allowed to exit. Concerning the water line boundary condition, temperature is fixed to reference Temperature and mass flow is imposed through the `usclim.F` user file as a function of time. At the wall, standard turbulent boundary conditions for water and air are imposed.

User routines

In this simulation some user files are modified by introducing specific subroutines.

Boundary conditions are imposed by using the CATHARE solution. In order to impose the boundary conditions as a function of time one must modify the file `usclim.F`. On the injector inlet boundary, the mass flow function $m(t)$ for phase 1 (steam) over the interval $t \in [1.43E + 02, 1.68E + 02]$ is given by

$$m(t) = \frac{-(-5952.98 + 74.3234t - 0.228571t^2)}{54.7}. \quad (5.2)$$

The FORTRAN language is the following:

```

      IF ( (TTCABS .GE. 1.43E+02)
&      .AND. (TTCABS .LT. 1.68E+02) ) THEN
          DEBCL (1, 2) = -FACT_W * ( -5952.98 + 74.3234 * TTCABS - 0.228571
&      * TTCABS * TTCABS )
      ENDIF

```

Here, $DEBCL(j, \alpha)$ is the mass flowrate on boundary j (steam inlet boundary is denoted by 1 in order) for phase α (steam is phase 2). Time is denoted in this file by `TTCABS`. The same procedure is used to set the steam boundary conditions on all the simulation time and the water boundary conditions in which the mass flowrate on boundary is denoted by $DEBCL(3, 1)$.

Initial conditions must be defined in the file `usiniv.F`. The water level in the Overall Pool is set by 4.5 m and above the water only air is present. The FORTRAN routine is the following:

```

      DO IEL = 1, NCEL
          IF (XYZCEN(1, IEL) .GT. 4.5 ) THEN
              RTP (IEL, IALPR(2)) = 1.D0
              RTP (IEL, IALPR(1)) = 0.D0
              RTP (IEL, IALPR(3)) = 0.D0
          ELSE

```

```

      RTP ( IEL, IALPR ( 1 ) ) = 1. D0
      RTP ( IEL, IALPR ( 2 ) ) = 0. D0
      RTP ( IEL, IALPR ( 3 ) ) = 0. D0
    ENDIF
  ENDDO

```

The $RTP(e, \alpha)$ function gives the value of the volume fraction in the element e with phase α .

The physical laws and properties must be added in the file `usphyv.F`. For the air, the gas law is applied and the FORTRAN routine is the following:

```

      DO IEL=1, NCEL
        H3=RTPA ( IEL, IENTHT ( 3 ) )
&      -0.5 * ( RTPA ( IEL, IU ( 3 ) ) ** 2
&      +RTPA ( IEL, IV ( 3 ) ) ** 2
&      +RTPA ( IEL, IW ( 3 ) ) ** 2 )
        GAM=1.4
        PROPHY ( IEL, IROM ( 3 ) ) = GAM / ( GAM - 1. ) * RTPA ( IEL, IPR ) / H3
        PROPHY ( IEL, ITEMPK ( 3 ) ) = H3 / PROPHY ( IEL, ICP ( 3 ) )
      ENDDO

```

where the air temperature is defined as $T = h/c_p$. Details can be found in [31].

The enthalpy source term in the steam enthalpy equation due to direct contact with the air has been coded in the user-defined routine `usth12.F` and is given by

$$Q_{23} = 10^6 \alpha_2 \alpha_3 (T_3 - T_2). \quad (5.3)$$

The routine is the following:

```

ZET12 = 0. D0
  IF ( IPHAS2 .EQ. 3 ) THEN
    ZET12 = RTPA ( ICEL, IALPR ( IPHAS1 ) ) *
      RTPA ( ICEL, IALPR ( 3 ) ) * 1. D6
  ENDIF

```

This term is added in the enthalpy equation in order to prevent the calculation from diverging.

The source term in the steam momentum equation for the k-th direction, due to direct contact interaction with the air is coded in the user routine `ustsns.F`, is given by

$$M_{23}^k = \alpha_2 \rho_2 F d_{23} \frac{\alpha_3}{\rho_2} (U_3^k - U_2^k), \quad (5.4)$$

with

$$F d_{23} = 10^5 (1 + V_R^2) \left[\frac{kg}{m^3 s} \right], \quad (5.5)$$

and V_R is the module of the relative velocity between phases. The FORTRAN routine is reported here:

```

IF (IPHAS.EQ.2.OR.IPHAS.EQ.3) THEN
  ALP2 = RTPA (IEL, IALPR (2))
  ALP3 = RTPA (IEL, IALPR (3))
  ROM2 = PROPHY (IEL, IROM (2))
  ROM3 = PROPHY (IEL, IROM (3))
  VR23 = (RTPA (IEL, IU (3)) - RTPA (IEL, IU (2))) ** 2
&      + (RTPA (IEL, IV (3)) - RTPA (IEL, IV (2))) ** 2
&      + (RTPA (IEL, IW (3)) - RTPA (IEL, IW (2))) ** 2
  FD23 = 1.D5 * (1. + VR23)
  IF (IPHAS.EQ.2) THEN
    TSA (2) = TSA (2) - ALP3 * FD23 / ROM2
    TSA (3) = TSA (3) + ALP3 * FD23 / ROM2
  ENDIF
  IF (IPHAS.EQ.3) THEN
    TSA (2) = TSA (2) + ALP2 * FD23 / ROM3
    TSA (3) = TSA (3) - ALP2 * FD23 / ROM3
  ENDIF
ENDIF

```

The drag coefficient in the momentum equation is calculated in the user routine `usdrag.F`.

5.3.3 Results obtained for the test 9

In this section, the results of the two dimensional OP-injector system simulations are described in detail. In order to consider temperature evolution for test 9 as reported in Figure 5.12, it is possible to divide the experiment into four parts:

- Beginning;
- Temperature stratification (pool heating);

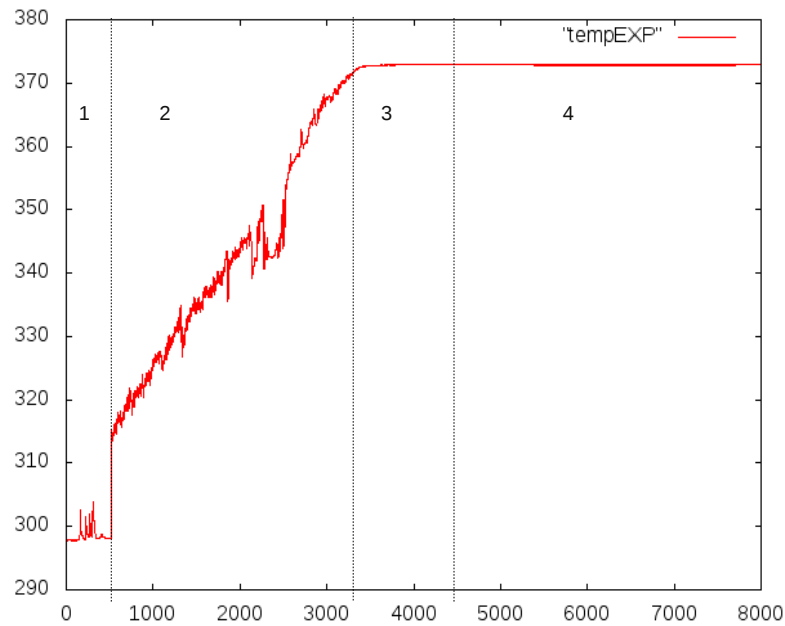


Figure 5.12: Chronology of the temperature main events for the probe *TP6*

- Steam injection (pool boiling);
- Injection above water level.

The time interval of each part is summarized in Table 5.3.

n	Description	Time (s)
1	Beginning of the test	0 -500
2	Pool heating	500-3200
3	Pool boiling	3200-4200
4	Low water level	4200-7700

Table 5.3: Chronology of the Temperature main events

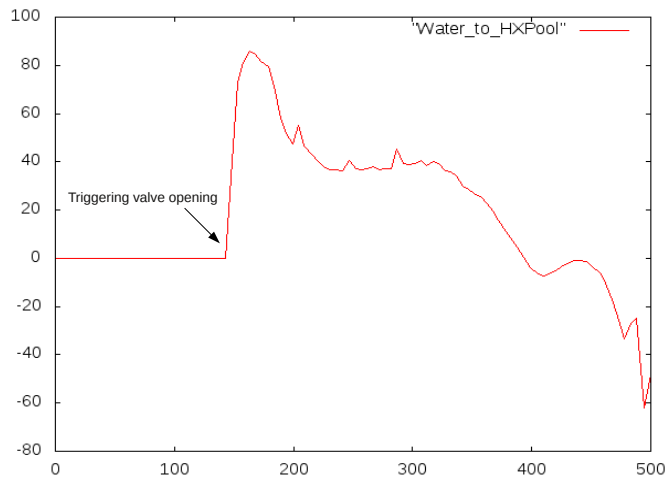
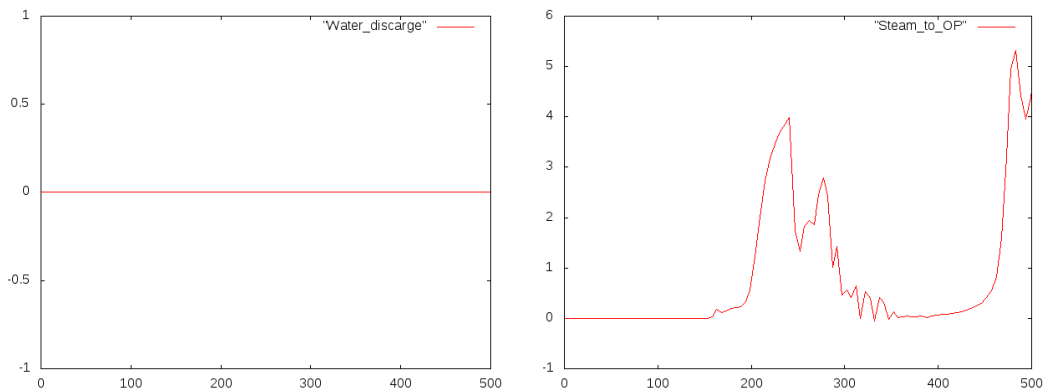
Beginning of the test

During the initial part of the simulation the pool temperature is low. Table 5.4 shows the initial conditions of the system ($t = 0$) and the boundary conditions for NEPTUNE during the time interval 0 – 500 s as computed by CATHARE are shown in Figures 5.13-5.14.

In Figure 5.13 and on the left of Figure 5.14 the water mass flowrate from Overall Pool to HX pool and the water discharge mass flowrate are shown, respectively. These

Parameter	Unit	Value
OP water level	m	4.50
OP water temperature	$^{\circ}C$	24.5
HX pool water level	m	1.222
HX pool water temperature	$^{\circ}C$	47

Table 5.4: Initial conditions of Overall Pool and HX pool.

Figure 5.13: Water mass flowrate to HX pool over the time interval $[0 - 500]s$ computed from CATHARE simulation.Figure 5.14: Water discharge mass flowrate and steam mass flowrate to overall pool over the time interval $[0 - 500]s$ computed from CATHARE simulation.

two flows are set as boundary conditions over the boundary that defines the water line. In order to do this the CATHARE values are interpolated at the time nodes and the

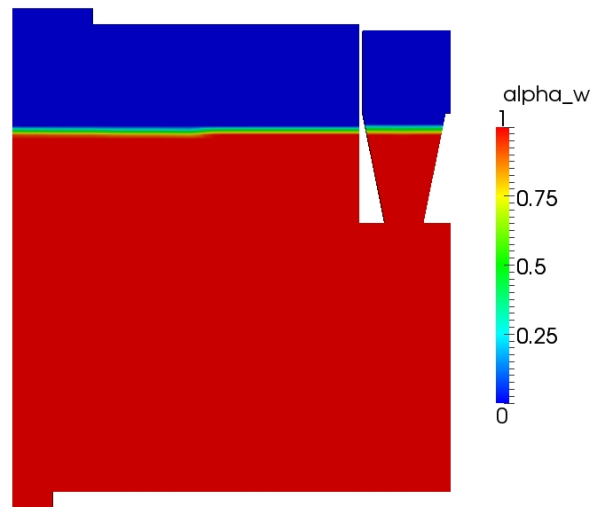


Figure 5.15: Water level at $t = 150$ s.

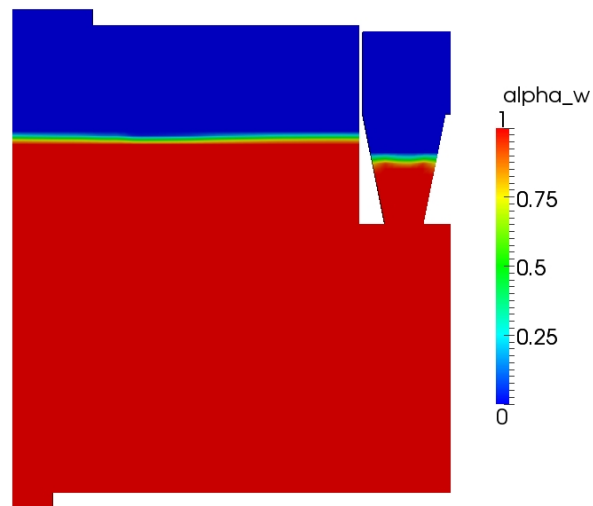


Figure 5.16: Water level at $t = 204$ s.

resulting interpolating functions are reported on the file `usclim.F` as described in the

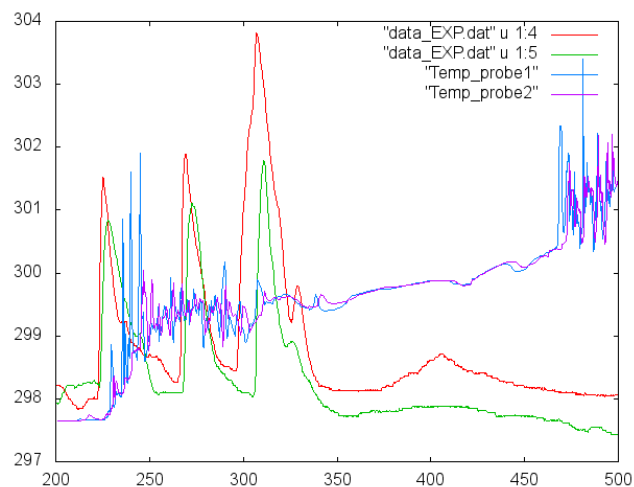


Figure 5.17: Computational and experimental temperature profiles in probes TP6 (1) and TP8 (2) as a function of time.

previous section. The steam mass flowrate from the HX pool to the Overall Pool is reported on the right of Figure 5.14. This mass flow generates the velocity at the steam inlet. Since the CATHARE solution provides a unique scalar value, the velocity profile is assumed to be constant.

During the interval $t \in [0, 143]$ s all the boundary mass flow rates are set to zero so that the system can reach a stable condition. At $t = 150$ s the water level of the simulation is almost everywhere uniform as one can see in Figure 5.15. During the interval $t \in [143 - 204]$ s a water level adjustment occurs. The resulting level in the Overall Pool is shown in Figure 5.16. The water levels in the injector and in the Overall Pool are different due to the steam pressure. In the final interval $t \in [204 - 500]$ s the steam enters the injector with a significant mass flowrate and the Overall Pool temperature increases in an appreciable manner. One can see this from the temperature probes in Figure 5.17. In this Figure the temperature values in probes TP6 (called 1) and TP8 (called 2) computed by NEPTUNE are reported as a function of time, along with the experimental measurements. It is important to remark that the agreement between computed and measured temperature profiles is not very good. The computed temperatures increase jointly and no temperature stratification, that is no temperature difference between the two probes, takes place. The CATHARE simulation of this facility does not exhibit a temperature stratification as well, due to the mono-dimensional nature of the model. The NEPTUNE computations are two-dimensional and therefore the code should be able to capture the stratification phenomenon. This means that either the initial or the boundary conditions or the modeling equations are not correctly implemented. Nevertheless, many attempts have been made with different conditions and different physical

models with the purpose of reproducing stratification, but none of them has been successful. This may be due to a wrong modeling of the injector for which the hypothesis of adiabatic walls is made.

Temperature stratification

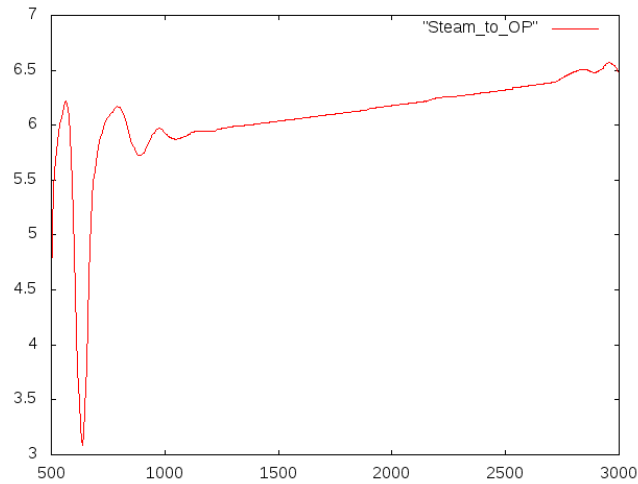


Figure 5.18: Steam mass flowrate to overall pool over the time interval $[500 - 3000]s$ defined from CATHARE simulation

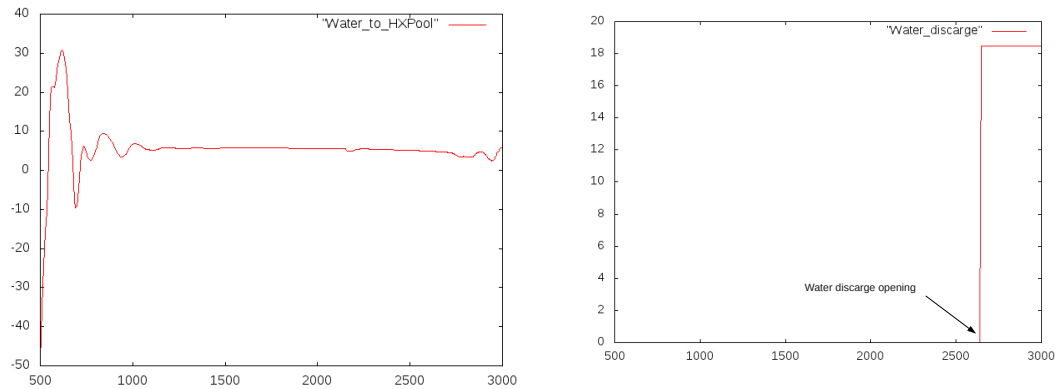


Figure 5.19: Water mass flowrate to HX pool and water discharge mass flowrate over the time interval $[500 - 3000]s$ defined from CATHARE simulation

During the interval $t \in [500 - 3200] s$ the pool temperature increases until it reaches boiling. For the time interval under study, the steam mass flowrate to the overall pool is shown in Figure 5.18; the water mass flow rates to the HX pool and to the discharge line are reported in Figure 5.19 on the left and right respectively. In two-dimensional

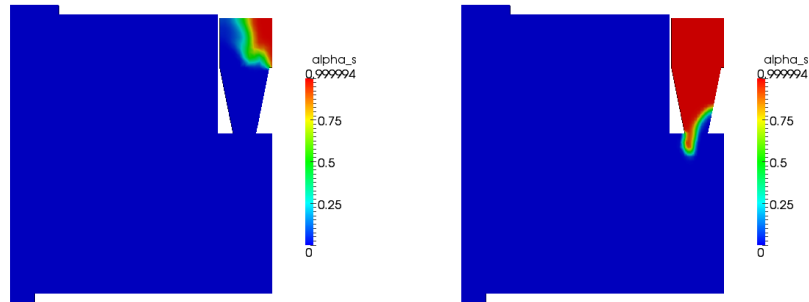


Figure 5.20: Steam entering the injector (right) and injection of steam into water (left)

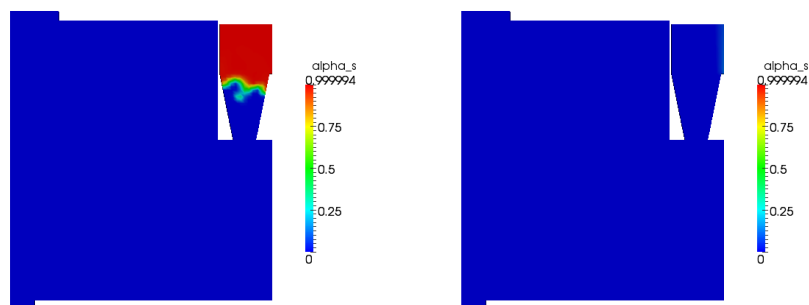


Figure 5.21: Steam and water mixing (right) and inverse flow (left)

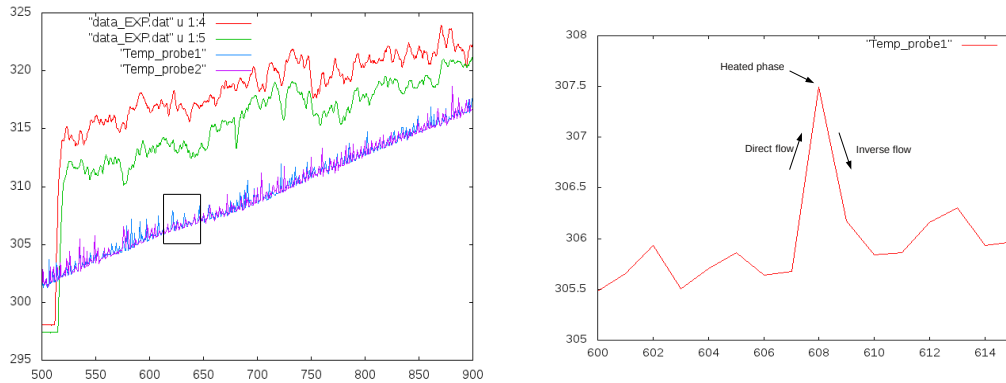


Figure 5.22: Temperature of the probes TP6 (red) and TP8 (green) from experiment and NEPTUNE computation (blue and violet) and zoom of the temperature oscillations

geometry these two flows may be added to define the boundary condition for the water line. The NEPTUNE simulation shows a great mixing with no temperature stratification. The mixing is generated by the cyclic behavior of the injector. The injector is periodically filled with steam. The steam cannot enter the pool and condensates near the injector outlet. The steam pressure pushes the water down till the level goes below the injector. The steam mixes with water and the water enters the injector again. The steam condensates and the water is sucked until it fills the injector almost completely. Then the cycle repeats again. This can be seen in Figures 5.20-5.21. On the top of Figure 5.20 the injector is filling with steam which then pushes the water level down (Figure 5.20 on the bottom). On the top of Figure 5.21 the water level drops down and water and steam mix quickly to fill again the injector completely as shown on the bottom of Figure 5.21. The resulting temperatures at the probes is shown in Figure 5.22. The experiment exhibits the temperature stratification while the simulation shows a strong turbulent mixing. Figure 5.22 on the right shows a zoom over a temperature oscillation. During the initial part of the injection the temperature increases when the injector fills with steam. The maximum temperature (heated phase) is obtained after the steam is injected into the pool. Then the temperature decreases since the cold water is sucked into the injector. The surrounding water temperature remains at the mixing pool temperature. This temperature is lower than the corresponding experimental temperature showing a high rate of mixing.

5.3.4 Steam injection on boiling pool

Around $t = 3200$ s the pool starts boiling. During the interval $t \in [3200 - 4200]$ s the steam is injected directly into a boiling pool. In Figure 5.23 the steam mass flowrate

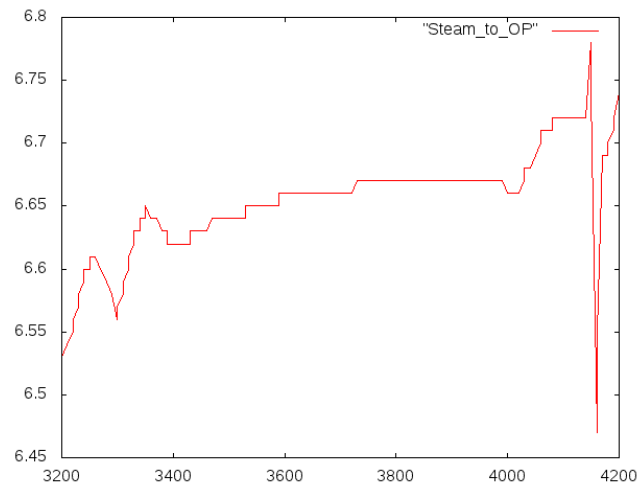


Figure 5.23: Steam mass flowrate to overall pool over the time interval $[3200 - 4200]s$ defined from CATHARE simulation.

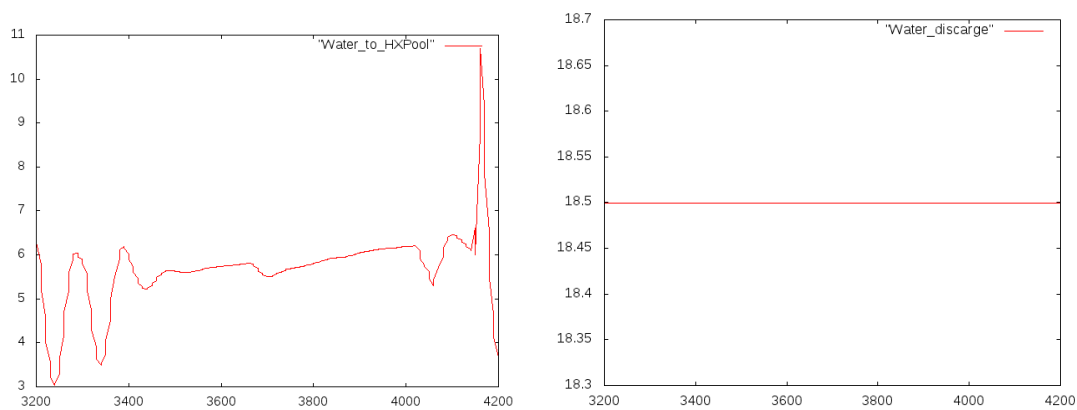


Figure 5.24: Water mass flowrate to the HX pool and water discharge mass flowrate over the time interval $[3200 - 4200]s$ defined from CATHARE simulation.

injected into the overall pool is reported as a function in the considered time interval. The steam mass flow has a steady value around 6.6 Kg/s. Figure 5.24 shows the water mass flowrate to the HX pool and the water discharge mass flowrate on the left and right, computed by CATHARE and used as boundary conditions for NEPTUNE simulation. The water discharge mass flowrate is kept to a constant value of 18 kg/s so as to rapidly decrease the water level in the overall pool. In Figure 5.25 the water temperature distribution at $t = 4000$ s is shown. All the water is boiling. The temperature field is extended from the water region to the whole pool region even if in these parts there is only steam or air. The top of Figure 5.26 shows the injection of steam into the boiling pool when the water level is below the injector outlet. In this case the condensation is

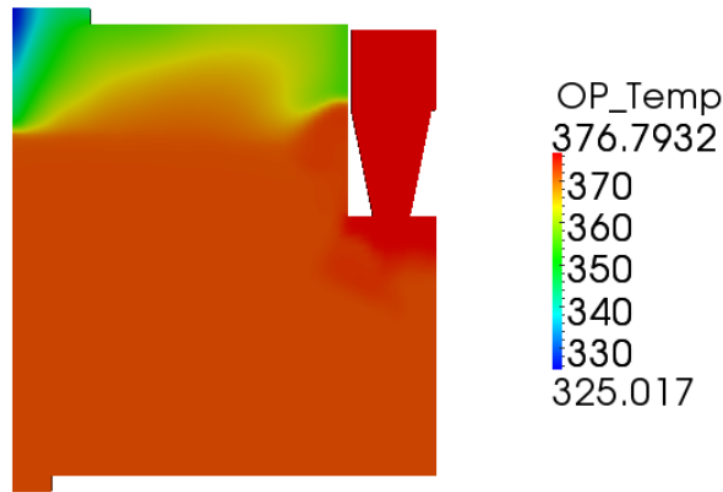


Figure 5.25: Extended water temperature distribution in boiling pool

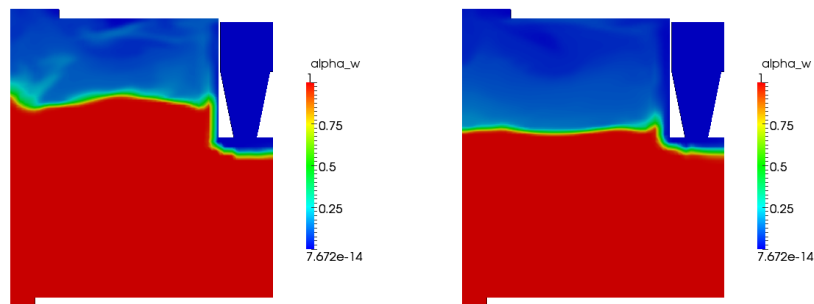


Figure 5.26: Steam injection on boiling pool (right) and steam release to the water surface (left)

minimal and all the steam goes above the level of the water pool as shown in Figure 5.26 on the bottom. Condensation may take place in some areas of the pool, especially near the boil-off where the cold air may condensate the saturated steam.

5.3.5 Injection above water level

During the interval $t \in [4200 - 7700]$ s the pool level decreases until it is below the injector outlet. Figure 5.27 shows the evolution of the steam mass flowrate entering the overall pool in this last time interval. The temperature of this flow is the saturation temperature. In a similar way in Figure 5.28 the water mass flowrate to the HX pool and the water discharge mass flowrate are shown on the left and right respectively. The

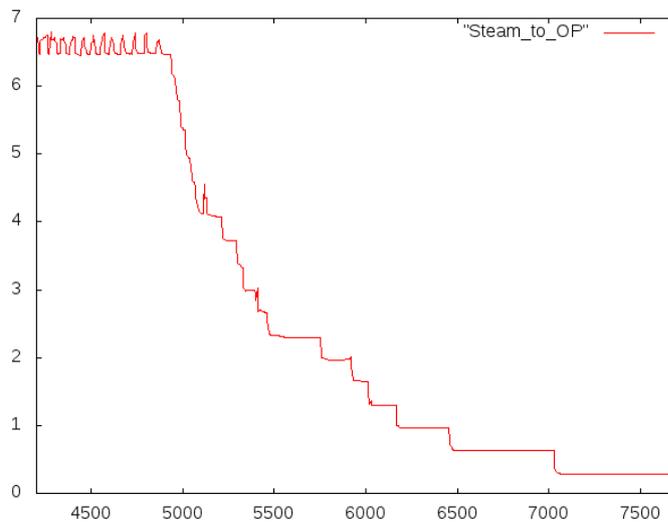


Figure 5.27: Steam mass flowrate to overall pool over the time interval $[4200 - 7700]$ s defined from CATHARE simulation.

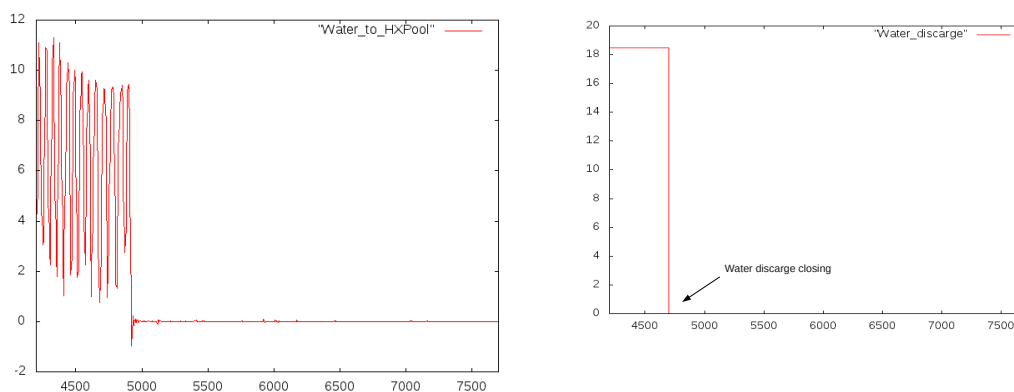


Figure 5.28: Water mass flowrate to the HX pool and water discharge mass flowrate over the time interval $[4200 - 7700]$ s defined from CATHARE simulation.

water discharge mass flowrate is kept constant to 18.8 kg/s till about $t = 4700$ s and then it is set to zero when the water discharge line is closed. The temperature on this boundary region is room temperature. With these boundary conditions the velocity and temperature profiles of all the phases can be computed. The top of Figure 5.29 shows the steam injection into the water pool. In Figure 5.29 on the bottom the steam is injected above the water level. There is no mixing with water and the energy is released directly to the pool surface. From the pool surface the steam mixes with the air and then it goes out of the system through the boil-off boundary. In this case the NEPTUNE code simulates pretty well the heat exchange between the different phases.

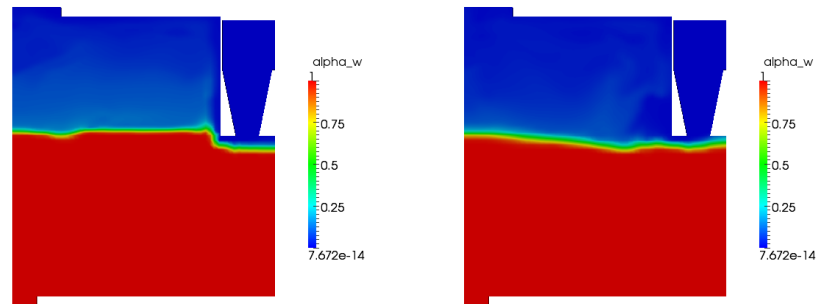


Figure 5.29: Steam injection above the water level.

5.4 The OP-injector three-dimensional model

In order to improve the investigation within the Overall Pool and to better understand what happens inside the injector and the pool, a 3D simulation of the system is performed [31]. In the next sections the results obtained by simulating the Overall Pool and the injector system on three hexahedral meshes with different geometry are presented.

5.4.1 Results obtained for the test 9

Case 1 - Real geometry

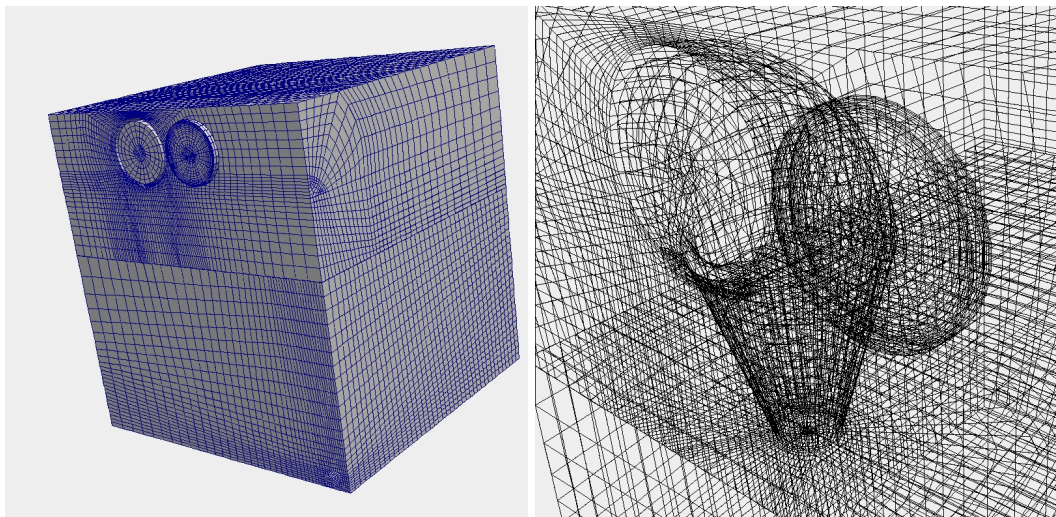


Figure 5.30: PERSEO 3D hexahedral grid (left) and a detail of the injector and boil-off region (right) for the real geometry

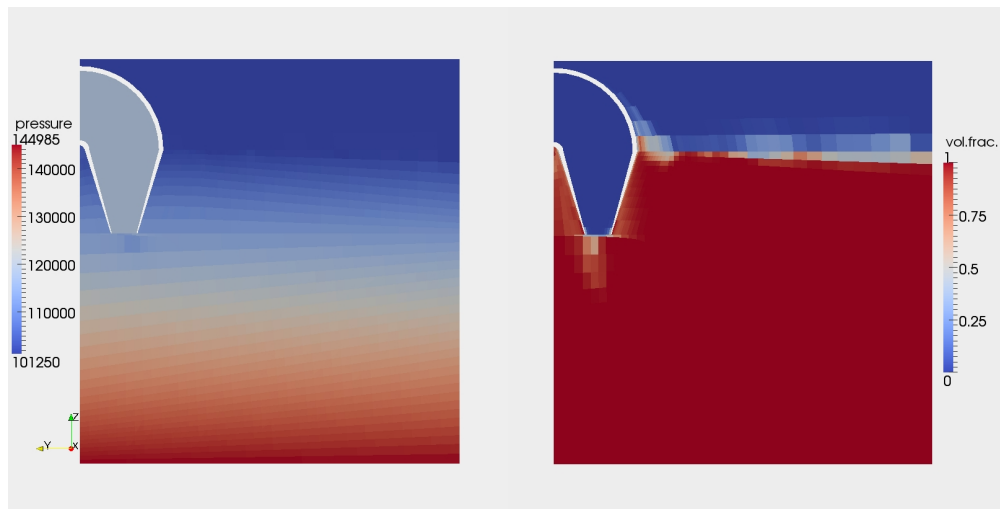


Figure 5.31: Pressure [Pa] (left) and water volume fraction (right) at a $x=3.12$ m section for $t_1 = 9.08398$ s

In a first analysis, the OP-injector model has been constructed on the real geometry of the overall pool and of the injector. In Figure 5.30 the external part of the mesh and a detail of the injector and boil-off zone are shown. The grid is composed by 85041 hexahedral cells. It can be seen how the most refined zones are close the injector nozzle and below the injector bend. The dimensions of the small cells below the injector bend are determined by the high curvature of the injector wall and by the proximity to the pool wall. In these cells the local *Courant number* has its highest values. The time step is then determined by the field values in these cells, while the *Courant number* in the rest of the computational domain is much lower. This results in a very low efficiency of the calculation. In addition, very small time steps may induce instabilities on the calculation, because of the time derivative terms in the pressure equation. It should be noted that the grid has been constructed by taking advantage of the NEPTUNE capability to deal with non-conforming grids. As a matter of fact, the first mesh is given by the union of different parts: the upper half of the pool, the lower half of the pool, the injector, the boil-off and the water line sections. All the junctions are non conforming. It must be emphasized that the code proved to be very sensible to sharp changes in the cell dimensions, even across the grid junction. Therefore, a great attention must be given to this aspect while constructing new grids. Since the steam mass flowrate is approximately zero up to the time $t_0 = 153$ s, the simulation is shifted in time by the quantity t_0 so that the real time is $t = t_1 + t_0$, where t_1 is the simulation time. In Figure 5.31 the pressure and water volume fraction fields are shown on a vertical section passing through the injector axis at time $t_1 = 9.08398$ s. It can be observed that the steam condenses right at the injector nozzle and that the cell deformation near the

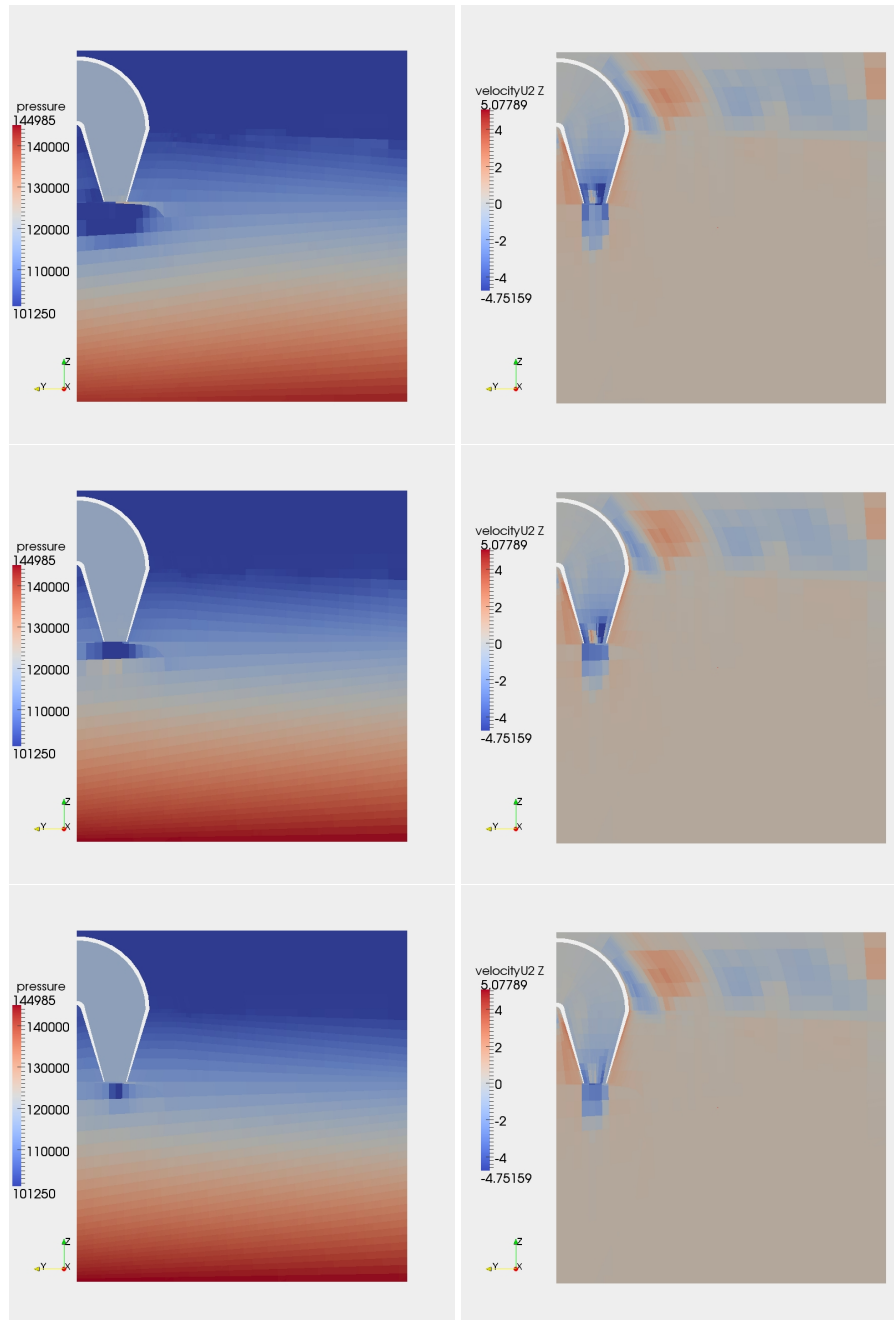


Figure 5.32: Pressure [Pa] (left) and z component of steam velocity [m/s] (right) at a $x = 3.12\text{ m}$ section for $t_1 = 9.09419\text{ s}$ (top), $t_1 = 9.09833\text{ s}$ (middle) and $t_1 = 9.10886\text{ s}$ (bottom)

free surface causes some distortion in the surface reconstruction itself. In Figure 5.32 a sequence of pressure and steam vertical velocity distributions are presented in the time interval $9.09419\text{ s} < t_1 < 9.10886\text{ s}$. At this early stage of the experiment the steam mass

flowrate is very low ($Q_{steam} = 0.157 \text{ kg/s}$) and its velocity does not exceeds 5 m/s . This is the reason for the prompt steam condensation right at the injector nozzle. As it can be seen from the pressure field, the steam condensation causes a pressure drop near the nozzle which then extends to the region between the injector and the pool wall. These pressure fluctuations are also caused by the fact that the volume occupied by the steam inside the injector is too small to compensate the volume lost during the condensation and in a low-mach number formulation of the problem, the boundary conditions do not react to such a loss in volume. This pressure fluctuations propagate inside the injector until the simulation finally does not converge. However, many sources of instability overlap in this simulation. For this reason it has been decided to generate new grids starting from a simplified geometry, in order to isolate and correct the most important factors that lead the simulation to divergence.

Case 2 - Geometry with straight injector at the real position

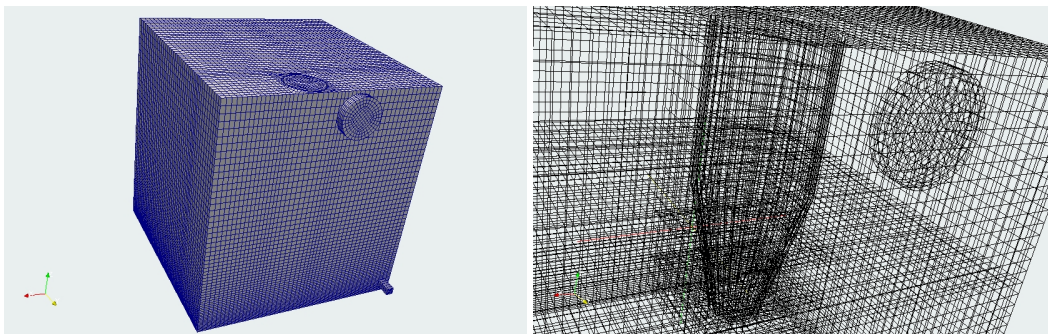


Figure 5.33: PERSEO 3D hexahedral grid (left) and a detail of the injector and boil-off region (right) for the geometry with straight injector and real position of the injector exit

In order to reduce the possible sources of numerical instabilities, a new geometry has been generated by introducing a straight injector entering the pool from the top of the domain. The injector nozzle is in the same position and with the same area. The grid is still composed by different blocks: lower half of the pool, upper half of the pool, block around the injector, boil-off, injector, (WD) and (WL) water lines. With respect to the first mesh, a block of cells in the part of the pool around the injector as been added. This block has conforming junctions with the remaining part of the upper pool, even though the grid size in the normal direction of the connecting surfaces undergoes a steep variation, especially in the upper part of the injector (again the short distance from the pool wall requires small cells) and near the injector nozzle. The junctions between the grid in the lower half of the pool and the other blocks are non conforming but the grid size in the direction normal to the common surfaces are kept constant on

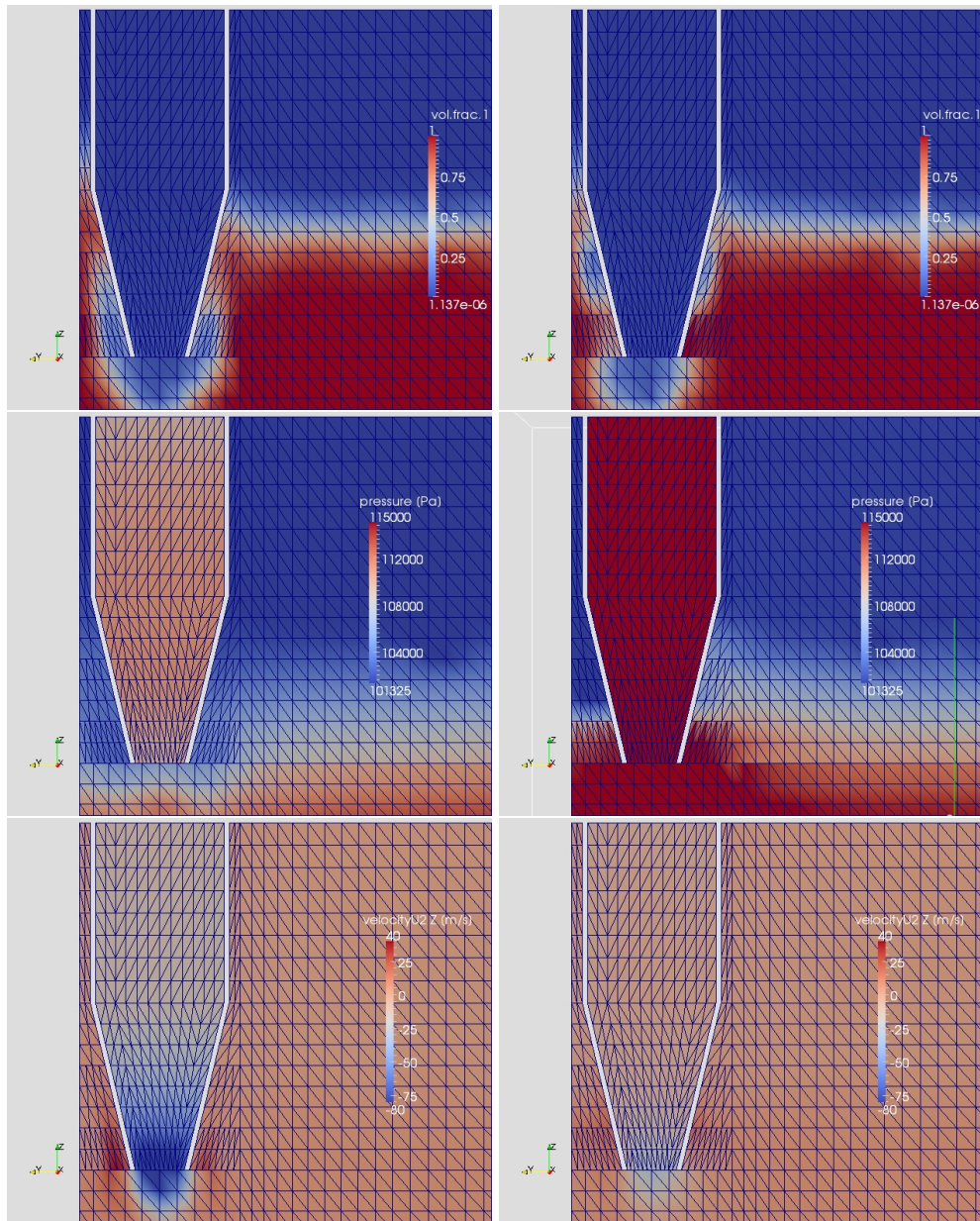


Figure 5.34: Water volume fraction (top), pressure (middle) and vertical component of steam velocity (bottom) for $t_1 = 50.6804$ s (left) and $t_1 = 51.8309$ s (right) on a section at $x=3.312$

both sides. The mesh has now 129338 hexahedral cells. With the second mesh the simulation starts at time $t_0 = 451$ s, that is before the increase of the steam mass flow at the inlet takes place. The simulation appears to be more stable than with the first mesh, but a few changes were required in the user defined functions in order to run the simulation up to $t_1 = 60$ s. More particularly, in the drag model `usdrag.F` the water characteristic diameter was set to $d_1 = 5 \cdot 10^{-5}$ when the water volume fraction

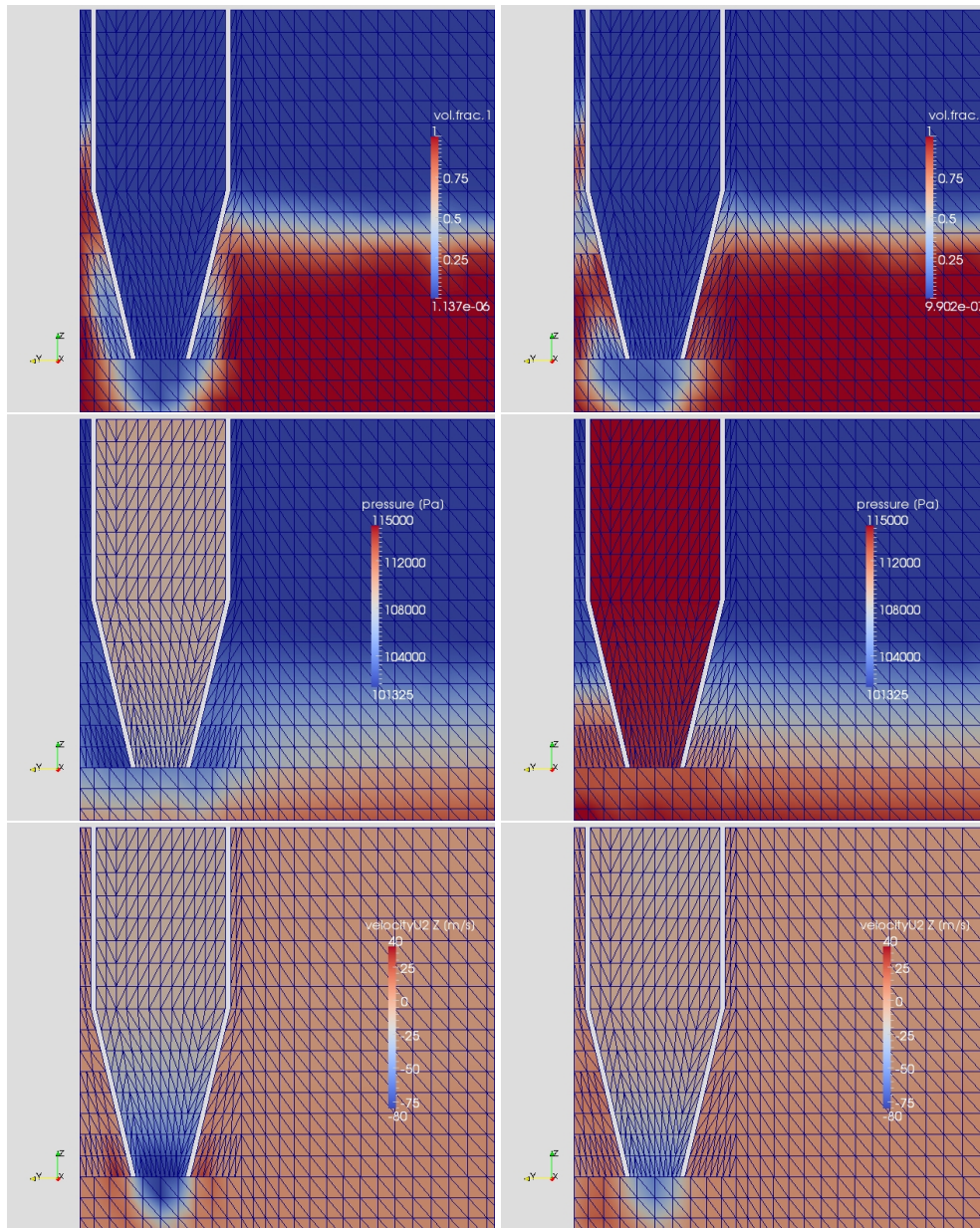


Figure 5.35: Water volume fraction (top), pressure (middle) and vertical component of steam velocity (bottom) for $t_1 = 53.7734$ s (left) and $t_1 = 55.9895$ s (right) on a section at $x=3.312$

$\alpha_1 < 2 \cdot 10^{-5}$, in order to prevent the water velocity to diverge in the region of the domain where water is not actually present. However, the pressure fluctuations due to the prompt steam condensation were still present inside the injector, and the routine `usclim.F` was modified in order to reduce this effect. From the available experimental data it is found that the pressure inside the HX pool is almost constant with a value close to $P = 113000$ Pa. Thus a correction for the steam mass flowrate Q_{steam} has

been introduced in such a way that Q_{steam} is set to zero when the pressure at the inlet section exceeds $P^{up} = 115560 Pa$, on the other hand it is increased when it drops below $P^{low} = 109250 Pa$. The correction for this second case is

$$Q_{steam} = \sqrt{[Q_{steam}^0]^2 + Q_{adj}} \quad (5.6)$$

$$Q_{adj} = 2(P^{low} - P^{in})^* \rho A_{in}^2 \quad (5.7)$$

$$(P^{low} - P^{in})^* = \min(\text{pos}(P^{low} - P^{in}), 1) \quad (5.8)$$

where P^{in} and A_{in} are the pressure at the inlet section and its area, respectively. With this correction the simulation was run up to $t_1 = 60 s$, even if it was not possible to have a perfect control on the mass injected in the system, therefore an intermediate stage was considered. In Figures 5.34-5.35 the evolution of water volume fraction, pressure and steam vertical velocity is presented on a section passing through the injector, at times in the interval $50.6804 s < t_1 < 55.9895 s$. A part of the mesh is also shown. It can be seen the oscillatory behavior of the flow close to the injector, with the pressure decreasing when the highest velocities are reached at the injector nozzle and the water is pushed away from that position. Then the velocity decreases, the water comes back closer to the nozzle and the pressure inside the injector increases again. It should be observed that the pressure field presents spurious oscillations at time $t_1 = 51.8309 s$ which are probably caused by the jump in the grid size in that region along the two horizontal directions. The observer should also be aware that the software PARAVIEW, which is used for data visualization, reconstructs the field on triangles when performing a cut. The wiggles along the lines that cut the squared cells with triangles may be in part due to the software itself. With the correction in the mass flowrate the simulation run up to time $t_1 = 60 s$, but finally diverged. However, this simulation pointed out that one of the main reasons for the numerical instability of the run was the excessive stiffness of the boundary conditions together with a too small portion of the domain occupied by the steam. Another critical aspect was identified in the junction of the grid blocks, where the grid size undergoes a steep variation.

Case 3 - Geometry with the injector in central position and an additional volume simulating a portion of the HX pool

In order to further reduce the sources of numerical instabilities a third geometry has been considered. In Figure 5.36 the discretized geometry is shown together with a local zoom of the injector region. Furthermore, to prevent the pressure oscillations inside the injector, a larger cylindrical vessel has been added upstream. The volume of such a vessel is approximately that occupied by the steam in the HX pool. The inlet section, where the boundary conditions from the CATHARE simulation are imposed, is now

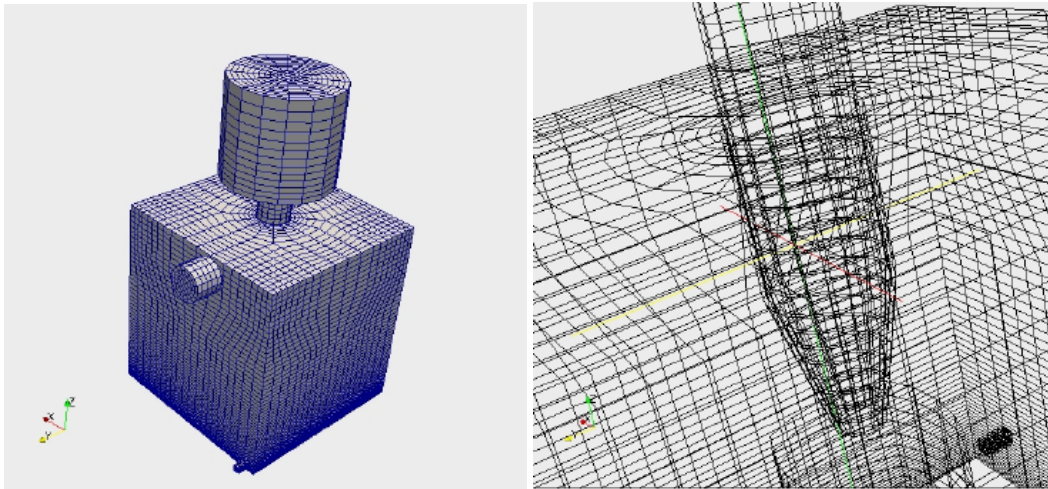


Figure 5.36: PERSEO 3D hexahedral grid (left) and a detail of the injector region (right) for the geometry with a straight injector and a modified position of the injector nozzle

the upper surface of this volume. With this modification the pressure fluctuations inside the injector, which are due to the prompt condensation of the steam, are greatly reduced. With the repositioning of the injector in the center of the domain, the change in the geometry is not negligible and this has an impact on the comparability between numerical and experimental data, but it allows to create a single mesh inside the pool, without non-conforming junctions or sudden changes in the grid size. Furthermore, it removes the presence of small size cells, and the smaller grid dimension is now the injector wall thickness. The grid has now 32250 hexahedral cells and with these changes larger time steps are now possible, removing in this way a possible source of instability. The simulation has been performed with a variable time step, which is determined by several stability coefficients (CFL , CFL_α , $Fourier$). It should be remarked that the stability limit of these coefficients was not constant during the simulation. At the very beginning, when the steam mass flowrate at the inlet $Q_{steam} < 3 \text{ kg/s}$, the system undergoes very large fluctuations: the steam condensation takes place inside the injector until the pressure in the injection system is high enough to push the water out of the injector. This fluctuating behavior can be seen in Figure 5.37 where the water volume fraction and the steam condensation rate are both shown in the time interval $12.88 \text{ s} < t_1 < 15.18 \text{ s}$. Under these severe conditions the stability limit on the CFL_α condition had to be kept in the range (0.15–0.2). This is probably due to the fact that the phase front moves suddenly and at a high velocity and the time step must be tailored on this key feature of the flow. As the mass flowrate at the inlet is increased, the steam velocity is higher and the water front never comes back inside the injector, as shown in Figure 5.38. Steam condensation mostly takes place at the exit of the injection system

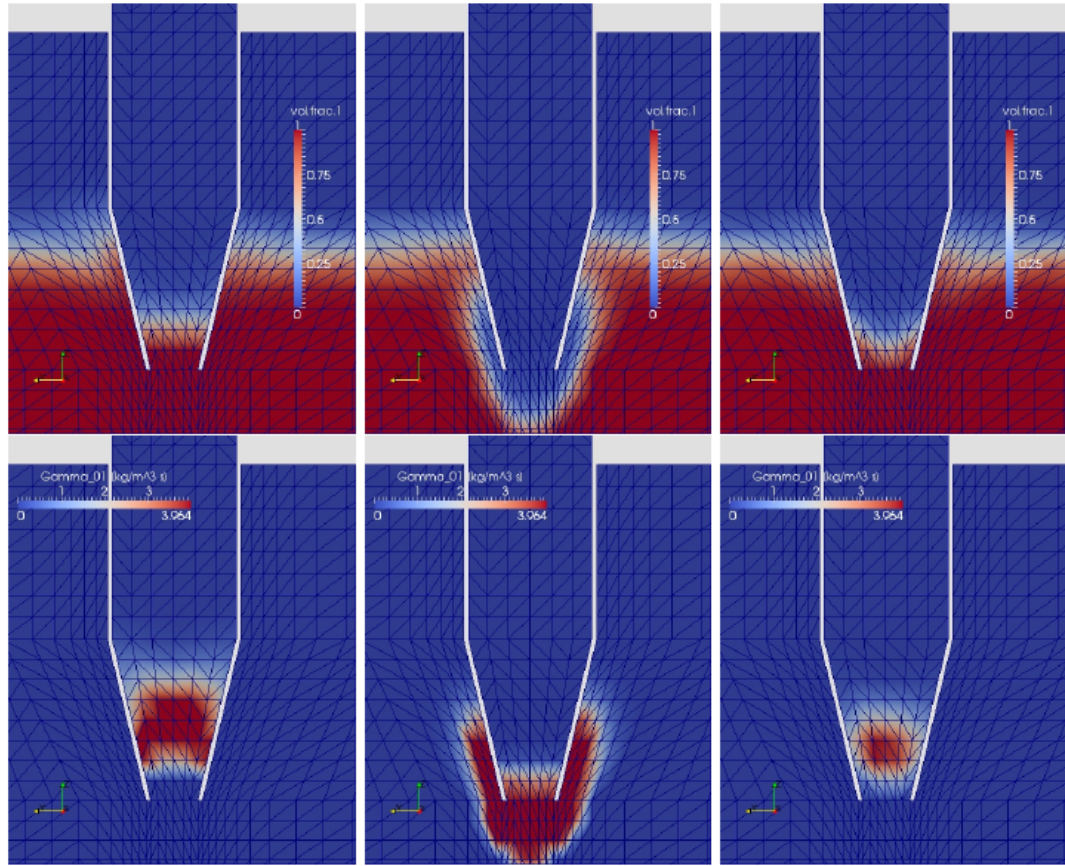


Figure 5.37: Water volume fraction (top) and condensation rate (bottom) for the geometry with a straight injector and a modified position of the injector nozzle, at times $t_1 = 12.88, 14.15, 15.18$ s (left to right)

or outside of it. At the same time, the high steam velocity at the exit and the small grid dimension below the injector wall require a very small time step. If the stability limit is left at $CFL_\alpha \sim 0.2$, the time step is excessively small and the calculation diverges in the $\alpha - P - H$ loop. For this reason the stability limits have been set to $CFL = CFL_\alpha \sim 0.5$ and $Fourier = 1.0$. The velocity field for $t_1 = 200.6$ s is shown in Figure 5.39. From the vertical component of the steam velocity it can be seen that the steam flowing out of the injector can reach the velocity $U_{2z} = -188$ m/s, while the maximum velocity of the flow going up outside the injector is $U_{2z} = 74.55$ m/s. As a consequence the radial component of the velocity reaches its highest value right below the end of the injector wall. The water temperature field evolution in the time interval 200.6 s $< t_1 < 243.36$ s is presented in Figure 5.40 together with the corresponding water volume fraction. It can be seen how the high-temperature region below the injector does not extend far below the water/steam front. On the contrary, a possible temperature stratification due

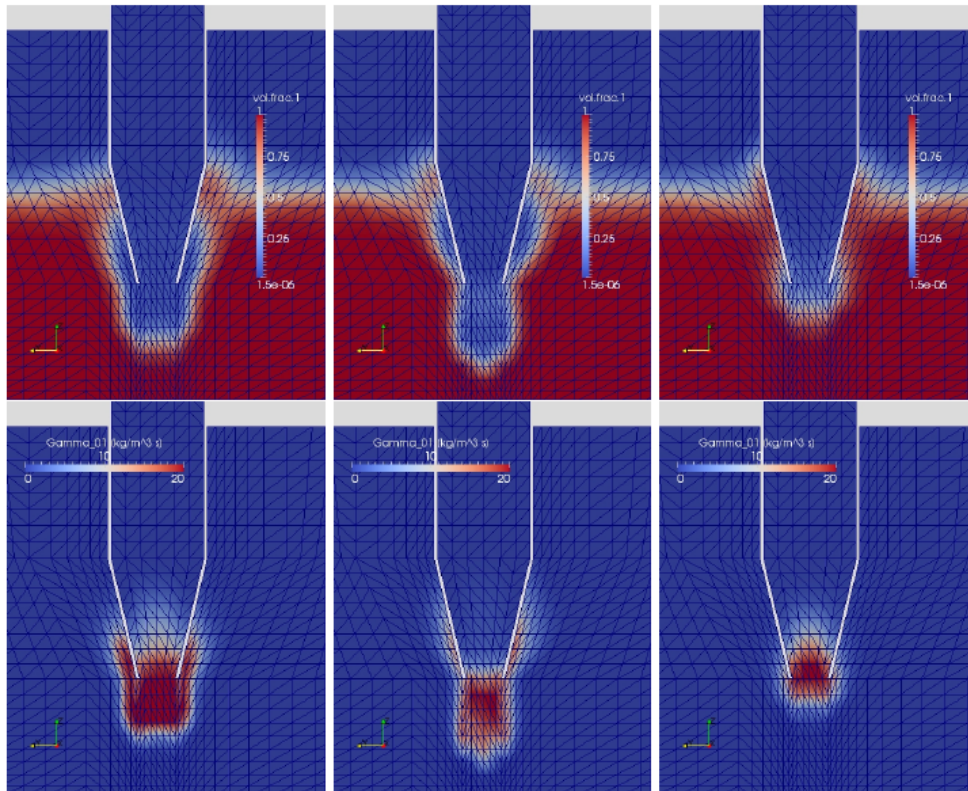


Figure 5.38: Water volume fraction (top) and condensation rate (bottom) for the geometry with a straight injector and a modified position of the injector nozzle, at times $t_1 = 200.6, 202.97, 205.52$ s (left to right)

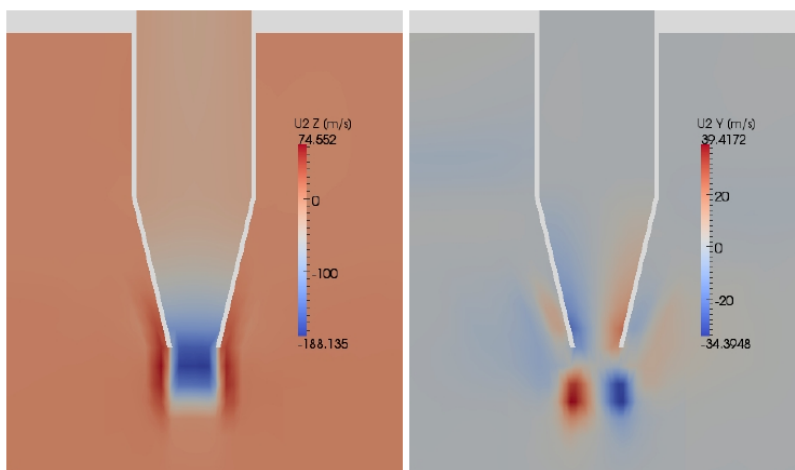


Figure 5.39: Vertical (left) and radial (right) steam velocity components on the vertical section through the injector axis at $x = 2.75$ m and time $t_1 = 200.6$ s, for the geometry with a straight injector and a modified position of the injector nozzle

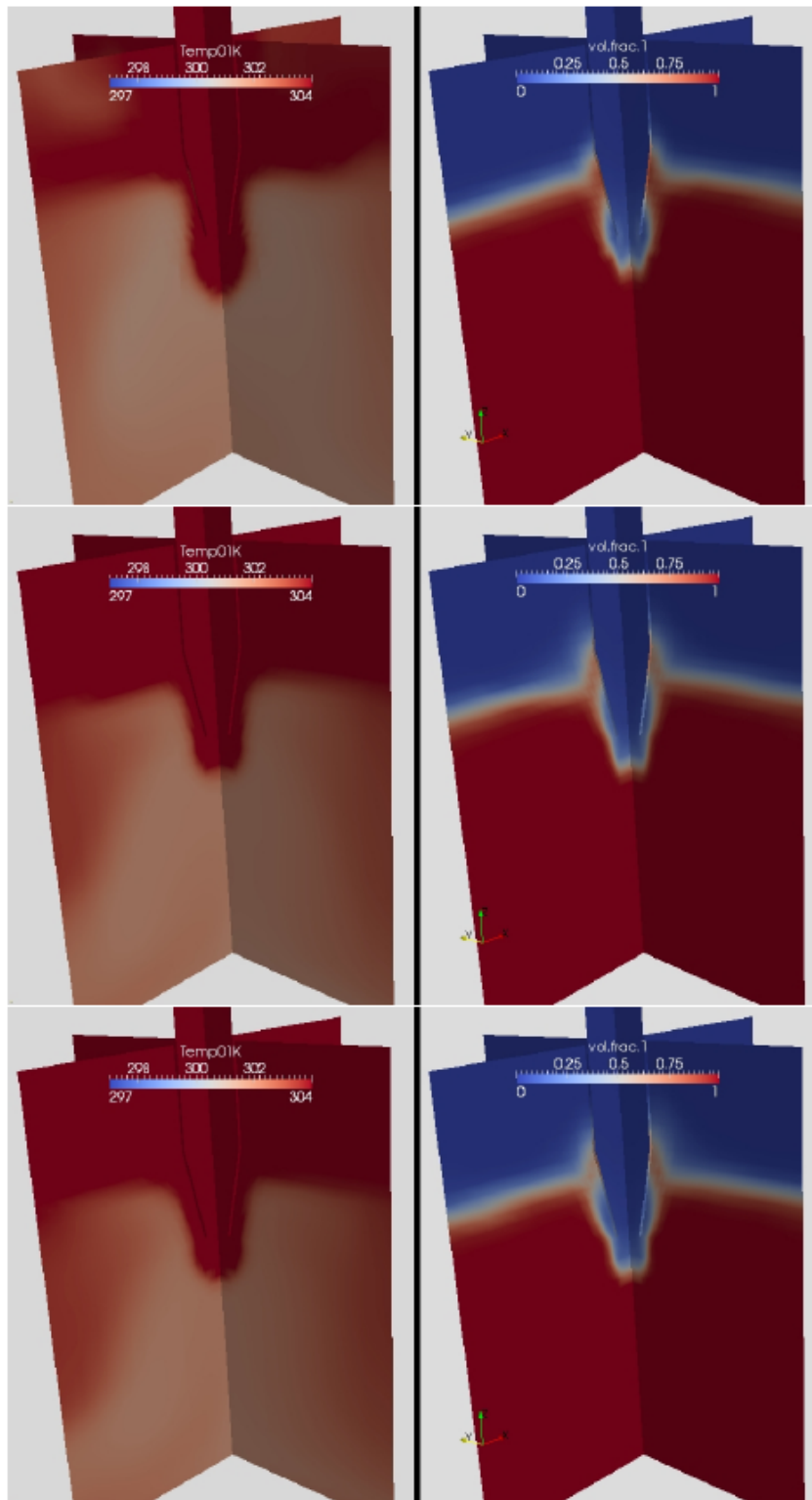


Figure 5.40: Water temperature (left) and volume fraction (right) on the vertical sections through the injector axis at $x = 2.75\text{ m}$ and $y = 2.75\text{ m}$ and times in the range $200.6\text{ s} < t_1 < 243.36\text{ s}$, for the geometry with a straight injector and a modified position of the injector nozzle

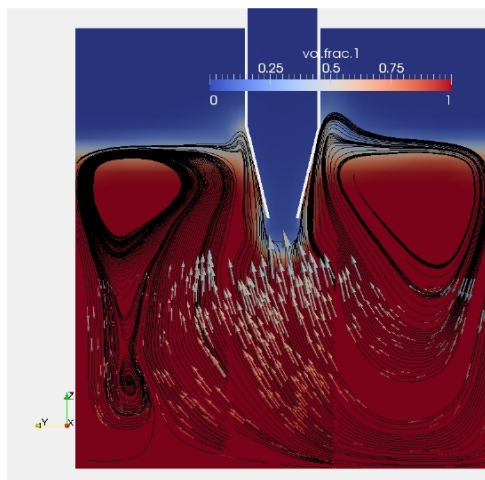


Figure 5.41: Water streamlines and velocity vectors (lower part only) on plane $x = 2.75 \text{ m}$ for $t_1 = 213.28 \text{ s}$. Contours for water volume fraction.

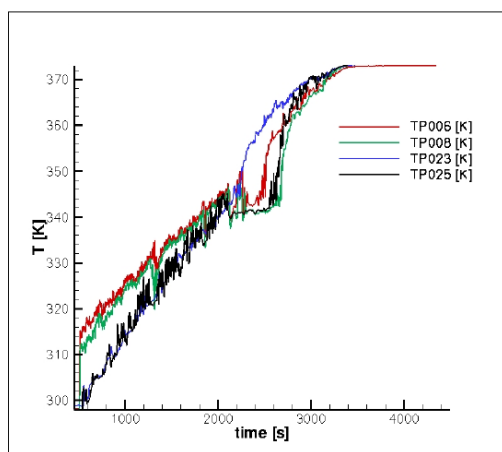


Figure 5.42: Experimental water temperature evolution for different probes

to the presence of the wall can be observed near the pool lateral boundary. The reason may become clear by looking at Figure 5.41. There is a net transfer of vertical momentum to the water in the upward direction due to buoyancy effects because of the heated water and to friction on the steam upflow near the external wall of the injector. A circulation is therefore setup inside the pool, with the fluid moving upwards in the central part and downwards close to the lateral walls. However, in the real configuration the injector is positioned close to the wall and buoyancy and wall effects will then overlap. Because of this consideration we should reconsider the experimental data and verify if the assumption that the temperature stratification, at least in this first part of the transient, is mainly due to a wall effect. With reference to Figure 5.42 two couples of probes

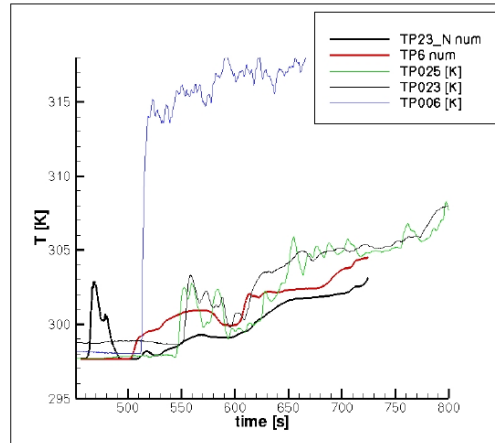


Figure 5.43: Comparison between experimental and numerical water temperature data for different probes

are considered. The first couple, $TP006$ and $TP008$, are positioned below the injector while the second one, $TP023$ and $TP025$, are located towards the pool center. The two probes $TP006$ and $TP023$ positioned at 2.195 m from the pool bottom, the other two at 1.195 m . There is clearly a temperature difference between the two probes located below, which is not present in the records of the two probes positioned at the pool center, at least in the first part of the transient. It should also be noted that the probes below the injector undergo a very fast temperature rise at the beginning of the transient, while the temperature rise is much more gradual for the probes in the pool center. A consistent temperature stratification seems to be present for $t > 2000\text{ s}$, when both the probes at the higher level register temperature values higher than the lower probe ones.

In Figure 5.43 the comparison between numerical and experimental data is shown. The experimental data refer to probes $TP006$, $TP023$ and $TP025$. The numerical data are taken at the same position of $TP006$ ($TP6_num$) and below the injector at the same vertical level as $TP006$ and $TP023$ ($TP23_N_num$). The exact position for the latter numerical probe is given, in the simulation frame of reference, by the following coordinates $x = 2.815\text{ m}$, $y = 2.7355\text{ m}$, $z = 2.195\text{ m}$. It can be seen how the numerical data follow quite closely the experimental data taken from the probes at the pool center ($TP023$ and $TP025$). The fact, that the experimental data for $TP006$ show a completely different behavior, with a sudden temperature rise up to $T \simeq 315\text{ K}$ seems to confirm the coupled effect of the injection and wall effects. The comparison between the two numerical series, with $TP6_num$ always above $TP23_N_num$, shows the presence of a wall effect. It should be considered that in the real case the injector is close to the lateral wall, the hot water below the injector moves immediately downwards, before it can exchange heat with the surrounding colder water. This may explain the steep rise

in temperature evolution at *TP006* which can be seen in the experimental data.

Conclusions

In the present work, a coupled CATHARE-NEPTUNE CFD simulation has been performed. The main objective is to simulate the behaviour of an innovative heat removal system with in pool heat exchangers and, in particular, to explain, through a CFD simulation, the temperature stratification present in the experimental data taken from the probes below the injector system. As a first step, a reference solution for the system evolution by using the system code CATHARE has been obtained. From this solution, proper boundary conditions to simulate the Overall Pool (OP) and the injection system components by using the NEPTUNE CFD code have been derived. In a first analysis, a two-dimensional model with a simplified geometry of the Overall Pool-injector system has been adopted. The numerical results obtained with this model are slightly different respect to the experimental data. This may be due to a wrong modeling of the injector for which the hypothesis of adiabatic walls is made. In order to better investigate the water-steam behaviour inside the pool and the injector, a three-dimensional solution with different geometries has been obtained for the first part of transient evolution of the PERSEO Test 9 . Three different configurations have been investigated by means of three-dimensional simulations. The results of this analysis are briefly recalled below. The 3D OP-system simulation with the real geometry diverges. This is due to the pressure fluctuations inside the injector and because of the small cells below the injector bend. These cells are determined by the high curvature of the injector wall and by the proximity to the pool wall. Here, the local *Courant number* has its highest values. The time step is then determined by the field values in these cells, while the *Courant number* in the rest of the computational domain is much lower. This leads to in a very low efficiency of the calculation. In addition, very small time steps may induce instabilities on the calculation, because of the time derivative terms in the pressure equation. In order to avoid the instabilities due to the bend injector of the real three-dimensional geometry, simulations with the straight injector entering the pool from the top at the same position respects to the real geometry has been performed. The pressure fluctuations, which do not allow temperature stratification, are still present. These are mainly due to the high rate of steam condensation inside the injector. Though corrections have been

implemented in the model through the boundary conditions, that improved the code stability for the first part of the transient, no stable solution could be obtained. Another critical issue was the interaction of non-conforming grid junctions with the described oscillations. The last three-dimensional model locates the injector in central position surrounded by an additional volume simulating a portion of HX pool, to prevent the pressure oscillations inside the injector. The grid adopted for this configuration is fully conforming. With this new configuration, the simulation is stable, although the temperature results are slightly different respect to the experimental data, since the real position of the injector is not preserved. It should be noted that temperature stratification is not predicted below the injector by the model. Wall effect is therefore to be considered a key issue for the setting of the stratification. In order to improve the results obtained, a new model, concerning the only injector system, can be realized to investigate the heat exchange between the steam and the liquid phases at the interface and to reproduce the condensation/ebollition phenomena inside the injector. Then, an overall pool system can be modeled by considering as boundary conditions the results obtained from the injector simulations.

The multi-scale and multi-physics computation coupling monodimensional and three-dimensional codes is still in a development stage but it should be considered the unique way to define the behaviour of systems where the time and length scales of individual processes involved differ by orders of magnitude.

Bibliography

- [1] G. Laviaille, *Cathare V2.5_1: USER'S MANUAL*, Laboratoire de developpement des applications pour les systemes, CEA, Grenoble, France, Mars 2006.
- [2] , *www-cathare.cea.fr*.
- [3] D. Bestion, G. Geffraye, *The Cathare Code*, Laboratoire de developpement des applications pour les systemes, CEA, Grenoble, France, Avril 2002.
- [4] , D.Bestion, *Interfacial friction determination for the 1-D 6-equation 2-fluid model used in the CATHARE code*, European Two Phase Flow Meeting; Marchwood, 1985.
- [5] , D.Bestion, *The physical closure laws in the CATHARE code*, Nuclear Engineering and design, Vol.124, pp 229-245, 1990.
- [6] J.Bartak, T.Haapalehto, *Simultaneous bottom and Top-down rewetting calculations with the CATHARE code*, Nuclear Technology, Vol. 106, pp 46-59, 1994.
- [7] J.Kelly, J.Bartak, A.Janicot, *Reflow modelling under oscillatory flow conditions with CATHARE*, New Trends in Nuclear System Thermalhydraulics, Pisa, Italy, Mai-June 1994.
- [8] I.Bartak, D.Bestion, T.Haapalehto, *The top-down reflooding model in the CATHARE code*, NURETH6, Grenoble, France, October 1993.
- [9] T.Maciaszek, J . C . Micaelli, D.Bestion, *Modelisation de l'autovaporisation dans le cadre d'un modele á deux fluides II*, La houille blanche, Vo1.2, pp129-2133, 1988.
- [10] A.Janicot, D.Bestion, *Condensation for ECC injection*, Nuclear Engineering and Design, Vol.2 pp 129-133, 1993.
- [11] D.Bestion, P.Coste, *Study on condensation modelling in the CATHARE code with and without non condensable gases*, New Trends in Nuclear System Thermalhydraulics, Pisa, Italy, May-,June 1994.

- [12] P.Coste, D.Bestion, *A simple modelling of mass diffusion effects on condensation with non condensable gases for a 1-D 2-fluid code*, Second international Conference on Multiphase Flow, Kyoto, Japan , April 1995.
- [13] CSSI, A. Fouquet, *CATHARE 2 V2.5.1 : Dictionary of operators and directives* Laboratoire de developpement des applications pour les systemes, CEA, Grenoble, France, Avril 2008.
- [14] *User Guide of NEPTUNE_CFD 1.0.8*, EDF, R&D, CEA, France 2010.
- [15] Y. Fournier, *Code_Saturne version 1.1: guide pratique et theorique du module Enveloppe*, EDF R&D report HI-83 /03/007.
- [16] Lavieville J., Quemerais. E., Mimouni S., Boucker M., Mechitoua N. *NEPTUNE CFD V1.0 theory manual*, EDF, R&D, INCKA Society, CEA, France, January 2006.
- [17] Y.Y. Hsu. *On the size range of active nucleation cavities on a heating surface*, J. of Heat Transfer, No.84, pp. 207-216, 1962
- [18] N. Kurul , M.Z. Podowski *Multidimensional effects in forced convection subcooled boiling*, Conference on heat and mass transfer, Jerusalem, 1991
- [19] H.C. Unal. *Maximum bubble diameter, maximum bubble growth time and bubble growth rate during subcooled nucleate flow boiling of water up to 17.7MW/m²* , Int. J. Heat Mass Transfer, No. 19, pp. 643-649, 1976
- [20] E. Deutsch, O. Simonin *Large Eddy Simulation applied to the motion of particles in stationary homogeneous fluid turbulence*, Turbulence Modification in Multiphase Flows, ASME FED, 1991, Vol. 110, pp. 35-42
- [21] G.T. C Sanady *Turbulent diffusion of heavy particles in the atmosphere*, J. Atm. Sc., 1963, Vol. 20, pp. 201-208
- [22] R. Ferri, A. Achilli, S. Gandolfi *PERSEO PROJECT. Experimetal Data Report*, SIET 01 014 RP 02, Piacenza, Italy, December 20, 2002
- [23] P. Meloni, J. F. Pignatel *Simulation of the PANDA Isolation Condenser Using CATARE and RELAP*, ENEA QT-SBA-00006, Bologna, Italy, May 25 , 1999.
- [24] M. Rigamonti *PERSEO project: nodalisation for the Relap5 Mod. 3.2 code and calculation results*, SIET 00 945 RF 02. Piacenza, Italy, February 28 , 2002.
- [25] A. Achilli *Nuovo sistema di emergenza a scambiatore di calore immerso (New emergency system with immersed heat exchanger)*, SIET 00 915 ST 01 Rev. 1. Piacenza, Italy, January 21 , 2002.

- [26] P. Meloni, *CATHARE2 V1.4 Capability to simulate the performance of Isolation Condenser Systems with Thermal Valve*, Proc. International Conference Nuclear Energy in Central Europe, Portoroz, Slovenia, 2001.
- [27] P. Meloni, A. Achilli, R. Ferri, F. Bianchi *Experimental campaign and numerical analysis for the in-pool energy removal system for emergency operation*, 13th International Conference on Nuclear Engineering Beijing, China, May 16-20, 2005
- [28] F. Bianchi et al., *Assessment of RELAP5 MOD3.3 and CATHARE 2 V1.5a against a Full Scale Test of PERSEO Device*, Proc. 12th International Conference on Nuclear Engineering (ICONE12), Arlington, Virginia, USA, April 25-29, 2004.
- [29] R. F. Kulak and C. Fiala, *NEPTUNE: A System of Finite Element Programs for Three-Dimensional Nonlinear Analysis*, Nuclear Engineering and Design, 106, pp. 47-68 (1988) 17, 65
- [30] F. Bassenghi, G. Bornia, L. Deon and S. Manservigi, P. Meloni and M. Polidori *IMPLEMENTATION AND VALIDATION OF THE NURISP PLATFORM*, DIENCA - University of bologna, Via dei Colli 16, 40136 Bologna, Italy. ENEA - Via Martiri di Monte Sole 4, 40129 Bologna, Italy. CERSE-UNIBO RL1308/2011
- [31] F. Bassenghi, G. Bornia, S. Manservigi, R. Scardovelli, F. Donato, C. Lombardo, M. Polidori *OPTIMIZATION AND VALIDATION OF THE CFD MODULES IN THE NURISP PLATFORM*, CIRTEN - Universit  di Bologna DIENCA ENEA - Via Martiri di Monte Sole 4, 40129 Bologna, Italy. NNFISS-LP2-089

List of Figures

1.1	Junction between two modules	9
1.2	AXIAL 1D element	10
1.3	VOLUME 0D element	10
1.4	3D module	11
1.5	Boundary condition module	12
1.6	RUPTURE element	12
1.7	TEE scheme	13
1.8	Assembly of modules	14
1.9	Map of the motion regimes in CATHARE code	15
1.10	Spatial discretization of the AXIAL module	21
1.11	Spatial discretization of the standard VOLUME module	22
1.12	Spatial discretization of the 3D module	22
1.13	junction between two AXIAL elements	24
1.14	weight notion in a hydraulic circuit description	25
1.15	Description of an AXIAL element	26
1.16	Examples of sub-modules or gadget associated with an AXIAL element	27
2.1	Modules of the NEPTUNE CFD	31
2.2	Boiling heat flux at the wall	44
2.3	Tree structure of a case study	60
2.4	NEPTUNE GUI interface (Edamox).	61
2.5	Suggested parameter order.	63
2.6	Geometry and mesh of the channel	66
2.7	Fluid and Flow Properties panel	67
2.8	Inter-phase forces for liquid and vapor phases	68
2.9	Input-output control panel	69
2.10	Generality panel	70
2.11	Numerical Scheme panel	71
2.12	Scalar panel	72

2.13	Boundary conditions applied on the boiling channel	72
2.14	boundary conditions panel	73
2.15	Run panel	74
3.1	Scheme of the PERSEO facility	75
3.2	PERSEO facility scheme of the primary side and main elevations	77
3.3	PERSEO facility Steam Duct and Liquid Line between the pools	78
3.4	Hx Pool temperature measurement position	81
3.5	Overall Pool temperature measurement position	82
3.6	Water flowrate between the pools (partial HX Pool fill-up)	86
3.7	Water flowrate between the pools (total HX Pool fill-up)	86
3.8	HX Pool and Overall Pool levels	87
3.9	HX exchanged power	87
3.10	Primary side pressure	88
3.11	HX Pool temperatures	88
3.12	Overall Pool temperatures	89
3.13	Water flowrate between the pools (2 Phase)	90
3.14	HX Pool and Overall Pool water level (2 Phase)	91
3.15	Primary side pressure (2 Phase)	91
3.16	HX exchanged power (2 Phase)	92
3.17	HX Pool temperatures (2 Phase)	92
3.18	Overall Pool temperatures (2 Phase)	93
3.19	Water flowrate between the pools	94
3.20	HX Pool and Overall Pool water level	95
3.21	Primary side pressure	95
3.22	HX exchanged power	96
3.23	HX Pool temperatures	96
3.24	Overall Pool and pool connecting line temperatures	97
4.1	CATHARE nodalization scheme	100
4.2	HX Pool collapsed water level	101
4.3	Overall Pool collapsed water level	101
4.4	HX Pool relative pressure	102
4.5	HX exchanged power	102
4.6	Overall Pool temperatures	103
4.7	HX tube wall temperatures	103
4.8	HX Pool collapsed water level	105
4.9	Overall Pool collapsed water level	106
4.10	HX Pool relative pressure	106

4.11	HX exchanged power	107
4.12	Overall Pool temperatures	107
4.13	HX tube wall temperatures	108
4.14	HX Pool collapsed water level	109
4.15	Overall Pool collapsed water level	109
4.16	HX Pool relative pressure	110
4.17	HX exchanged power	110
4.18	Overall Pool temperatures	111
4.19	HX tube wall temperatures	111
4.20	3D volume Overall Pool modeling scheme	112
4.21	HX Pool relative pressure	113
4.22	HX Pool collapsed water level	114
4.23	HX exchanged power	114
4.24	Overall Pool collapsed water level	115
4.25	Overall Pool collapsed water level	115
4.26	HX Pool relative pressure	116
4.27	HX Pool collapsed water level	116
4.28	HX exchanged power	117
5.1	Coupling CATHARE-NEPTUNE	120
5.2	Overall pool temperature measurement positions.	121
5.3	Overall pool temperatures for different probes.	122
5.4	2D geometry and mesh of OP-injector system	123
5.5	Steam Mass flowrate to OP pool	124
5.6	Water Mass flowrate to HX pool (left) and water discharge Mass flowrate (right)	124
5.7	Physical properties.	125
5.8	Input-Output control	126
5.9	Physical models	126
5.10	Scalars	127
5.11	Boundary conditions.	128
5.12	Chronology of the temperature main events for the probe <i>TP6</i>	132
5.13	Water mass flowrate to HX pool over the time interval $[0 - 500]s$ com- puted from CATHARE simulation.	133
5.14	Water discharge mass flowrate and steam mass flowrate to overall pool over the time interval $[0 - 500]s$ computed from CATHARE simulation.	133
5.15	Water level at $t = 150$ s.	134
5.16	Water level at $t = 204$ s.	134

5.17	Computational and experimental temperature profiles in probes TP6 (1) and TP8 (2) as a function of time.	135
5.18	Steam mass flowrate to overall pool over the time interval [500 – 3000] <i>s</i> defined from CATHARE simulation	136
5.19	Water mass flowrate to HX pool and water discharge mass flowrate over the time interval [500 – 3000] <i>s</i> defined from CATHARE simulation . . .	136
5.20	Steam entering the injector (right) and injection of steam into water (left)	137
5.21	Steam and water mixing (right) and inverse flow (left)	137
5.22	Temperature of the probes TP6 (red) and TP8 (green) from experiment and NEPTUNE computation (blue and violet) and zoom of the temperature oscillations	138
5.23	Steam mass flowrate to overall pool over the time interval [3200 – 4200] <i>s</i> defined from CATHARE simulation.	139
5.24	Water mass flowrate to the HX pool and water discharge mass flowrate over the time interval [3200 – 4200] <i>s</i> defined from CATHARE simulation.	139
5.25	Extended water temperature distribution in boiling pool	140
5.26	Steam injection on boiling pool (right) and steam release to the water surface (left)	140
5.27	Steam mass flowrate to overall pool over the time interval [4200 – 7700] <i>s</i> defined from CATHARE simulation.	141
5.28	Water mass flowrate to the HX pool and water discharge mass flowrate over the time interval [4200 – 7700] <i>s</i> defined from CATHARE simulation.	141
5.29	Steam injection above the water level.	142
5.30	PERSEO 3D hexahedral grid (left) and a detail of the injector and boil-off region (right) for the real geometry	142
5.31	Pressure [Pa] (left) and water volume fraction (right) at a $x=3.12$ m section for $t_1 = 9.08398$ s	143
5.32	Pressure [Pa] (left) and z component of steam velocity [<i>m/s</i>] (right) at a $x = 3.12$ m section for $t_1 = 9.09419$ s (top), $t_1 = 9.09833$ s (middle) and $t_1 = 9.10886$ s (bottom)	144
5.33	PERSEO 3D hexahedral grid (left) and a detail of the injector and boil-off region (right) for the geometry with straight injector and real position of the injector exit	145
5.34	Water volume fraction (top), pressure (middle) and vertical component of steam velocity (bottom) for $t_1 = 50.6804$ s (left) and $t_1 = 51.8309$ s (right) on a section at $x=3.312$	146

5.35	Water volume fraction (top), pressure (middle) and vertical component of steam velocity (bottom) for $t_1 = 53.7734$ s (left) and $t_1 = 55.9895$ s (right) on a section at $x=3.312$	147
5.36	PERSEO 3D hexahedral grid (left) and a detail of the injector region (right) for the geometry with a straight injector and a modified position of the injector nozzle	149
5.37	Water volume fraction (top) and condensation rate (bottom) for the geometry with a straight injector and a modified position of the injector nozzle, at times $t_1 = 12.88, 14.15, 15.18$ s (left to right)	150
5.38	Water volume fraction (top) and condensation rate (bottom) for the geometry with a straight injector and a modified position of the injector nozzle, at times $t_1 = 200.6, 202.97, 205.52$ s (left to right)	151
5.39	Vertical (left) and radial (right) steam velocity components on the vertical section through the injector axis at $x = 2.75$ m and time $t_1 = 200.6$ s, for the geometry with a straight injector and a modified position of the injector nozzle	151
5.40	Water temperature (left) and volume fraction (right) on the vertical sections through the injector axis at $x = 2.75$ m and $y = 2.75$ m and times in the range 200.6 s $< t_1 < 243.36$ s, for the geometry with a straight injector and a modified position of the injector nozzle	152
5.41	Water streamlines and velocity vectors (lower part only) on plane $x = 2.75$ m for $t_1 = 213.28$ s. Contours for water volume fraction.	153
5.42	Experimental water temperature evolution for different probes	153
5.43	Comparison between experimental and numerical water temperature data for different probes	154

List of Tables

2.1	Variable initialization	54
2.2	NEPTUNE modules	62
2.3	Scalar equation options	64
2.4	User routines	65
3.1	PERSEO facility design features	79
3.2	PERSEO shake-down test matrix	83
3.3	PERSEO test matrix	83
3.4	Main PERSEO test 7 parameters in phase 1	84
3.5	Chronology of main events of Phase 1	85
3.6	Chronology of main events of Phase 2	90
3.7	Main PERSEO test 9 parameters	93
3.8	Chronology of main events of test 9	94
4.1	Chronology of main events of Phase 1	101
4.2	Chronology of main events of Phase 2	105
4.3	Chronology of main events of test 9	112
5.1	Exact locations (in <i>mm</i>) of the probes for temperature measurements with respect to the reference frame indicated in Figure 5.2.	122
5.2	Fluid and flow properties selected for PERSEO test 9	124
5.3	Chronology of the Temperature main events	132
5.4	Initial conditions of Overall Pool and HX pool.	133